

PHYSICAL PROPERTIES OF ANATASE TiO<sub>2</sub> ALTERED BY  
LANTHANIDE ATOMS

A THESIS SUBMITTED TO  
THE GRADUATE SCHOOL OF NATURAL AND APPLIED SCIENCES  
OF  
MIDDLE EAST TECHNICAL UNIVERSITY

BY

KIVILCIM BAŞAK VURAL

IN PARTIAL FULFILLMENT OF THE REQUIREMENTS  
FOR  
THE DEGREE OF DOCTOR OF PHILOSOPHY  
IN  
PHYSICS

SEPTEMBER 2015



Approval of the thesis:

**PHYSICAL PROPERTIES OF ANATASE TiO<sub>2</sub> ALTERED BY  
LANTHANIDE ATOMS**

submitted by **KIVILCIM BAŞAK VURAL** in partial fulfillment of the requirements for the degree of **Doctor of Philosophy in Physics Department, Middle East Technical University** by,

Prof. Dr. Gülbin Dural Ünver \_\_\_\_\_  
Dean, Graduate School of **Natural and Applied Sciences**

Prof. Dr. Mehmet Zeyrek \_\_\_\_\_  
Head of Department, **Physics**

Prof. Dr. Şinasi Ellialtıođlu \_\_\_\_\_  
Supervisor, **Basic Science, TEDU**

Assist. Prof. Dr. Daniele Toffoli \_\_\_\_\_  
Co-supervisor, **Chemical and Pharmaceutical Sciences Department, University of Trieste**

**Examining Committee Members:**

Prof. Dr. Şenay Katırcıođlu \_\_\_\_\_  
Physics Department, METU

Prof. Dr. Şinasi Ellialtıođlu \_\_\_\_\_  
Basic Science, TEDU

Prof. Dr. Ođuz Gülseren \_\_\_\_\_  
Physics Department, Bilkent University

Prof. Dr. Mehmet akmak \_\_\_\_\_  
Physics Department, Gazi University

Assoc. Prof. Dr. Hande Toffoli \_\_\_\_\_  
Physics Department, METU

**Date:** \_\_\_\_\_

I hereby declare that all information in this document has been obtained and presented in accordance with academic rules and ethical conduct. I also declare that, as required by these rules and conduct, I have fully cited and referenced all material and results that are not original to this work.

Name, Last Name: KIVILCIM BAŞAK VURAL

Signature :

# ABSTRACT

## PHYSICAL PROPERTIES OF ANATASE TiO<sub>2</sub> ALTERED BY LANTHANIDE ATOMS

Vural, Kıvılcım Başak

Ph.D., Department of Physics

Supervisor : Prof. Dr. Şinasi Ellialtıođlu

Co-Supervisor : Assist. Prof. Dr. Daniele Toffoli

September 2015, 95 pages

In this thesis, the structural, electronic and optical properties of adsorption of single lanthanide atoms (Pr, Gd, Er, and Lu) in anatase TiO<sub>2</sub> (101) substrate have been investigated by using the first-principles calculations based on Hubbard  $U$  corrected term density functional theory (DFT+ $U$ ). Here, among the lanthanides, we have primarily concentrated on Pr atom. TiO<sub>2</sub> has attracted a material in various technological applications due to its chemical stability. In most of the technological applications such as photocatalytic TiO<sub>2</sub> have been used to relate to its physical properties. Lanthanides (Ln) have drawn the attention as good dopants because of the improved features of TiO<sub>2</sub>. The strong correlations are arising from the localized Ti 3d and lanthanide (Ln) 4f orbitals. This indicates that the doping process do occur easily.

The adsorption energies of Pr atom are found high in all binding models, so Pr is effective atom for adsorption process. The result of interaction between

Ln and the surface, impurity states occur into the band gap, this provide the optical activity of the TiO<sub>2</sub> (101) surface with improving both the UV-visible and the near-IR range. Also, we have studied adsorbate-dopant interaction using prototypical dye molecules such as benzoic acid and Coumarin 153. Molecular adsorption energies and the optical properties are improved by the presence of Ln. In addition, considering the interaction between Coumarin 153 (C153) and reduced (O-vacancy) surfaces, it seems to be an effective method as much as.

Keywords: Photocatalysis, anatase, TiO<sub>2</sub>, lanthanides, Coumarin 153, DFT+U

# ÖZ

## LANTANİTLER TARAFINDAN ANATAZ $\text{TiO}_2$ NİN FİZİKSEL ÖZELLİKLERİNİN DEĞİŞİMİ

Vural, Kıvılcım Başak

Doktora, Fizik Bölümü

Tez Yöneticisi : Prof. Dr. Şinasi Ellialtıoğlu

Ortak Tez Yöneticisi : Yrd. Doç. Dr. Daniele Toffoli

Eylül 2015 , 95 sayfa

Bu çalışmada, anataz  $\text{TiO}_2$  (101) tabanlı yüzeye tek lantanit atomlarının (Pr, Gd, Er, and Lu) tutunmasının yapısal, elektronik ve optik özellikleri Hubbard  $U$  düzeltilmiş yoğunluk fonksiyonu kuramına (DFT+ $U$ ) dayalı ilk prensipler hesapları kullanılarak incelendi. Burada, lantanit atomları arasında, öncelikle Pr atom üzerinde yoğunlaşmıştır.  $\text{TiO}_2$  ise nedeniyle kimyasal kararlılığa sahip olması nedeniyle çeşitli teknolojik uygulamalarda çeken bir malzemedir. Fotokatalitik gibi teknolojik uygulamaların çoğu  $\text{TiO}_2$  yapısının fiziksel özellikleri ile ilişkilidir. Lantanitler (Ln)  $\text{TiO}_2$ 'nin özelliklerini geliştirmesi nedeniyle iyi dopantlar olarak dikkati çekmiştir. Güçlü korelasyon lokalize Ti 3d ve lantanide (Ln) 4f orbitallerinin kaynaklanmaktadır. Bu katkılama işleminin kolayca meydana geldiğini gösterir.

Pr atomun adsorpsiyon enerjileri tüm bağlanma modellerinde yüksek bulunmuştur, yani Pr adsorpsiyon süreci için etkili atomdur. Ln ve yüzey arasın-

daki etkileşiminin sonucu, bant aralığında kirlilik durumları meydana gelir, TiO<sub>2</sub> yüzeyinin optik aktivitesini sağlayarak, hem UV-görünür hem de yakın-IR aralığında iyileştirir. Ayrıca, benzoik asit ve kumarin 153 prototip boya moleküllerini kullanılarak adsorbate-takviye etkileşimini inceledik. Moleküler adsorpsiyon enerjisi ve optik özellikleri Ln varlığı ile geliştirildi. Buna ek olarak, kumarin 153 (C153) ve indirgenmiş (O-boş) yüzeyleri arasındaki etkileşim göz önüne alındığında, etkili bir yöntem olarak görünmektedir.

Anahtar Kelimeler: Fotokataliz, anataz, TiO<sub>2</sub>, lanthanitler, Kumarin 153, DFT+U



To my family

## ACKNOWLEDGMENTS

I would like to express my deep and sincere gratitude to my supervisor Prof. Dr. Şinasi Ellialtıođlu, for his support and advice. I am grateful to my unofficial advisor Assoc. Prof. Dr. Hande Toffoli for her guidance, eternal patience, and encouragement. I would like to thank Prof. Dr. Ođuz Gölseren for his critical comments, valuable advices about this and in many others.

I also would like to thank deeply to my dear colleagues Ceren Sibel Sayın and Merve Demirtaş for their cooperation and supportive discussions that were crucial for this thesis, to my special friends Mehtap Özbey Arabacı, Nazlı Somel, Ozan Yıldırım, Mehmet Ali Olpak, Mehmet Somel, Yakup Pekön, Çađan Aksak, and Gül Çorbacıođlu for their helpful and support motivating that were significant for me.

I want to thank to best friends Pınar İçemer, Pınar Yađcı, Canan Erden and Gülsüm Karaşahin for their support in every way that was fundamental for my life. I want to thank for Burçin Cihan and Ebru Aylar, who were on my side in every time.

# TABLE OF CONTENTS

ABSTRACT . . . . .	v
ÖZ . . . . .	vii
ACKNOWLEDGMENTS . . . . .	x
TABLE OF CONTENTS . . . . .	xi
LIST OF TABLES . . . . .	xiv
LIST OF FIGURES . . . . .	xvii
LIST OF ABBREVIATIONS . . . . .	xxi
CHAPTERS	
1 INTRODUCTION . . . . .	1
2 THEORETICAL BACKGROUND . . . . .	9
2.1 The problem of structure of matter . . . . .	9
2.2 Pre-Density Functional Theory . . . . .	10
2.2.1 Hartree and Hartree-Fock approximation . . . . .	10
2.2.2 Thomas-Fermi Theory . . . . .	12
2.3 Modern Density Functional Theory . . . . .	12
2.3.1 Hohenberg-Kohn Theory . . . . .	12

2.3.2	Self-consistent Kohn–Sham equations . . . . .	13
2.4	Functionals for Exchange and Correlation . . . . .	13
2.4.1	The Local Density Approximation (LDA) . . . . .	14
2.4.2	Generalized Gradient Approximation (GGA) . . . . .	15
2.4.2.1	PBE functional . . . . .	15
2.5	Pseudopotentials . . . . .	16
2.5.1	Ultrasoft Pseudopotential . . . . .	17
2.5.2	Projector Augmented Waves . . . . .	17
2.6	Numerical Calculations . . . . .	18
2.7	Hubbard corrected density functional theory (DFT+U) . . . . .	18
2.8	Dielectric Matrix . . . . .	21
3	PR ADSORBED ON (101) ANATASE SURFACE . . . . .	23
3.1	Computational Method . . . . .	23
3.2	Result and Discussions . . . . .	24
3.2.1	Hubbard Correction Term . . . . .	24
3.2.2	Adsorptional Case . . . . .	27
3.2.3	Varying of U parameter . . . . .	32
4	BENZOIC ACID (BZA) ADSORPTION ON THE SURFACE . . . . .	45
4.0.4	Benzoic acid (BZA) . . . . .	45
4.0.5	Benzoic acid adsorbed on Bare Surface . . . . .	47
4.0.6	Benzoic Acid Adsorbed on Pr/TiO <sub>2</sub> Surface . . . . .	49

4.0.7	Dissociated Benzoic Acid on Surface . . . . .	50
4.0.8	Dissociated Benzoic Acid on the Pr/TiO <sub>2</sub> Surface	51
4.0.9	Optical Properties . . . . .	52
5	COUMARIN 153 (C153) ADSORPTION ON THE TiO <sub>2</sub> SURFACE	59
5.1	Computational Method . . . . .	59
5.2	Result and Discussions . . . . .	59
5.2.1	Coumarin 153 . . . . .	59
5.2.2	TiO <sub>2</sub> Anatase Surface . . . . .	60
5.2.3	Adsorption of Coumarin 153 . . . . .	62
5.2.3.1	Adsorption on TiO <sub>2</sub> . . . . .	62
5.2.3.2	Adsorption on Pr/TiO <sub>2</sub> . . . . .	65
5.2.4	Optical Properties . . . . .	68
6	BEYOND PR . . . . .	71
6.1	Computational Method . . . . .	71
6.2	Result and Discussions . . . . .	72
6.2.1	Adsorptional Cases for a Single Lanthanides .	72
6.2.2	Benzoic Acid Adsorbed on Ln/TiO <sub>2</sub> Surface . .	74
7	CONCLUSION . . . . .	81
	REFERENCES . . . . .	85
	APPENDICES	
	CURRICULUM VITAE . . . . .	95

# LIST OF TABLES

## TABLES

Table 3.1 Unit cell parameters ( $\text{\AA}$ ) and band gaps for $\text{TiO}_2$ anatase bulk obtained after complete structural optimization with PBE+U compared to experimental data. . . . .	26
Table 3.2 Unit cell parameters ( $\text{\AA}$ ) and band gaps for $\text{Pr}_2\text{O}_3$ bulk structure obtained after complete structural optimization with PBE+U compared to experimental data. . . . .	27
Table 3.3 Adsorption energies (eV), magnetic moments ( $\mu_B$ ), and interatomic distances ( $\text{\AA}$ ) of the three Pr adsorption configurations shown in Fig. 3.3. $U_{Ti}$ and $U_{Pr}$ are both 5 eV. . . . .	29
Table 3.4 Bader charge of Pr adsorbed on the surface in three different configuration. In Hubbard U value used in the different for the $U_{Ti}$ and $U_{Pr}$ are fixed as 5 eV. . . . .	30
Table 3.5 Calculated parameters: adsorption energy and average bond lengths of Pr adsorbed on the surface in two different configuration. In Hubbard U value used in the different for the Pr 4f orbital and fixed as 5 eV for the Ti 3d orbital. . . . .	33
Table 3.6 Bader charge of Pr adsorbed on the surface in two different configuration. In Hubbard U value used in the different for the Pr 4f orbital and fixed as 5 eV for the Ti 3d orbital. . . . .	34

Table 3.7 Adsorption energy (eV), magnetic moment ( $\mu_B$ ), and average bond lengths ( $\text{\AA}$ ) two Pr adsorption geometries on the $\text{TiO}_2$ $U_{Pr}=5-8$ eV and $U_{Ti}=6$ eV. . . . .	35
Table 3.8 Bader charges ( $ e $ ) of two Pr adsorption geometries on the $\text{TiO}_2$ $U_{Pr}$ . In Hubbard U value used in the different for the Pr 4f orbital and fixed as 6 eV for the Ti 3d orbital. eV. . . . .	36
Table 3.9 Adsorption energy (eV), magnetic moment ( $\mu_B$ ), and average bond lengths ( $\text{\AA}$ ) of two Pr adsorption geometries on the $\text{TiO}_2$ for $U_{Pr}=5-8$ eV and $U_{Ti}=4$ eV. . . . .	37
Table 3.10 Bader charges ( $ e $ ) of two Pr adsorption geometries on the $\text{TiO}_2$ for $U_{Pr}=5-8$ eV and $U_{Ti}=4$ eV. . . . .	38
Table 4.1 Average bond lengths of of benzoic acid experimental and calculated by DFT . . . . .	46
Table 4.2 Average bond lengths ( $\text{\AA}$ ) and adsorption energies (eV) of BZA and BZ adsorbed on $\text{TiO}_2$ and Pr/ $\text{TiO}_2$ . . . . .	48
Table 4.3 Bader charge values of BZA and BZ adsorbed on $\text{TiO}_2$ and Pr: $\text{TiO}_2$ . . . . .	52
Table 5.1 Average bond lengths, electronic bang gap, and adsorption energies of C153 adsorbed on both the anatase surface and the surface having O-vacancies. . . . .	63
Table 5.2 Bader charge analysis results for C153/ $\text{TiO}_2(101)$ anatase systems. For labeling refer to Fig 5.3 5.4 . . . . .	66
Table 6.1 Adsorption energy and average bond lengths of Ln adsorbed on the surface. . . . .	72
Table 6.2 Bader charges ( $ e $ ) and band gap of Ln (Gd, Er, Lu) adsorption geometries on the $\text{TiO}_2$ . . . . .	73

Table 6.3 Average bond lengths ( $\text{\AA}$ ) and adsorption energies (eV) of ben- zoic acid adsorbed on $\text{TiO}_2$ and $\text{Ln}/\text{TiO}_2$ . . . . .	75
Table 6.4 Bader charge and band gap values of BZA adsorbed on $\text{Ln}:\text{TiO}_2$ .	76



# LIST OF FIGURES

## FIGURES

Figure 1.1 Schematic diagram of photovoltaic device by Gratzel [24]. Photon adsorption causes the electron excitation from ground state $S^0$ to excited state $S^*$ . Electron travels (ballistically) from $S^*$ to the conducting surface layer and over the potential barrier, into the semiconductor, reaching to the ohmic back conduct, after reduction of the oxide holes. . . . .	3
Figure 3.1 (a) Front views of the slab modeling the anatase bulk. (b) The electronic band structure are represented. . . . .	25
Figure 3.2 The geometric and electronic structures of $\text{TiO}_2$ (101) surface. Oxygen, and titanium atoms are indicated red, and gray balls. Energy bands and DOS structures are represented rightmost panel of atomic structure figures. . . . .	28
Figure 3.3 The geometric and electronic structures of three different adsorptive Pr: $\text{TiO}_2$ systems respectively for (a) Pr(a-1), (b) Pr(a-2), and (c) Pr(a-3) systems. Praseodymium, oxygen, and titanium atoms are indicated pink, red, and gray balls. . . . .	39
Figure 3.4 The optical absorption spectra of Pr adsorbed on $\text{TiO}_2$ models at (a) visible range and (b) infrared range. . . . .	40

Figure 3.5 The geometric and electronic structures of two adsorptional cases for Pr:TiO <sub>2</sub> system, as the value of U for Ti was taken in 5 eV and for Pr was taken in the range of 5 to 8, respectively. While the first column represents the Pr( <i>a</i> -1) case, the second column represents Pr( <i>a</i> -2) case. Energy bands structures are represented rightmost panel of atomic structure figures . . . . .	41
Figure 3.6 The geometric and electronic structures of two adsorptional cases for Pr:TiO <sub>2</sub> system, as the value of U for Ti was taken in 6 eV and for Pr was taken in the range of 5 to 8, respectively and it was taken to 6 eV for Ti. While the first column represents the Pr( <i>a</i> -1) case, the second column represents Pr( <i>a</i> -2) case. Energy bands and DOS structures are represented rightmost panel of atomic structure figures . . . . .	42
Figure 3.7 The geometric and electronic structures of two adsorptional cases for Pr:TiO <sub>2</sub> system, as the value of U for Ti was taken in 4 eV and for Pr was taken in the range of 6 to 8, respectively. While the first column represents the Pr( <i>a</i> -1) case, the second column represents Pr( <i>a</i> -2) case. Energy bands and DOS structures are represented rightmost panel of atomic structure figures . . . . .	43
Figure 4.1 (a) The relaxed benzoic acid with atomic labels, (b) HOMO and LUMO charge densities . . . . .	47
Figure 4.2 The geometric and electronic structures of adsorption of BZA on the bare surface (C <sub>b</sub> ( <i>a</i> -1);(a), C <sub>b</sub> ( <i>a</i> -2);(b), C <sub>b</sub> ( <i>a</i> -3);(c)) and on Pr/TiO <sub>2</sub> (C( <i>a</i> -1);(d), C( <i>a</i> -2);(e), C( <i>a</i> -3)(f)surface, respectively. Energy bands and PDOS structures are represented rightmost panel of atomic structure figures . . . . .	55
Figure 4.3 The geometric and electronic structures of adsorption of dissociated benzoic acid on the bare surface and on Pr:TiO <sub>2</sub> surface . .	56

Figure 4.4 The optical absorption spectra of (a) benzoic acid (BZA) and (b) benzoate anion (BZ) adsorbed on TiO <sub>2</sub> models at visible range. . . . .	56
Figure 4.5 The optical absorption spectra of benzoic acid (BZA) adsorbed on Pr/TiO <sub>2</sub> models at (a)visible range, (b) infrared range. . . . .	57
Figure 4.6 The optical absorption spectra of benzoate anion (BZ) adsorbed on Pr/TiO <sub>2</sub> models at (a)visible range, (b) infrared range. . . . .	57
Figure 5.1 HOMO-LUMO of isolated Coumarin 153 is represented . . . . .	60
Figure 5.2 The atomic and electronic structures of (a) TiO <sub>2</sub> , (b) TiO <sub>2</sub> (V <sub>01</sub> ), and (c) TiO <sub>2</sub> (V <sub>02</sub> ) surfaces. PDOS graphics is shown rightmost panel by band structure, therein, Ti <sub>4c</sub> , Ti <sub>5c</sub> and O are represented by the blue, gree(orange), are red colours, respectively . . . . .	62
Figure 5.3 The geometric and electronic structures of three adsorptional cases for C153:TiO <sub>2</sub> and C153/Pr/TiO <sub>2</sub> system. While the first column (a) represents the atomic structure case, the second and third columns; (b), (c) represent energy bands and DOS structures. . . . .	64
Figure 5.4 The geometric and electronic structures of three adsorptional cases for C153/TiO <sub>2</sub> (V <sub>01</sub> 1), C153/TiO <sub>2</sub> (V <sub>01</sub> 2) and C153/TiO <sub>2</sub> (V <sub>02</sub> ) systems. While the first column (a) represents the atomic structure case, the second and third columns; (b), (c) represent energy bands and DOS structures. . . . .	67
Figure 5.5 The optical absorbance of bare, O-vacancies and Pr-doped TiO <sub>2</sub> (101)-3×1 surfaces (a, b), cases for C153:TiO <sub>2</sub> and C153/Pr/TiO <sub>2</sub> system (c, d) and cases for C153/TiO <sub>2</sub> (V <sub>01</sub> 1), C153/TiO <sub>2</sub> (V <sub>01</sub> 2) and C153/TiO <sub>2</sub> (V <sub>02</sub> ) systems (e, f). The graphs on the left-hand panel (a, c, e) refer to the visible range and those on the right-hand panel (b, d, f) to the infrared region. . . . .	69

Figure 6.1	The geometric and electronic structures of adsorptional cases for Gd:TiO <sub>2</sub> systems, Er:TiO <sub>2</sub> , and Lu:TiO <sub>2</sub> systems, respectively. While the first column (a) represents the atomic structure case, the second and third columns; (b) represent energy bands and DOS structures. . . . .	77
Figure 6.2	The optical absorption spectra of Ln (Gd, Er, Lu) adsorbed on TiO <sub>2</sub> models at (a) visible and (b) infrared ranges. . . . .	78
Figure 6.3	The optical absorption spectra of BZA adsorbed on Ln(Gd, Er, Lu)/TiO <sub>2</sub> models at (a) visible and (b) infrared ranges. . . . .	78
Figure 6.4	The geometric and electronic structures of adsorptional cases for BZA/Gd:TiO <sub>2</sub> systems, BZA/Er:TiO <sub>2</sub> and BZA/Lu:TiO <sub>2</sub> systems. While the first column (a) represents the atomic structure case, the second and third columns; (b), (c) represent energy bands and DOS structures. . . . .	79

## LIST OF ABBREVIATIONS

PBE	Perdew, Burke, and Enzerhof
GGA	Generalized Gradient Approximation
LDA	The Local Density Approximation
C153	Coumarin 153
CB	Conduction Band
VB	Valance Band
FE	Fermi Energy



# CHAPTER 1

## INTRODUCTION

Semiconductor photocatalysis relies on semiconductors that are able to accelerate chemical reactions through light absorption. This process has been investigated by scholars from various disciplines of science and engineering, and has been applied in various industrial areas such as environmental remediation [1, 2, 3], green energy production [5, 6, 7] and medical therapy [8]. Considering the gradual increase in the energy consumption of the world's population and the limited fossil energy resources the popularity of this topic is not a surprise.

In principle, in photocatalysis process, photon energy should be larger than or equal to the band gap energy of the semiconductor material in order to excite an electron in the conduction band to the valence band. The excited electron leaves behind a hole in the valence band and thus an electron-hole pair is created. This electron-hole pair may travel to the surface of the photocatalyst and react adsorbates on the surface. The performance of photocatalysis depends on several factors including reduction and oxidation rate of the surface by electrons and holes, light absorption spectrum and coefficient, and the recombination rate of the electron-hole pair. Although a complete list would involve many more, most of the studies on the topic refer to these three factors [9, 10, 11, 12]

Many semiconductor materials have been used for these photocatalytic applications, such as  $\text{TiO}_2$ ,  $\text{ZnO}$ ,  $\text{NiO}$ ,  $\text{Fe}_2\text{O}_3$ ,  $\text{CdS}$ , and  $\text{ZnS}$  [13, 14, 15]. Among these materials, titania ( $\text{TiO}_2$ ) has undoubtedly drawn the greatest attention due to its high stability, low cost and low environmental impact [16, 17, 18, 19]. In 1972, photocatalytic splitting of water on a  $\text{TiO}_2$  electrode under ultraviolet (UV)

light was discovered by Fujishima and Honda [20, 21]. Later, in 1977, Frank and Bard demonstrated that cyanide in water could be treated by electrolytic decomposition of  $\text{TiO}_2$  upon lighting [22] leading to the wide use of photocatalysis for purifying water. In addition, dye-sensitized solar cells (DSSC) based on  $\text{TiO}_2$  was improved by Gratzel et al [23]. Schematic diagram of it is as shown in the Fig 1.1. DSSC research has been rather active due to ease of production and more modest cost than silicon based photovoltaic devices. As a result,  $\text{TiO}_2$  has become a good candidate for the studies carried out on environmentally friendly energy sources operation. Principle of the DSSC can be described as follows: the light is absorbed by dye-molecules stored on the semiconductor surface. Electrons excited by photons are injected into the semiconductor conduction band. The electrons pass through an external circuit, then a redox process takes place in an electrolyte. Finally, the electrons get through the oxidized dye molecules to restart the procedure [25].

In nature,  $\text{TiO}_2$  is present in three main polymorphs namely anatase, rutile, and brookite. Among them, brookite is not favored in the applications because of its complex structure, which causes difficulties during the crystal growth process [26]. In practise, anatase and rutile are the most widely used variations of titania. Thermodynamically, the rutile phase is more stable than anatase; particularly its (110) surface has been widely used in surface science applications. But this suitability actually depends on the particle size. For instance, anatase is the most thermodynamically stable phase compared to rutile and brookite, if the diameter of the particles of the three phases are equal to each other and they are below 14 nm [27, 28]. On the other hand, the anatase form of titania especially its (101) and (100) facets [29] is generally favored in photocatalytic applications owing to its relatively higher photocatalytic activity [30, 31].

In spite of these favorable properties, anatase illustrates some problems in application. Because anatase has lower stability compared to rutile for its bulk phase, preparation of large single anatase crystal has traditionally been difficult [32]. Having limited information on the anatase structure for a quite a time was the reason for this difficulty. Fortunately, this difficulty has been overcome thanks to the developments in the sample preparation techniques. Anatase ap-



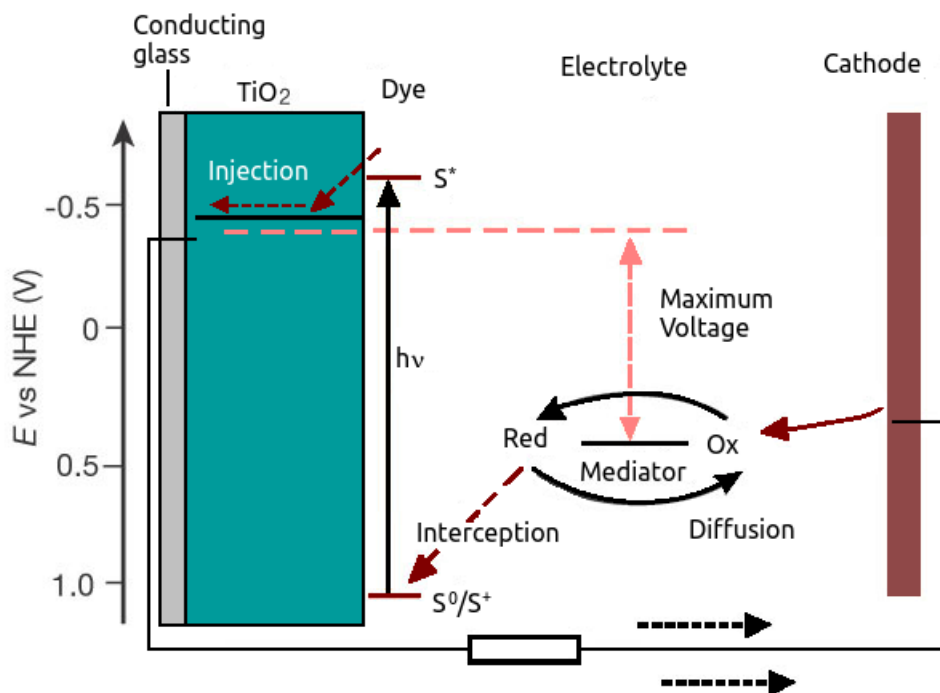


Figure 1.1: Schematic diagram of photovoltaic device by Gratzel [24]. Photon adsorption causes the electron excitation from ground state  $S^0$  to excited state  $S^*$ . Electron travels (ballistically) from  $S^*$  to the conducting surface layer and over the potential barrier, into the semiconductor, reaching to the ohmic back conduct, after reduction of the oxide holes.

lications have become more visible in the literature thereafter. However, there are still limiting factors in photocatalysis applications of anatase, caused by its wide band gap (3.2 eV). The large band gap leads to excitations corresponding only to a small portion of the solar energy, namely, the UV region (only 3% of the total emission). This drawback reduces the efficiency of solar energy conversion. Several methods have been developed in order to overcome this shortcoming, all focusing on tailoring the band gap to achieve visible range activity of  $\text{TiO}_2$ . This reduction of the band gap has been realized in many studies by ion doping [33, 34, 35], metal deposition on the anatase surface [36, 37, 38], and surface adsorption of dye molecules [39, 40]. Here,  $\text{TiO}_2$  provides an important advantage in the process of electron-transfer between the semiconductor and the adsorbed molecule. Among these techniques, ion doping [41] and dye

molecule adsorption are generally accepted to be the most direct and effective methods. Several types of ions have been used as dopants, such as n-type doping, p-type doping and cation-anion co-doping. Recently, transition and rare earth metals have emerged as a new generation class of dopant [42]. Similar including dye molecule adsorption on  $\text{TiO}_2$  have become an active area in photocatalytic research [43, 44].

Doping with some lanthanide ions, such as La, Ce, Eu, and Gd, have been examined widely in the literature as photocatalytic applications [45, 46]. Although some previous studies had reported on  $\text{TiO}_2$  modified by gas phase of the RE oxides ( $\text{Ln}_3\text{O}_2$ ), the mixtures of  $\text{TiO}_2$  with three RE oxides indicating higher photoactivity compared with pure  $\text{TiO}_2$  was first introduced in 1998 by Yu et al. [47]. The adsorption process or metal deposition (La, Nd and Pr) on the surface is known as a key issue to cause change in photocatalytic activity, the importance of which was reported by Parida and Sahu in their work [48]. Lanthanide ions are able to form complexes with various Lewis bases, such as amines, aldehydes, alcohols, carboxylic acid, owing to the interaction between these functional groups and the  $f$ -orbital of the lanthanides. Accordingly, adding lanthanide ions into any  $\text{TiO}_2$  structure could enable concentration of the organic pollutant at the semiconductor surface and consequently increases the photocatalytic activity of the catalyst [49]. Praseodymium (Pr) is one of these RE metals. Liang *et al.* [50] claimed that Pr-doped anatase  $\text{TiO}_2$  enhanced the photocatalytic activity under visible light in the degradation of an azo dye. However, application of any single lanthanide ion adsorption on surfaces is rare in the literature. To our knowledge, no studies have been conducted on the  $\text{Pr}^{3+}$  ion adsorbed on the anatase  $\text{TiO}_2$  surface based on the DFT+ $U$  approach, despite the importance of the adsorption process in understanding photocatalytic activity. The aim of large part of this thesis is to investigate the effects on the band structure of  $\text{Pr}^{3+}$  adsorption on the anatase (101) surface.

As indicated by many theoretical studies, the adsorbed dye molecules can absorb light in the visible region and readily inject the excited electron into the  $\text{TiO}_2$  conduction band. In other words, they can act as sensitizers. Regarding the adsorption of molecules, a large number of organic molecules are used in practice.

Anchoring groups, being important components of the dye molecules are the parts that are responsible for the interaction with the surface. For various dye molecules, the adsorption of common anchoring groups, such as carboxylic acid, phosphonic acid, and hydroxyl groups, have been investigated in many studies. Carboxylic acid is one of the most common anchoring groups in several studies. As for the benzoic acid, it is the simplest aromatic carboxylic acid [51, 52, 53]. There were many studies concerned with the adsorption of benzoic acid (BZA) on TiO<sub>2</sub> surfaces [54, 55]. Lunell *et al.* [56] showed that the spectra for TiO<sub>2</sub> remained the same and any states are not available in the band gap, after benzoic acid adsorption. Q. Guo *et al.* [57] demonstrated that the two oxygen atoms of dissociative benzoic acid can be adsorbed on the fivefold coordinated surface Ti atom at room temperature. Moreover, it is known that the strong interaction between the Pr atom with BZA can be realized [58, 59]. We discussed in the previous paragraph that the relationship of lanthanide ions with carboxylic acid is the influence on the photocatalytic activity. However to the best of our knowledge, there have been no studies in the literature on BZA adsorbed on the surface in the presence of lanthanide atoms in this work. We also investigate nondissociated and dissociated benzoic acid (BA) adsorbed on the Pr-added TiO<sub>2</sub>(101) surface.

The dyes which are present on the TiO<sub>2</sub> surface are important for the absorption of as much light as possible. The most successful sensitizers use derivatives of ruthenium complexes, which have been extensively studied for dye-sensitized solar cells applications [60, 61, 62]. However, the use of ruthenium in the application leads to an increase in cost due to its rare presence in nature. As a consequence, studies towards alternative dye molecule synthesis to be used in applications have increased recently. Among these molecules, organic dyes have been considered as an alternative to Ru complex sensitizers indicating many advantages for the applications. These advantages can be roughly considered as follows [63, 64]: Molecular structures of organic dyes in various form can be easily synthesized, organic dyes are highly low cost and much environmentally friendly compared to noble metal complexes and, organic dyes have shown a higher efficiency than some dyes based on Ru complexes in DSSCs.

Up to now, hundreds of organic dye molecules are synthesized, many of them have been examined in many applications [52]. Coumarin, which is one of alternative dyes, can be classified as a member of benzopyrone, which consists of fused benzene and pyrone rings. It is a substance naturally present in many plants and essential oils. Here, the fused benzene means a structure where benzene rings is the basic unit of larger polycyclic aromatic. Pyrone is described as including a ketone functional group and an unsaturated ring having one oxygen atom. Various coumarins are used in a wide range of many applications in both industrial and clinical areas, such as blue-green laser dyes, optical bleaching agents, and cancer therapy. In addition, coumarin and its compounds are successfully applied in organic dye-sensitized solar cells, since the electron injection process actualizes very fast with strong coupling of the dye and semiconductor, especially in the case of Coumarin 343 with  $\text{TiO}_2$  [65]. Therefore, Coumarin-343 dye used as organic dye photosensitizer has been obtained highly efficient DSSCs [66]. Similarly, formation of a strong coupling between  $\text{TiO}_2$  and Coumarin 153 (C153) [67] was observed. But the claim that this involves strong coupling needs to be further examined. These types of molecules do not have any carboxyl groups, in contrast to many other organic dye molecules. Therefore, we have investigated interaction between C153 and anatase surface in this thesis.

In this thesis, we have investigated the structural, electronic and optical properties of  $\text{TiO}_2$  (101) anatase surface with impurity atoms or molecules by using Hubbard-corrected Density Functional Theory (DFT+ $U$ ). The chapters of this thesis are organized as follows: After the Introduction part, the second chapter begins with a brief overview of the standard DFT techniques and approximations, thereafter we elaborate on the specifics of the Hubbard correction term. Finally, we discuss how to calculate the dielectric constant by using DFT+ $U$  and how to obtain the absorbance value from these results. Here, we only have discussed the main points about this theory and its relation to this thesis, as it is used in the calculations. In chapter 3, the modification of electronic, structural and optical properties of the anatase surface with adsorption of Pr are investigated. In addition, we examine the adsorption behavior of the Pr atom

by changing the value of  $U$ . In chapter 4, we study the behavior of adsorption of dissociative and nondissociative benzoic acid on both the  $\text{TiO}_2$  (101) surface and the surface with a Pr impurity. In chapter 5, we examine the  $\text{TiO}_2$  surface and the surface doped with a Pr atom and their interaction with Coumarin 153 dye molecule. Also, the physical properties of interaction of Coumarin 153 with a surface reduced by an oxygen vacancy are analyzed. In chapter 6, the interaction of other lanthanide atoms such as Gd Er and Lu with the surface and benzoic acid are studied. In chapter 7, namely Conclusion part, the obtained results are shortly outlined.



## CHAPTER 2

### THEORETICAL BACKGROUND

In this chapter, the theoretical approximations and approaches used in Density Functional Theory (DFT) based methods will be presented [68, 69].

#### 2.1 The problem of structure of matter

It is a complex problem to describe the physical and chemical properties of matter at the microscopic scale. In general, we handle a collection of interacting atoms, which may also be affected by some external field. This ensemble of particles may be in the gas phase (molecules and clusters) or in a condensed phase (solids, surface, wires). However, in any case the system can be described as a set of atomic nuclei and electrons interacting via Coulomb forces. Therefore, the Hamiltonian of such a system can be written in the following general form:

$$\hat{H} = \hat{H}_{el} + \hat{H}_{nucl} \quad (2.1)$$

where

$$H_{el} = - \sum_{i=1}^N \frac{\hbar^2}{2m} \nabla_i^2 + \frac{e^2}{8\pi\epsilon_0} \sum_{i=1}^N \sum_{j \neq i}^N \frac{1}{|\mathbf{r}_i - \mathbf{r}_j|} - \frac{e^2}{4\pi\epsilon_0} \sum_{I=1}^P \sum_{i=1}^N \frac{Z_I}{|\mathbf{R}_I - \mathbf{r}_i|} \quad (2.2)$$

$$H_{nucl} = - \sum_{I=1}^P \frac{\hbar^2}{2M_I} \nabla_I^2 + \frac{e^2}{8\pi\epsilon_0} \sum_{I=1}^P \sum_{J \neq I}^P \frac{Z_I Z_J}{|\mathbf{R}_I - \mathbf{R}_J|} \quad (2.3)$$

where  $\mathbf{r}_i$ , ( $i = 1, \dots, N$ ) is a set of  $N$  electron coordinates and  $\mathbf{R}_I$ , ( $I = 1, \dots, P$ ) is a set of  $P$  nuclear coordinates. The factor of  $\frac{1}{2}$  has been included in order to avoid double counting of terms in the series representation.

In principles, all the properties can be derived by solving the time independent many-body Schrödinger equation;

$$H\Psi_n(\mathbf{R}, \mathbf{r}) = \varepsilon_n \Psi_n(\mathbf{R}, \mathbf{r}) \quad (2.4)$$

where  $\varepsilon_n$  are energy eigenvalues and  $\Psi_n(\mathbf{R}, \mathbf{r})$  are the corresponding eigenstates or wave functions, which must be antisymmetric with respect to exchange of electronic coordinates in  $r$ , since electrons are fermions. Nuclei of the same species also obey the same rule because of their nuclear spin, so that eigenstate or wave function must be symmetric or antisymmetric with respect to exchange of nuclear variables in  $R$ .

## 2.2 Pre-Density Functional Theory

### 2.2.1 Hartree and Hartree-Fock approximation

The main problem in the structure of matter is to solve the Schrödinger equation of a many-particle system in the external Coulombic field created by a collection of atomic nuclei. In order to achieve this, approximations are in order. The first approximation to solve the many-body problem was proposed by Hartree [70], which is a variational wave function based approach. The basic assumption of it is a simple product of single-particle orbitals. In the Hartree approximation, the electrons are considered as occupying single particle orbitals which are determine the wave function. Each electron feels the electrostatic field which is due to the central potential of the nucleus together with the field created by the other electrons. In this case, the approximate wave function can be written as

$$\Phi(\mathbf{x}_1, \mathbf{x}_2, \dots, \mathbf{x}_N) = \phi_1(\mathbf{x}_1)\phi_2(\mathbf{x}_2) \dots \phi_N(\mathbf{x}_N) \quad (2.5)$$

and the one-particle Schrödinger equation proposed by Hartree is,



$$\left( -\frac{\hbar^2}{2m} \nabla^2 + V_{ext}(\mathbf{R}, \mathbf{r}) + \int \frac{\sum_{j \neq i}^N |\phi_j(\mathbf{r}')|^2}{|\mathbf{r} - \mathbf{r}'|} d\mathbf{r}' \right) \phi_i(\mathbf{r}) = \varepsilon_i \phi_i(\mathbf{r}) \quad (2.6)$$

where the third term on the left hand side is the classical electrostatic potential due to the charge distribution of all the other electrons. Therefore the third term is called the Hartree potential. Sum of the second and third terms is the effective potential. In the Hartree formulation makes the electron–electron interaction counted twice. The correct energy expression is

$$E^H = \sum_{i=1}^N \varepsilon_i - \frac{1}{2} \int \int \frac{\rho_i(\mathbf{r}) \rho_j(\mathbf{j})}{|\mathbf{r}_i - \mathbf{r}_j|} d\mathbf{r}_i d\mathbf{r}_j. \quad (2.7)$$

where  $\rho_i(\mathbf{r}) = |\phi_i(\mathbf{r})|^2$ . The problem of Hartree approximation is such that it does take the electrons as distinguishable particles, However electrons are indistinguishable spin- $\frac{1}{2}$  particles and the obey Pauli exclusion principle. If two electrons are exchange, the wave function must change sign. Thus, a Slater determinant is formed from the one–particle orbitals in order to achieve the correct antisymmetric wavefunction [71],

$$\Phi_{HF}(x_1, x_2, \dots, x_N) = \frac{1}{\sqrt{N!}} \begin{vmatrix} \phi_1(1) & \phi_2(1) & \cdots & \phi_N(1) \\ \phi_1(2) & \phi_2(2) & \cdots & \phi_N(2) \\ \vdots & \vdots & \ddots & \vdots \\ \phi_1(N) & \phi_2(N) & \cdots & \phi_N(N) \end{vmatrix} \quad (2.8)$$

$$\Phi_{HF} = \frac{1}{\sqrt{N!}} \sum_{i=1}^N (-1)^{P(i)} \phi_{i1}(\mathbf{x}_1) \phi_{i2}(\mathbf{x}_2) \dots \phi_{iN}(\mathbf{x}_N) \quad (2.9)$$

This wave function allows particle exchange in the correct manner. The approximation consists of the wave function in the form (2.14) is called Hartree–Fock (HF) or self consistent field (SCF) model. HF equation provides good description of inter-atomic bonding but many-body correlations are completely ignored.

## 2.2.2 Thomas–Fermi Theory

Thomas and Fermi, independently of each other, gave a perspective for constructing the total energy in terms of the electronic density without using one-electron orbitals [72]. They proposed the expression for the kinetic, exchange, and correlation energies of the homogenous electron gas to construct the same quantities for the inhomogenous system as;  $E_\alpha[\rho] = \int \rho(\mathbf{r})\varepsilon_\alpha[\rho(\mathbf{r})]d\mathbf{r}$  where  $\varepsilon_\alpha[\rho(\mathbf{r})]$  is the energy, (a functional of density) of a homogenous electron gas corresponding with  $\rho(\mathbf{r})$ . This idea was the first time that the local density functional approximation (LDA) was used. The relationship between the Fermi energy and density for homogenous electron gas is given by;

$$\rho = \frac{1}{3\pi^2} \left( \frac{2m}{\hbar^2} \right)^{3/2} \epsilon_F^{3/2} \quad (2.10)$$

and the kinetic energy of the homogenous gas is  $T = 3\rho\epsilon_F/5$ . When it is used with electron density formula, the kinetic energy density formulation can be derived in a similar manner. Finally, total energy expression without exchange and correlation can be obtain in Thomas–Fermi theory as,

$$E_{TF}[\rho] = C_k \int \rho(\mathbf{r})^{5/3} d\mathbf{r} + \int \rho(\mathbf{r})v_{ext}(\mathbf{r})d\mathbf{r} + \frac{1}{2} \int \int \frac{\rho(\mathbf{r})\rho(\mathbf{r}')}{|\mathbf{r} - \mathbf{r}'|} d\mathbf{r}d\mathbf{r}' \quad (2.11)$$

where  $C_k = 3(3\pi^2)^{2/3}/10 = 2.871$  in atomic units. Thomas–Fermi theory does not have the exchange and correlation effects and Hartree equation described the ground states even better than that. However, it contains the fundamental ideas necessary for the development Density Functional Theory.

## 2.3 Modern Density Functional Theory

### 2.3.1 Hohenberg–Kohn Theory

Two main theorems were proposed by Hohenberg–Kohn (HK) in 1964 [73] that forms the foundation of density functional theory (DFT)

1. For any system of interacting particles the ground state energy is a unique functional of the particle density,  $E_0 = E[\rho(\mathbf{r})]$ . There cannot be two different external potentials  $v(\mathbf{r}) \neq v'(\mathbf{r})$  that correspond to the same electronic density for the ground state.
2. The minimum value of the functional  $E = E[\rho(\mathbf{r})]$  for the energy can be define by variations  $\delta\rho(\mathbf{r})$  of the particle density at equilibrium density  $\rho_0(\mathbf{r})$ ,

$$E = E[\rho_0(\mathbf{r})] = \min\{E[\rho(\mathbf{r})]\} \quad (2.12)$$

### 2.3.2 Self-consistent Kohn–Sham equations

The Hartree term refers to the classical electrostatic energy, which is known exactly for the electron-electron problem. However, the kinetic energy  $T = \langle \Phi | \hat{T} | \Phi \rangle$  cannot be expressed directly in terms of the density. Kohn and Sham introduced an auxiliary system with the same density as the real system,

$$E_{KS}[\rho] = T_R[\rho] + \int \rho(\mathbf{r})v_{ext}(\mathbf{r})d\mathbf{r} + \frac{1}{2} \int \int \frac{\rho(\mathbf{r})\rho(\mathbf{r}')}{|\mathbf{r} - \mathbf{r}'|} d\mathbf{r}d\mathbf{r}' + E_{XC}[\rho] \quad (2.13)$$

where the density is the writtena as  $\rho(\mathbf{r}) = \sum_i |\phi_i(\mathbf{r})|^2$  in terms of unspecified sing-particle orbitals, and  $E_{XC}[\rho]$  is the exchange-correlation functional. The energy functional has been expressed in terms of the KS orbitals ( $N_s$ ) by this formula, which minimizes the non-interacting electronic kinetic energy under the fixed number of electrons constraint. Although Kohn–Sham orbitals do not have a clear meaning by themselves, they have been proven to describe the density of states fairly correctly.

### 2.4 Functionals for Exchange and Correlation

The exchange energy ( $E_X$ ), and correlation energy terms ( $E_C$ ) are not known in explicit form. Several approximations have been developed to best represent these terms.

### 2.4.1 The Local Density Approximation (LDA)

The local density approximation [74] or spin polarized systems local spin density approximation (LSDA) is one of the most widely used approximations to calculate the exchange–correlation energy. The main idea is to assume generally an electronic system as locally homogenous, for which to use the exchange–correlation hole corresponding to the homogenous gas. In practice, the exchange–correlation terms local in the density is an integral over all space with the exchange–correlation energy density at each point in the volume.

$$E_{XC}^{LDA}[\rho] = \int \rho(\mathbf{r})\epsilon_{XC}^{LDA}[\rho(\mathbf{r})]d\mathbf{r} \quad (2.14)$$

where,  $\epsilon_{XC}^{LDA}$  is exchange–correlation energy density of the system and its value is in terms of the exchange–correlation hole,

$$\epsilon_{XC}^{LDA}[\rho] = \frac{1}{2} \int \frac{\rho_{XC}^{LDA}(\mathbf{r}, \mathbf{r}')}{|\mathbf{r} - \mathbf{r}'|} d\mathbf{r}'. \quad (2.15)$$

L(S)DA works the best for solids where the electron density is close to homogeneous gas. However, it can be used that of if the following points are kept in mind.

1. It favours more homogenous systems.
2. It gives overestimated binding energies for molecules and solids.
3. The geometries of systems involving strong bonds (covalent, ionic, and metallic) are described well within the LDA. But, the description of systems involving weak bonds (hydrogen or van der Waals) are failed within the LDA
5. Chemical trends such as ionization potential are usually correct.

Although L(S)DA is a very successful approximation, it is known to fail to reproduce some properties. Some important ones are;

- i) Electronic densities of atoms in the core region are poor because LDA fails to cancel the self-interaction.

ii) Non-local correlation effects are not taken into account inherently by the LDA.

iii) The energy band gap within LDA is smaller than the true band gap.

iv) Strongly correlated systems such as transition metal oxides are poorly characterized by LDA.

## 2.4.2 Generalized Gradient Approximation (GGA)

The matter of electronic density of inhomogeneous systems are carried out with an expansion of the density in terms of the gradient and higher order derivatives. In general, the exchange–correlation energy in the basic form can be written as;

$$E_{XC}[\rho] = \int \rho(\mathbf{r})\varepsilon_{XC}[\rho(\mathbf{r})]d\mathbf{r} + \int F_{XC}[\rho(\mathbf{r}), \nabla\rho(\mathbf{r}), \nabla^2\rho(\mathbf{r}), \dots]d\mathbf{r} \quad (2.16)$$

where the function  $F_{XC}$ , modifies the LDA expression relative to the variation of the density. Naturally, all the formal properties cannot be enforced at the same time. Numerous forms for  $F_{XC}$  have been proposed by Langreth–Mehl, Becke–Lee–Yang–Parr (BLYP), Perdew–Wang (PW91), and Perdew–Burke–Erzerhof (PBE). We only explain here our choice in this thesis, namely the PBE functional in the calculations.

### 2.4.2.1 PBE functional

Perdew, Burke, and Erzerhof (PBE) functional approximation can propose to solve one problem in the GGAs. It is originated from that the reduced to the second order gradient expansion for density variations are small. The result of this case, the linear response of a uniform gas is described with GGAs less satisfactory than L(S)DA [75].

The general trends of GGAs concerning improvements over the LDA are following:

1. They enhance binding and atomic energies.
2. They improve bond lengths and angles.
3. They improve energetics, geometries, and dynamical properties of water, ice, and water clusters. Especially, BLYP and PBE show best agreement with experimental results in terms of these. In general, although, they are not clear the description of F–H bond, this improves for the case of hydrogen-bounded systems.
4. Semiconductors are marginally better described within the LDA than in GGA, except for the binding energies.
5. For the 4d–5d transition metals the improvement of the GGA over the LDA is not clear.
6. Lattice constant of noble metals (Au, Ag, Pt) are overestimated in GGA, while they are closer to the experimental results in LDA.

## 2.5 Pseudopotentials

The concept of "pseudopotential" in electronic structure is related to the replacement of the strong Coulomb potential due to the nucleus, on the effects of the tightly bound core electrons, by an effective ionic potential acting on the valence electron. In other words, a pseudopotential is used to compute properties of valence electron due to unchanged core electron states into different chemical environments and considered the valence wave functions orthogonality to the core states. The pseudopotential process to be reproduced starts within independent-particle approximation, just like in the Kohn–Sham density functional approach. The valence states are seen to oscillate rapidly in the region occupied by the core electrons because of the strong ionic potential in this region. These oscillations sustain the orthogonality between the core and valence states due to Pauli exclusion principle. The valence state generated from pseudopotential construction leads to smoother pseudo-function because the resulting potential is a much weaker one than the original potential.

Pseudopotential calculations are based upon "*ab initio*" norm-conserving potentials in the most modern applications. Pseudopotentials require "norm-conserving" property in order to provide accurate and transferable potential, which provides that although the valence properties are defined in different environments such as atoms, molecules, and ions, they can be rightly described by pseudopotential constructed in one environment. We presented two of many different types of approximations in order to create smooth, transferrable, and accurate pseudofunctions in this subsection.

### 2.5.1 Ultrasoft Pseudopotential

One approach is known as "ultrasoft pseudopotentials" [76] which provides accurate calculations by transformation that rewrites the non-local potential in a form involving a smooth and an auxiliary function around each ion core having the rapidly varying part of the densities. Thus, the smaller the planewave cut-off, the smaller the number of planewaves that is required by this way. Smooth functions that represent each atomic state are the solution of the generalized eigenvalue problem.

### 2.5.2 Projector Augmented Waves

The projector augmented wave (PAW) [77] method is a general approach to a solution of electronic problem that reformulates the formal simplicity of the traditional plane-wave pseudopotential approach, adapting it to modern techniques for calculation of the total energy, forces, and stress. It introduces projectors and auxiliary localized functions similar to the ultrasoft pseudopotential method. Also, the total energy is described a functional in the PAW approach and it uses advanced algorithms for efficient solutions of the generalized eigenvalue problem. However, calculations in the PAW approach based on all-electron wavefunctions, so it recovers the wavefunction with the core region of atoms as well. Hence, this method can be incorporated into existing pseudopotential codes with relatively minor additional effort.

## 2.6 Numerical Calculations

We have used Vienna *Ab-initio* Simulation Package (VASP) for our *ab initio* calculations. VASP allows the electronic structure of the system with periodic boundary conditions to be calculated using ultrasoft Vanderbilt pseudopotentials, or the Projected Augmented Wave method, and a plane wave basis set. All calculations are performed within the DFT formalism.

## 2.7 Hubbard corrected density functional theory (DFT+U)

Description of strongly correlated systems (such as transition metal or rare earth oxides) is a significant challenge for Density Functional Theory (DFT). Although DFT is a successful method in order to identify magnetic and structural properties of these systems, the electronic properties of them cannot accurately be predicted with the help of the method.

Over the years many ideas were developed to overcome these challenges. Among them, the most recognized are self-interaction-correction local spin density approximation (SIC-LSDA), hybrid functionals, and LDA+U. The LDA+U (or GGA+U), Hubbard-modeled corrections, is particularly useful as the simplest and the most effective method. The Hubbard formula is derived from an approximation to the more general Hamiltonian. The Hubbard Hamiltonian  $H_H$  can be written as follows;

$$H_H = -t \sum_{ij\sigma} c_{i,\sigma}^\dagger c_{j\sigma} + U \sum_i n_{i\uparrow} n_{i\downarrow} \quad (2.17)$$

where  $i$  is over lattice sites and  $j$  is over the neighbors of  $i$ . Also,  $c_{i,\sigma}^\dagger$ ,  $c_{j\sigma}$ , and  $n_{i\sigma} = c_{i\sigma}^\dagger c_{i\sigma}$  represent creation, annihilation and number operators for the electron of spin  $\sigma$  on site  $i$ , respectively. This presentation is known as the single-band Hubbard formulation. In here, the hopping is restricted to the nearest neighboring sites for one band (amplitude  $t$  represents single-particle terms of the electronic energy) and the parameter  $U$  represents the strength of the Coulomb



interaction for between electrons on the same atom. The main idea of LDA+U (or GGA+U) is to add into DFT by a correction term that obviously accounts for "on-site" electron-electron interactions. The formulation of LDA+U total energy functional of a system is generally represented as;

$$E_{LDA+U} = E_{LDA} + E_U = E_{LDA} + E_{Hub} - E_{dc} \quad (2.18)$$

In this formulation,  $E_{LDA}$  is the energy term used in DFT calculations, and  $E_{Hub}$  contains electron-electron interactions as modeled in the Hubbard Hamiltonian. This means that the formulation contains only interaction term of Hubbard Hamiltonian ( $U \sum_i n_{i\uparrow} n_{i\downarrow}$ ) for localized d or f electrons.  $E_{dc}$  is a mean-field approximation to the correction "on-side" correlation functional ( $E_{Hub}$ ), which models the electron correlation contained in  $E_{LDA}$ . This term is subtracted from the total energy to avoid double counting of the interactions contained in  $E_{Hub}$ . The double counting term is  $UN(N-1)/2$ , where  $N = \sum_i n_i$ . Therefore, a basic formulation of the total energy can be written as,

$$E_{LDA+U} = E_{LDA} + \frac{U}{2} \sum_{i \neq j} n_i n_j - \frac{U}{2} N(N-1) \quad (2.19)$$

When we take the interaction term of Hubbard Hamiltonian,

$$E_{Hub} = U \sum_i n_{i\uparrow} n_{i\downarrow} = \sum_{nn'mm'} \sum_{\sigma, \sigma'} U_{nnmm'} c_{n,\sigma}^\dagger c_{m,\sigma'}^\dagger c_{n',\sigma'} c_{m',\sigma} \quad (2.20)$$

If  $\sigma \neq \sigma'$ , then

$$c_{n,\sigma}^\dagger c_{m,-\sigma}^\dagger c_{n',-\sigma} c_{m',\sigma} = c_{n,\sigma}^\dagger c_{m',\sigma}^\dagger c_{m,-\sigma} c_{n',-\sigma} = n_{nm}^\sigma n_{m'n'}^{-\sigma} \quad (2.21)$$

and the matrix element representation is;

$$\begin{aligned} U_{nnmm'} &= \frac{1}{2} \int d\mathbf{r} d\mathbf{r}' \psi_n^\dagger(\mathbf{r}) \psi_{n'}^\dagger(\mathbf{r}') V(\mathbf{r} - \mathbf{r}') \psi_m(\mathbf{r}) \psi_{m'}(\mathbf{r}') \\ &= \frac{1}{2} \langle nm | V_{ee} | n'm' \rangle \end{aligned} \quad (2.22)$$

If  $\sigma = \sigma'$ , we have two possibilities;

$$c_{n,\sigma}^\dagger c_{m,\sigma}^\dagger c_{n',\sigma} c_{m',\sigma} = \begin{cases} c_{n,\sigma}^\dagger c_{m',\sigma} c_{m,\sigma}^\dagger c_{n',\sigma} = n_{nm'}^\sigma n_{mn'}^\sigma \\ -c_{n,\sigma}^\dagger c_{n',\sigma} c_{m,\sigma}^\dagger c_{m',\sigma} = -n_{nn'}^\sigma n_{mm'}^\sigma \end{cases} \quad (2.23)$$

$E_{Hub}$  and  $E_{dc}$  can be given general expression;

$$E_{Hub} = \frac{1}{2} \sum_{nm,\sigma} \langle nm | V_{ee} | m'n' \rangle n_{nm'}^\sigma n_{mn'}^{-\sigma} \quad (2.24)$$

$$+ (\langle nm | V_{ee} | m'n' \rangle - \langle nm | V_{ee} | n'm' \rangle) n_{nm'}^\sigma n_{mn'}^\sigma$$

$$E_{dc} = \frac{U}{2} N(N-1) - \frac{J}{2} (N^\uparrow(N^\uparrow-1) + N^\downarrow(N^\downarrow-1)) \quad (2.25)$$

where  $U$  and  $J$  are screened Coulomb and exchange parameters. The  $V_{ee}$  integrals in eq. (8) describe the Coulomb interaction among  $d$  electrons sitting on the same site.

If we want to write the relation between  $U$  and  $V_{ee}$  or  $J$  and  $V_{ee}$ . Before the integral representation of  $\langle nm | V_{ee} | m'n' \rangle$  in the spherical coordinate is get;

$$\langle nm | V_{ee} | m'n' \rangle = \int d\mathbf{r} d\mathbf{r}' R_{ln}^*(\mathbf{r}) Y_{ln}^* R_{lm'}(\mathbf{r}) Y_{lm'} V(\mathbf{r} - \mathbf{r}') R_{lm}(\mathbf{r}') Y_{lm} R_{ln'}(\mathbf{r}') Y_{ln'}^* \quad (2.26)$$

then, the Coulomb potential is written in terms of spherical harmonics

$$V(\mathbf{r} - \mathbf{r}') = \frac{1}{\epsilon} \frac{1}{|\mathbf{r} - \mathbf{r}'|} = \frac{1}{\epsilon} \sum_{l=0}^{\infty} \frac{4\pi}{2l+1} \frac{r_{<}^l}{r_{>}^{l+1}} \sum_{m=-l}^l Y_{lm}(r) Y_{lm}^*(r') \quad (2.27)$$

and

$$\langle nm | V_{ee} | m'n' \rangle = \sum_{l'=0}^{\infty} \frac{4\pi}{2l'+1} \frac{r_{<}^{l'}}{r_{>}^{l'+1}} \sum_{p=-l'}^l \langle ln | Y_{l'k} | lm' \rangle \langle lm | Y_{l'k}^* | ln' \rangle F^{l'} \quad (2.28)$$

where,  $0 \leq l' \leq 2l$ ,  $l$  is the angular moment of Hubbard electrons. The  $F^{l'}$  coefficients, that in Hartree-Fock (HF) theory are the radial Slater integrals representing the bare electron-electron interaction, in the formulation of the LDA+U functional are treated as parameters that represent screened electronic couplings. For d electrons only  $F^0$ ,  $F^2$ , and  $F^4$  are necessary

$$U = \frac{1}{(2l+1)^2} \sum_{nn'} \langle nn' | V_{ee} | nn' \rangle = F^0 \quad (2.29)$$

$$J = \frac{1}{2l(2l+1)} \sum_{n \neq n', n'} \langle nn' | V_{ee} | n'n \rangle = \frac{F^2 + F^4}{14}$$

## 2.8 Dielectric Matrix

In our optical absorption calculations, we make use of post processin tool using the KS orbitals. The frequency dependent dielectric matrix is calculated. The imaginary part is defined by a summation over empty states using the equation:

$$\xi_{\alpha\beta}^{(2)}(\omega) = \frac{4\pi^2 e^2}{\Omega} \lim_{q \rightarrow 0} \frac{1}{q^2} \sum_{c,v,\mathbf{k}} 2\omega_{\mathbf{k}} \delta(\epsilon_{c\mathbf{k}} - \epsilon_{v\mathbf{k}} - \omega) \times \langle u_{c\mathbf{k}} + c_{\alpha q} | u_{v\mathbf{k}} \rangle \langle u_{c\mathbf{k}+c_{\beta}\mathbf{q}} | u_{v\mathbf{k}} \rangle \quad (2.30)$$

here the indices  $c$  and  $v$  refer to conduction and valence band states respectively, and  $u_{c\mathbf{k}}$  is the cell periodic part of the orbitals at the  $\mathbf{k}$ -point  $\mathbf{k}$ . The real part of the dielectric tensor  $\epsilon^{(1)}$  is obtained by the usual Kramers-Kronig transformation

$$\xi_{\alpha\beta}^{(1)}(\omega) = 1 + \frac{2}{\pi} P \int_0^\infty \frac{\xi_{\alpha\beta}^{(2)}(\omega') \omega'}{\omega'^2 - \omega^2 + i\eta} d\omega' \quad (2.31)$$

where  $P$  denotes the principle value. The corresponding absorption spectrum was estimated by the following equation;

$$I(\omega) = 2\omega \left( \frac{(\xi_1^2(\omega) + \xi_2^2(\omega))^{\frac{1}{2}} - \xi_1(\omega)}{2} \right)^{\frac{1}{2}} \quad (2.32)$$

where  $I$  is the optical absorption coefficient,  $\omega$  is the angular frequency ( $E = \hbar\omega$ ) [101].

## CHAPTER 3

### PR ADSORBED ON (101) ANATASE SURFACE

In this chapter, we methodically study Pr impurities on the TiO<sub>2</sub> anatase (101) surface. We present our band structure calculations as a function of the empirical parameter  $U$  in an attempt to quantify its effect on materials properties.

#### 3.1 Computational Method

First principle total energy calculations were performed within DFT+U by means of plane-wave basis sets and the projector augmented wave (PAW) potential [77]. The Perdew–Burke–Ernzerhof (PBE) [75] functional of the generalized gradient approximation (GGA) [78] has been used to calculate the exchange–correlation effects. The valence atomic configurations used for the PAW potentials are 3d<sup>3</sup> 4s<sup>1</sup> for Ti, 2s<sup>2</sup> 2p<sup>4</sup> for O, and 5s<sup>2</sup> 5p<sup>6</sup> 4f<sup>3</sup> 6s<sup>2</sup> for Pr. The charge analysis was done using the Bader method [80, 81]. The cut off energy was 500 eV. Hubbard  $U$  is calculated using Dudarev’s approximation with a combined  $U$ – $J$  term acting on Ti 3d and Pr 4f states [79]. The Brillouin zone integrations have been carried out using the Monkhorst-Pack scheme. With,  $8 \times 8 \times 8$  and  $11 \times 11 \times 11$   $k$ -point meshes for our TiO<sub>2</sub> and Pr<sub>2</sub>O<sub>3</sub> bulk structures calculations, respectively.  $4 \times 4 \times 1$   $k$ -point mesh were used for our TiO<sub>2</sub> (101) surface calculations. A three-layer slab model was used to describe (101) surface, as shown Fig. 3.2(a). The  $2 \times 1$  unit in the surface plane comprised of  $7.82 \text{ \AA} \times 10.36 \text{ \AA} \times 25.04 \text{ \AA}$  dimensions with a vacuum space of nearly  $15 \text{ \AA}$  to prevent from any interactions between periodic structures.

## 3.2 Result and Discussions

### 3.2.1 Hubbard Correction Term

The issue surrounding the correct choice of the empirical  $U$  can be addressed by examining changes in the physical properties of system as a function of this parameter. In our calculations, in order to determine the  $U_{eff} = U - J$  (setting  $J = 0$ ) for Ti atom, our calculated values in terms of lattice constant, and band gap for TiO<sub>2</sub> bulk has been compared with the available experimental data. Lattice constants were calculated the as to following way. First we constructed a periodic boundary lattice using the known positions of atoms. A starting lattice constant was chosen close to the experimental one. After a curve identifying the relationship between these varying lattice constants and energy was drawn. The final lattice constant corresponding to the lowest energy was chosen. This calculation was repeated for each  $U$ . The band structures were calculated for each the lattice constants. The band structure are shown in Figure 3.1 for  $U=5$  eV. Here, the critical issue is that the lattice constants increase with respect to their values in plain DFT, while the theoretical value of the band gap approaches the experimental value. Therefore, with increased  $U$  value, we can obtain the correct band gap of the system, but begin to disrupt its atomic structure. Table 3.1 displays the lattice constants and band gaps of a wide range of  $U$  values. For small  $U$  values, the lattice constants are closer to experimental values while the band gaps are inconsistent. For example, a  $U$  value of 2 eV yields a band gap of 2.14 eV which is very different from the experimental value of 3.2 eV [87] while the lattice constants are estimated to within 2.5%. In terms of table 3.1, the value of  $U$  can be fixed 8 eV for obtain the correct band gap. However, this value causes large distortions in anatase bulk with up to 4% error in the lattice constants. The value of  $U = 5$  eV is a fair compromise leading to the optimal a band gap of 2.65 eV for the bulk and 2.89 for surface anatase. In recent studies on TiO<sub>2</sub>, Selloni et al. [82], Pacchioni et al. [83], and Dompablo et al. [84] used the  $U$  parameters in the range of 2 to 4.5, 4, and 5 eV, respectively. In a different comparative study with experien.  $U$  was calculated in the range of 4 to 5 [85]. We have performed our calculations as  $U$  parameter for 4 and 6 values

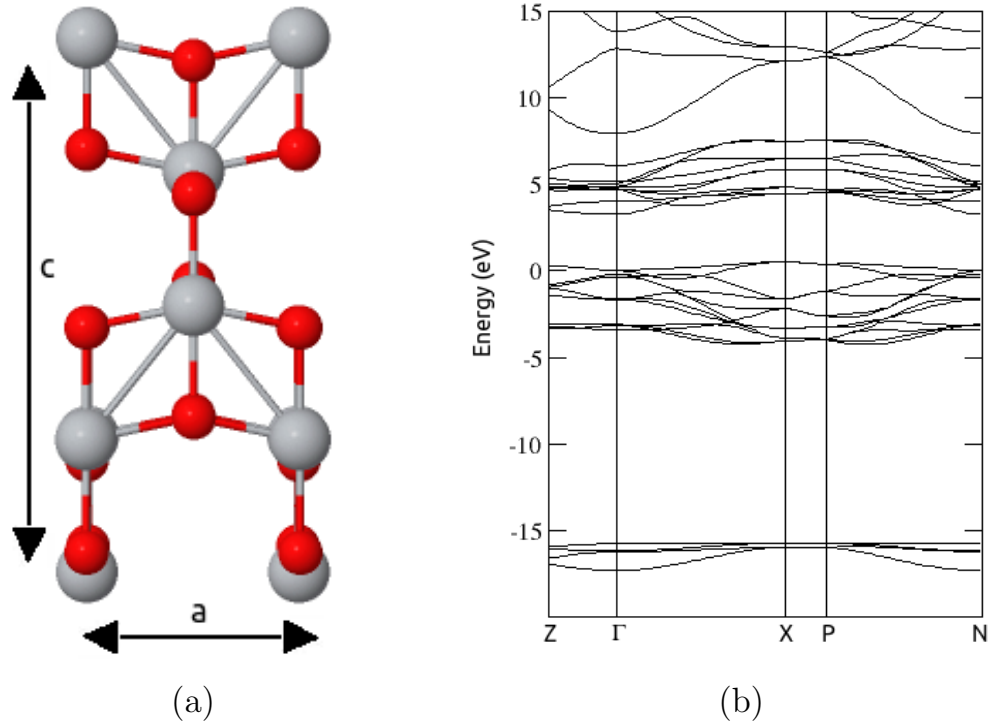


Figure 3.1: (a) Front views of the slab modeling the anatase bulk. (b) The electronic band structure are represented.

and analyzed the changes in the band structure. For each calculation, we have used the lattice parameters that compatible with the  $U$  value in question.

When the  $4f$  states of a single Pr atom are considered, a similar assessment is more challenging. In the literature, a definitive value of  $U$  for Pr has not been settled upon. Tran [86] *et al.* reported to be  $U = 6$  eV for Pr in the their study on bulk  $\text{PrO}_2$ . In another study on  $\text{PrO}_2$  5 eV was used [88]. In several applications ons rare earth titanate oxides, doped anatase bulk, and RE-perovskite crystal structures, appropriate value of  $U$  were found as to 5.5, 6.0 and 6.05 eV [89, 90, 91]. Unlike these studies, Spadavecchia *et al.* fixed 2 eV for  $4f$  Pr electrons  $U$  value [92].

Our calculation results for  $\text{Pr}_2\text{O}_3$  were listed Table 3.2. According to the Table, there is no linear relationship between the increase of the  $U$  value with the lattice constant. More irregular changes are observed. For example, while the lattice constant was found as 3.898 Å in case the  $U$  value of 2 eV, the constant

Table3.1: Unit cell parameters ( $\text{\AA}$ ) and band gaps for  $\text{TiO}_2$  anatase bulk obtained after complete structural optimization with PBE+U compared to experimental data.

	$E_g(\text{eV})$	$a(\text{\AA})$	$c(\text{\AA})$	$c/a$
exp [87]	3.20	3.78	9.51	2.51
U=0	1.91	3.83	9.65	2.51
U=1	2.03	3.85	9.66	2.51
U=2	2.14	3.87	9.65	2.49
U=3	2.32	3.88	9.71	2.50
U=4	2.48	3.89	9.74	2.50
U=5	2.65	3.91	9.77	2.50
U=6	2.82	3.93	9.78	2.49
U=7	3.02	3.94	9.82	2.49
U=8	3.22	3.96	9.85	2.48
U=9	3.12	3.98	9.87	2.48
U=10	3.04	3.99	9.91	2.48

can fall to 3.883  $\text{\AA}$  in the case the  $U$  value of 3 eV. Here, although the nearest value for the experimental lattice constant  $a$  seems to be for  $U$  value of 1 eV. the accuracy of band gap value is unclear due to contradicting experimental results. While Pourovskii *et al.* found as 3.90 eV [93], Kimura *et al.* found as 3.50 eV [94]. When we look at these theoretical results, our calculation for  $U$  value of 5 eV seem to be closer to these results. In these calculations, it is assumed that the  $f$ -orbitals as core orbitals in these theoretical calculations. However, in our calculations the  $f$ -orbitals were considered as valence. Taking reference to the band structure in our calculation, impurity states originating  $f$ -orbitals do not appear in the band gap for the  $U$  values of 4 eV or larger. Eventually, this value is consistent with other studies that used as of the Pr atoms,  $U$  value was chosen 5 eV for Pr  $4f$  states.



Table3.2: Unit cell parameters ( $\text{\AA}$ ) and band gaps for  $\text{Pr}_2\text{O}_3$  bulk structure obtained after complete structural optimization with PBE+U compared to experimental data.

	$a(\text{\AA})$	$c(\text{\AA})$	$E_g(\text{eV})$
exp	3.85 [96]	6.01 [96]	3.90 [93],3.5 [94]
theo	3.89 [95]	6.12 [95]	3.17 [97]
Pr:U=0	3.820	5.986	2.56
Pr:U=1	3.848	6.010	3.34
Pr:U=2	3.898	6.025	2.57
Pr:U=3	3.883	6.037	3.61
Pr:U=4	3.892	6.049	3.03
Pr:U=5	3.891	6.072	3.15
Pr:U=6	3.878	6.095	3.67
Pr:U=7	3.870	6.161	3.75

### 3.2.2 Adsorptional Case

Before presenting our results on the Pr-doped  $\text{TiO}_2$  anatase (101) surface, we first refer to the relaxed structure of the clean surface, as shown Fig 3.2. According to previous theoretical studies, the surface energies are expected to change as the function of the number of atomic layers [98]. In addition the terrace construction of anatase (101) surface augments the strength of adsorption of metal atoms on the surface [99]. Therefore, three  $\text{TiO}_2$  layers have been chosen in the slab for forming the surface. A  $2 \times 1$  surface unit has four two-fold oxygen atoms ( $\text{O}2c$ ) causing the edges of the terrace-like part, while six-fold coordinated Ti atoms ( $\text{Ti}_{6c}$ ) lie along the troughs. Also, four three-fold oxygen atoms ( $\text{O}3c$ ) and four five-fold titanium atoms ( $\text{Ti}5c$ ) along the flat part. The surface electronic band structure is shown in the rightmost panel of the atomic structure in Fig 3.2. After the adsorption processes, the difference between (CB) and (VB) decrease by 0.06 – 0.14 eV in comparison with the band gap of bare  $\text{TiO}_2$  (101) surface calculated with  $U = 5$  eV (2.89 eV). The minimum of conduction band at  $\Gamma$  and the highest filled band (surface state) is along the  $\overline{\Gamma\text{J}}$  direction. According to

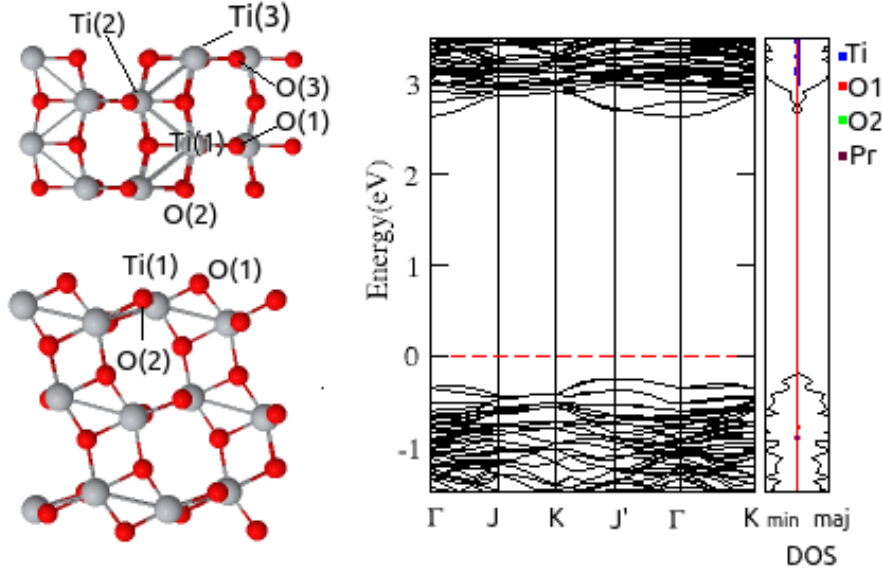


Figure 3.2: The geometric and electronic structures of  $\text{TiO}_2$  (101) surface. Oxygen, and titanium atoms are indicated red, and gray balls. Energy bands and DOS structures are represented rightmost panel of atomic structure figures.

the projected (local) density of state analysis, O atom states are more populated in the valence band which is mainly composed of Ti and O states (represented by the blue and red lines in PDOS, respectively).  $\text{O}2c$  atoms are more active at upper part of valence band. Moreover, Ti  $3d$  states are predominantly at the conduction band and  $\text{Ti}5c$  atoms are more active at low of there. As a result, it can be said that terrace-like part of surface is more reactive than the flat-like part of it for adsorption process.

For our initial Pr adsorption calculations, three stable adsorption configurations are identified for a  $U$  value of 5 eV for both Pr  $4f$  and Ti  $3d$ . These adsorption geometries are as shown in Figure 3.3. In the first geometry the Pr adsorption site is between  $\text{O}3c$  and  $\text{Ti}5c$  atoms, denoted as Pr(a-1); in the second between two edge  $\text{O}2c$  and  $\text{Ti}5c$  atoms, denoted as Pr(a-2); and in the third between  $\text{O}2c$  and  $\text{Ti}6c$  atoms located on the step-like surface construction, and also represented as Pr(a-3). Here, we focus on two adsorption forms. In the first, Pr atom directly interact with Ti atoms and significant degradation was observed on the surface, referred as the Pr(a-1) model. In the second, the most favorable

Table3.3: Adsorption energies (eV), magnetic moments ( $\mu_B$ ), and interatomic distances ( $\text{\AA}$ ) of the three Pr adsorption configurations shown in Fig. 3.3.  $U_{Ti}$  and  $U_{Pr}$  are both 5 eV.

	$\mu$	$E^{ads}$	Distances					
			Ti-Ti	Ti-O1	Ti-O2	Pr-Ti	Pr-O1	Pr-O2
TiO <sub>2</sub> (101)			3.12	1.88	2.03			
Pr( <i>a</i> -1)	5.00	3.06	2.95	2.35	2.21	2.81	2.21	
Pr( <i>a</i> -2)	3.00	6.92	3.02	2.10	2.11	3.23	2.19	2.40
Pr( <i>a</i> -3)	5.00	4.04	2.99	2.09	2.15	3.32	2.28	2.22

adsorption structure of Pr was referred as Pr(*a*-2). In the following sections, we will especially elaborate on these configurations. But we now return to the main topic of this part, namely the properties of these geometries.

The strength of the Pr-surface interaction can be described via the adsorption energy( $E^{ads}$ ). This energy can be calculated used formula as

$$E^{ads} = (E_{TiO_2} + E_{Pr} - E_{TiO_2+Pr}) \quad (3.1)$$

where  $E_{TiO_2}$ ,  $E_{Pr}$ , and  $E_{TiO_2+Pr}$  represent the total energy of the relaxed TiO<sub>2</sub> clean slab, the energy of one isolated Pr atom, and the total energy of the (slab+Pr) structure, respectively. The adsorption energies and relevant optimized structural values of Pr in all three configurations were in listed table 3.3. The adsorption energies for all cases have been found as 3.09 eV for Pr(*a*-1), 6.95 eV for Pr(*a*-2), and 4.07 eV for Pr(*a*-3). The average Pr-Ti, Pr-O1 and Pr-O2 distances are found as 3.23  $\text{\AA}$ , 2.19  $\text{\AA}$ , and 2.40  $\text{\AA}$ , respectively. The angle value of Ti-Pr-O1 is found as 40.1° to be. For Pr(*a*-1), both bond lengths of Pr-Ti and Pr-O are found as 2.81  $\text{\AA}$  and 2.21  $\text{\AA}$ , also the angle of O1-Pr-Ti is 54.2°. For Pr(*a*-3) case, both bond lengths of Pr-Ti and Pr-O are found as 3.32  $\text{\AA}$  and 2.22  $\text{\AA}$ , and O1-Pr-O2 and Ti-Pr-O angles are 78.2° and 39.8°, respectively. The increase in the bond lengths between Ti and O1 is observed in Pr(*a*-1), where Ti atom has been shifted down from surface about 0.5  $\text{\AA}$ .

The electronic features of these geometries were studied via spin-polarized band

Table 3.4: Bader charge of Pr adsorbed on the surface in three different configuration. In Hubbard  $U$  value used in the different for the  $U_{Ti}$  and  $U_{Pr}$  are fixed as 5 eV.

	Charges					
	Ti1	Ti3	O1	O2	O3	Pr
TiO <sub>2</sub> (101)	+2.04	+2.03	-0.91	-1.08	-0.91	
Pr( $a-1$ )	+1.87		-1.32			+1.44
Pr( $a-2$ )	+1.81	+1.81	-1.34	-1.45	-1.19	+1.96
Pr( $a-3$ )	+2.05		-1.14	-1.24		+1.52

structure and density of states graphs, indicated in rightmost panel of Figure 3.2. The CB minimum is along the  $\overline{JT}$  direction and the highest filled band (surface state) is at  $J'$  for all band structures of forms. When evaluated together with the band and the PDOS graphs, for Pr( $a-1$ ), two full occupied impurity states is located below the Fermi energy and in the band gap. The Fermi energy resides in the CB region. The Ti<sub>6c</sub> atom (Ti2) contributes more to the lower parts of the conduction band region. For the Pr( $a-3$ ), two full occupied impurity states is in the middle of band gap similar to Pr( $a-1$ ). However, O and Pr interaction is more reactive in these states. One occupied state originated from Ti (Ti<sub>6c</sub>) and Pr interaction resides near the CB region. The Fermi energy stands in the CB region. As for the band structure of Pr( $a-2$ ), in contrast to the other configurations, the Fermi level is situated in the middle of the band gap. Again, different from the others, both occupied and unoccupied impurity states are located in the band gap. While occupied states are originated from Pr-Ti and Pr-O interactions, orbitals of Pr are dominant in the unoccupied states placed up above the Fermi level.  $f$ -orbitals have a larger contribution for these states, although the effect of  $d$ -orbitals are present.

Bader analysis method is used for calculating partial atomic charges in this thesis. For  $U = 0$  value, the ions of bulk anatase are calculated to have charges  $Q_{Ti} = +2.64e$ , and  $Q_O = -1.32e$  in this work. These results compare well with the work of Mete *et al.* where they found  $Q_{Ti} = +2.66e$ , and  $Q_O = -1.33e$  [100]. Also charge values for different binding geometries are as shown Table 3.4. When the results of calculations for the bare surface with adsorption results

are compared, the highest change in the charge of Pr atom is in the Pr( $a-2$ ) configuration, which is found as  $Q_{\text{Pr}} = +1.96e$ . This large charge transfer correlates with the large binding energy. When considering the Pr( $a-1$ ) model, the highest change in the charge of Ti atom is seen easily. The poorest interaction between the titanium with Pr appears in the Pr( $a-3$ ) structure. In this model, the modest charge exchange between the atoms is an expected result because of Pr interaction with saturated Ti ( $\text{Ti}_{6c}$ ) atom.

The group of lanthanide elements show a strongly magnetic susceptibilities. Hence, Pr:TiO<sub>2</sub> structure gains magnetic property, after adsorption. The magnetic moments of all adsorption geometries considered here are listed in Table 3.3. In all cases, the magnetic moment takes on two different values 3 and 5  $\mu_B$ . Magnetization arises from interaction between Ti  $d$  and the Pr  $f$  orbitals. One Ti has remarkably large orbital magnetic moment of 1.6  $\mu_B$  for Pr( $a-1$ ), while each of the three Ti atoms bond with Pr has magnetic moment of 0.9  $\mu_B$  for Pr( $a-2$ ).

The optical absorbance spectra of the systems studied are as shown in Fig. 3.4. The spectrum was investigated in two parts the ultraviolet-visible (UV-vis,  $\lambda=100-800$  nm) and the near to far infrared (IR,  $\lambda=800-14000$  nm) for better resolution. A large peak in the UV range (between 150–400 nm), is seen for TiO<sub>2</sub>(101) shown in Fig. 3.4(a). TiO<sub>2</sub>(101) can only respond to ultraviolet-light (UV) and shows no absorption response in the visible-light region, which is consistent with the literature [101]. The performance of all three Pr-doped surfaces in the early UV range (100-200 nm) is better than the undoped surface while in the 200 and 400 nm, it is somewhat smaller. The visible part of the spectrum also displays an obvious gain in the absorption for all three doped structures over the bare surface (inset of Fig 3.4(a)). The geometry of Pr( $a-3$ ) that shows the best performance in the region after 500 nm is closely followed by Pr( $a-2$ ). Here, the electron transition from impurity states to the conduction band (CB) would lead to an obvious reduction of absorption energy and induce visible-light absorption. On the other hand, this result is slightly larger than experimental value [102]. In the near-IR region shown in Fig. 3.4(b), the bare surface exposes no absorption performance at all while Pr( $a-2$ ) and Pr( $a-3$ ) models remain active. In fact, Pr( $a-2$ ) shows a large peak at around 4000 nm. Conversely, Pr( $a-3$ )

quickly loses activity just beyond the near-IR edge.

### 3.2.3 Varying of $U$ parameter

In this section, two adsorption structures examined in the previous section have been taken as reference models and their behaviours were investigated for various  $U$  values. The effect of the  $U$  term on the structures were investigated by some studies, when Pr is replaced by Ti atoms in the  $\text{TiO}_2$  bulk [106, 107]. However, there is not evidence of any studies related to the adsorption process. As mentioned before, in this part of our study, we concentrate on Pr( $a-1$ ) and Pr( $a-2$ ) geometries. The  $U$  values for the Pr  $4f$  orbitals atom were first chosen in the 5–8 eV for adsorption process, while  $U = 5$  eV taken for the surface Ti atoms. The defect states located in the band gap indicate a few differences between different  $U$  values. They are nearly converted to flat structures depending on increase value of  $U$  for Pr. Then, we investigated the structures for values of  $U$  chosen in the 5–8 eV for Pr atoms adsorbed on a newly formed surface with  $U = 6, 4$  eV for Ti  $3d$  orbitals. Our results are summarized in Table 3.5.

With increasing the value of  $U$  for Pr atom, although both Pr( $a-1$ ) and Pr( $a-2$ ) models do not exhibit visible changes in their adsorption geometry, they show a declining trend in the adsorption energy. While this decrease is very large, for Pr( $a-2$ ), the energy drop between the Pr: $U=5$  eV and the Pr: $U=6$  eV states is found to be extremely high compared to others around 0.59 eV. In terms of the bond lengths in Pr: $U=5$  eV structure, Pr distance to the other atoms are less than the distance found for higher  $U$  values. For instance, the distance between Pr and O1 in the structure of Pr: $U=5$  eV is found as 2.19 Å, while the same distance in the Pr: $U=6$  eV structure is found as 2.29 Å. There is a 0.10 Å difference between them. On the other hand, it is found as 2.31 Å for Pr: $U=7$  eV and Pr: $U=8$  eV. The difference between Pr: $U=6$  eV and Pr: $U=7$  eV is 0.03 Å. For all cases, the magnetic moment takes on three different values 1, 3 and 5  $\mu_B$ . All structures are quite similar to the situation in the previous section in terms of magnetic moment, except in the case Pr: $U=7$  eV for Pr( $a-2$ ). Here, while magnetic moment of praseodymium atom is rather low, that for each of

Table3.5: Calculated parameters: adsorption energy and average bond lengths of Pr adsorbed on the surface in two different configuration. In Hubbard  $U$  value used in the different for the Pr 4f orbital and fixed as 5 eV for the Ti 3d orbital.

$U_{Pr}$	$E^{ads}$ (eV)	$\mu_B$	Atomic Distance (Å)					
			Ti-Ti	Ti-O1	Ti-O2	Pr-Ti	Pr-O1	Pr-O2
			Pr(a-1)					
pure			3.12	1.88	2.03			
6	3.01	2.99	2.94	2.34	2.22	2.81	2.25	
7	2.96	5.04	2.94	2.34	2.21	2.83	2.25	
8	2.87	5.00	2.96	2.29	2.19	2.85	2.23	
			Pr(a-2)					
6	5.36	5.03	3.11	2.11	2.10	3.30	2.29	2.56
7	5.32	1.00	3.09	1.92	2.04	3.38	2.31	2.61
8	5.25	4.96	3.10	2.11	2.10	3.30	2.31	2.57

the three Ti atoms was found as nearly  $0.9 \mu_B$ .

According to the electronic band structures of Pr(a-1) which are as shown in Figure 5.3 on the leftmost panel, there are two dispersionless impurity states which are in the middle of the gap. These states are positioned under the Fermi energy level located in the conduction band and they are completely filled. Pr is more dominant with a little mixing of Ti in these impurity bands. The occupied energy states are degenerate along the  $\overline{JK}$  direction for Pr:U = 6,7 while they are non degenerate along the same direction for Pr:U = 8. As for Pr(a-2) models for different  $U$  values, the electronic band structure is very different from Pr:U=5 eV. The band gap is populated with more impurity states and Fermi level resides in the middle of the band gap. However, for  $U$  of 6 eV and higher values for Pr atom, which are as shown in Figure 5.3 on the rightmost panel, there are two impurity states located in the middle of the gap as it is Pr(a-1). For Pr:U=7 eV, these occupied energy state are degenerate along the  $\overline{\Gamma J}$  and  $\overline{J'K}$  directions. In terms of PDOS, Pr is more dominant with a little mixing of Ti and O in these impurity bands.

The computational Bader charge analysis of these adsorption geometries are listed in the Table 3.6. The highest change in the charge of Pr:U=6 eV is as in the

Table3.6: Bader charge of Pr adsorbed on the surface in two different configuration. In Hubbard  $U$  value used in the different for the Pr 4f orbital and fixed as 5 eV for the Ti 3d orbital.

$U_{Pr}$	Bader Charges					
	Ti1	Ti3	O1	O2	O3	Pr
	Pr( $a-1$ )					
pure	+2.04	+2.04	-0.91	-1.08	-0.91	
6	+1.50		-1.11	-1.19		+1.48
7	+1.50		-1.11	-1.18		+1.47
8	+1.50		-1.11	-1.18		+1.42
	Pr( $a-2$ )					
6	+1.80	+1.80	-1.16	-1.24	-1.10	+1.60
7	+2.00	+1.82	-1.16	-1.21	-1.11	+1.53
8	+1.80	+1.80	-1.16	-1.24	-1.16	+1.51

Pr( $a-2$ ) configuration, which is found as  $Q_{Pr} = +1.60e$ . In same configuration, for larger  $U$  values for compared to Pr, there is a slight downward trend in these values. The difference in terms of charge transfer is less, when also considering the binding energies, we can assume that adsorption strength of Pr atom is not much has changed with the increase of the  $U$  value. In addition, the Bader charge values for the Ti atoms are much lower, and for O atoms a bit higher, their bare surface values. On the basis of these results, we can consider that the Pr–O interaction is stronger than Pr–Ti interaction, also compatible with our adsorption structures. Pr( $a-1$ ) structure that is less stable than Pr( $a-2$ ), as Pr atoms seem to have less of a charge difference for all  $U$  values. The charge values for the Ti atoms are higher compared with their bare surface values. Since the Pr–Ti interaction is more dominant in these cases, this result is expected.

While adsorptional geometries are represented in the Figure 4.1  $U = 6$  eV for Ti, and also related structural parameters and adsorption energies are listed in Table 3.7. With increasing  $U$  for the Pr atom, the results do not indicate any trends in terms of the adsorption energy. Especially, the energy of Pr( $a-1$ ) for Pr: $U=8$  eV state is found as extremely rather high value compared to other Pr( $a-1$ ) structures. In this case we observed a change in the adsorption structure becoming similar to the more stable structure such as Pr( $a-2$ ). In accordance



Table3.7: Adsorption energy (eV), magnetic moment ( $\mu_B$ ), and average bond lengths ( $\text{\AA}$ ) two Pr adsorption geometries on the  $\text{TiO}_2$   $U_{Pr}=5-8$  eV and  $U_{Ti}=6$  eV.

$U_{Pr}$	$E^{ads}$	$\mu$	Distances					
			Ti-Ti	Ti-O1	Ti-O2	Pr-Ti	Pr-O1	Pr-O2
Pr(a-1)								
pure			3.14	1.89	2.04			
5	3.42	5.00	3.00	2.31	2.28	2.82	2.24	2.70
6	2.52	1.00	2.97	2.40	2.28	2.84	2.22	2.66
7	2.43	4.99	2.96	2.35	2.25	2.84	2.20	2.84
8	4.81	5.00	3.09	2.22	2.25	3.29	2.28	2.56
Pr(a-2)								
5	7.68	5.00	3.10	2.09	2.15	3.24	2.12	2.41
6	7.75	5.04	3.17	2.07	2.20	3.25	2.20	2.37
7	7.33	5.00	3.09	1.95	2.01	3.45	2.31	2.80
8	6.92	1.00	3.12	2.08	2.15	3.26	2.14	2.41

with the geometry of the more stable adsorption the binding energy is higher relatively. Considering the bond lengths in Pr(a-1) for Pr:U = 8 structure, Pr distance to be Ti atom are more than the distance for the other Pr(a-1) for different value of  $U$  structures. For instance, the distance between Pr and Ti in the structure of Pr:U=5 eV is found as 2.82  $\text{\AA}$ , while the same distance in Pr:U=8 eV structure is found as 3.29  $\text{\AA}$ . This is consistent with the change of the adsorption geometry. When the Pr(a-2) results are investigated, the adsorption energy of Pr:U=6 eV is seen to have the highest value (7.75 eV). For all structures, the magnetic moment gets on three different values to be 1, 3 and 5  $\mu_B$ .

In relation to the electronic band structures and DOS of Pr(a-1) which are as displayed in Figure 4.1 on the leftmost panel, there are two impurity states which are located in the middle of the gap and they are also evident from the corresponding PDOS plots for all value of  $U$ . These states are positioned below the Fermi energy level located in the conduction band so that they are completely filled. Interaction between Pr and Ti atoms is more dominant in this impurity state. The occupied energy states are degenerate along the  $\overline{JK}$  direction for Pr:U=6. For Pr(a-2) models for varied  $U$  value, the electronic band structure is very different from Pr(a-1) models. The band gap is populated

Table 3.8: Bader charges ( $|e|$ ) of two Pr adsorption geometries on the  $\text{TiO}_2$   $U_{Pr}$ . In Hubbard  $U$  value used in the different for the Pr 4f orbital and fixed as 6 eV for the Ti 3d orbital. eV.

$U_{Pr}$	Charges					
	Ti1	Ti3	O1	O2	O3	Pr
	Pr( $a-1$ )					
pure	+2.06	+2.06	-0.93	-1.11	-0.93	
5	+1.50		-1.14	-1.19		+1.47
6	+1.45		-1.12	-1.19		+1.48
7	+1.50		-1.13	-1.20		+1.46
8	+1.57		-1.20	-1.15		+1.86
	Pr( $a-2$ )					
5	+1.84	+1.85	-1.21	-1.27	-1.16	+1.96
6	+1.84	+1.85	-1.17	-1.23	-1.16	+1.99
7	+1.85	+1.87	-1.18	-1.24	-1.16	+2.00
8	+1.84	+1.84	-1.21	-1.28	-1.17	+1.98

with impurity states under the Fermi level resided in the middle of the band gap. Two unoccupied states were located above of the Fermi level, except Pr:U = 7. The contribution of the Pr atom is more dominant in these unoccupied states, according to the PDOS graph. There are no empty states in the band gap for the Pr:U=7 eV structure. In addition, the conduction band minimum is at the K point.

The Bader charge analysis of these structures are given in Table 3.8. The highest change for the partial charge Pr is  $U$  value of 8 eV in the Pr( $a-1$ ) configuration, which is found as  $Q_{Pr} = +1.86e$ . Here, the bonding geometry of this structure changes and resembles Pr( $a-1$ ) models and therefore this relatively high charge transfer is to be expected. For the other  $U$  values for Pr( $a-1$ ), the changes for Pr charge are close to each other. Similar to  $U_{Ti}=5$  eV, the Bader charge values for the Ti atoms are much lower, for the O atoms are higher for Pr( $a-2$ ). However, Pr atoms seem to display a larger charge difference for all  $U$  values for  $U_{Ti}=5$  eV.

Adsorption geometries for  $U = 4$  eV are displayed in the Figure 3.7, and relevant

structural terms and adsorption energies are detailed in Table 3.9. In terms of the adsorption energy, any trend related to increasing  $U$  for the Pr atom are not appeared, similar to  $U = 6$  eV. Particularly, the energy of Pr(a-1) for Pr:U=6 eV state was found to be extremely high value compared to other Pr(a-1) structures such as 6.18 eV. Because adsorption geometry changed and has formed with similar to the most stable structure like Pr(a-2). The energy of Pr(a-2) for Pr:U=6 eV state was calculated to be 6.17 at a high level. The geometry of the all cases are accordance with adsorption energy, relatively. For instance, the distance between Pr and Ti the structure of Pr:U=7 eV is found as 3.34 Å, while the same distance in Pr:U=8 eV structure is found as 3.35 Å, for Pr(a-2). Their binding energy differences was found as 0.12 eV in a relatively small value. For all cases, the magnetic moment gets on three different values to be 1, 3 and 5  $\mu_B$ .

Table3.9: Adsorption energy (eV), magnetic moment ( $\mu_B$ ), and average bond lengths (Å) of two Pr adsorption geometries on the TiO<sub>2</sub> for  $U_{Pr}$ =5-8 eV and  $U_{Ti}$ =4 eV.

$U_{Pr}$	$E^{ads}$	$\mu$	Distances					
			Ti-Ti	Ti-O1	Ti-O2	Pr-Ti	Pr-O1	Pr-O2
Pr(a-1)								
pure			3.12	1.88	2.01			
5	2.67	4.99	2.86	2.26	2.13	2.81	2.24	2.53
6	6.18	5.00	3.02	2.07	2.00	3.23	2.20	2.35
7	1.88	3.00	3.02	2.07	2.08	2.81	2.16	–
8	2.77	5.00	3.01	2.17	2.13	2.78	2.29	–
Pr(a-2)								
5	5.98	5.00	3.09	2.05	2.15	3.22	2.14	2.39
6	6.17	5.00	3.12	1.93	2.04	3.25	2.21	2.33
7	4.51	1.00	3.08	1.96	2.01	3.34	2.32	2.59
8	4.63	5.00	3.08	1.90	2.04	3.35	2.31	2.57

In relation to the electronic band structures of Pr(a-1) which are displayed in Figure 3.7, there are several impurity states located under the Fermi level. The band structure includes many more impurity states, the Fermi level is approaching the valence band, while  $U_{Pr}$  increases. For Pr(a-2), the number of impurity states are the same as in Pr(a-1).

Table 3.10: Bader charges ( $|e|$ ) of two Pr adsorption geometries on the  $\text{TiO}_2$  for  $U_{Pr}=5-8$  eV and  $U_{Ti}=4$  eV.

$U_{Pr}$	Charges					
	Ti1	Ti3	O1	O2	O3	Pr
	Pr( $a-1$ )					
pure	+2.00	+2.00	-0.91	-1.08	-0.91	
5	+1.53		-1.11	-1.16		+1.46
6	+1.79		-1.15	-1.22		+1.99
7	+1.76		-1.19	-		+1.46
8	+1.74		-1.12	-		+1.49
	Pr( $a-2$ )					
5	+1.79	+1.78	-1.18	-1.24	-1.13	+1.96
6	+1.99	+1.79	-1.13	-1.23	-1.14	+1.99
7	+1.98	+1.79	-1.12	-1.20	-1.21	+1.53
8	+1.97	+1.78	-1.15	-1.22	-1.16	+1.53

The Bader charge analysis of the adsorption geometries are in Table 3.10. The highest change for Pr appears for the  $U=6$  eV in the Pr( $a-1$ ) configuration, which is found to be  $Q_{Pr} = +1.99e$ . Here, the bonding geometry of this structure resembles Pr( $a-1$ ), and its binding energy was found to be significantly higher. The results obtained for other  $U$  values are chosen to each other. The binding energies in these structures were found to be relatively low, so these results are consistent with each other. These two structures were bound on surface relatively weak.

Finally, It appears from our study that the important characteristics of Pr adsorption on the (101) anatase surface does not change appreciably with different Hubbard  $U$  values. In the remaining chapters of the thesis both  $U_{Ti}$  and  $U_{Pr}$  will be fixed at 5 eV.

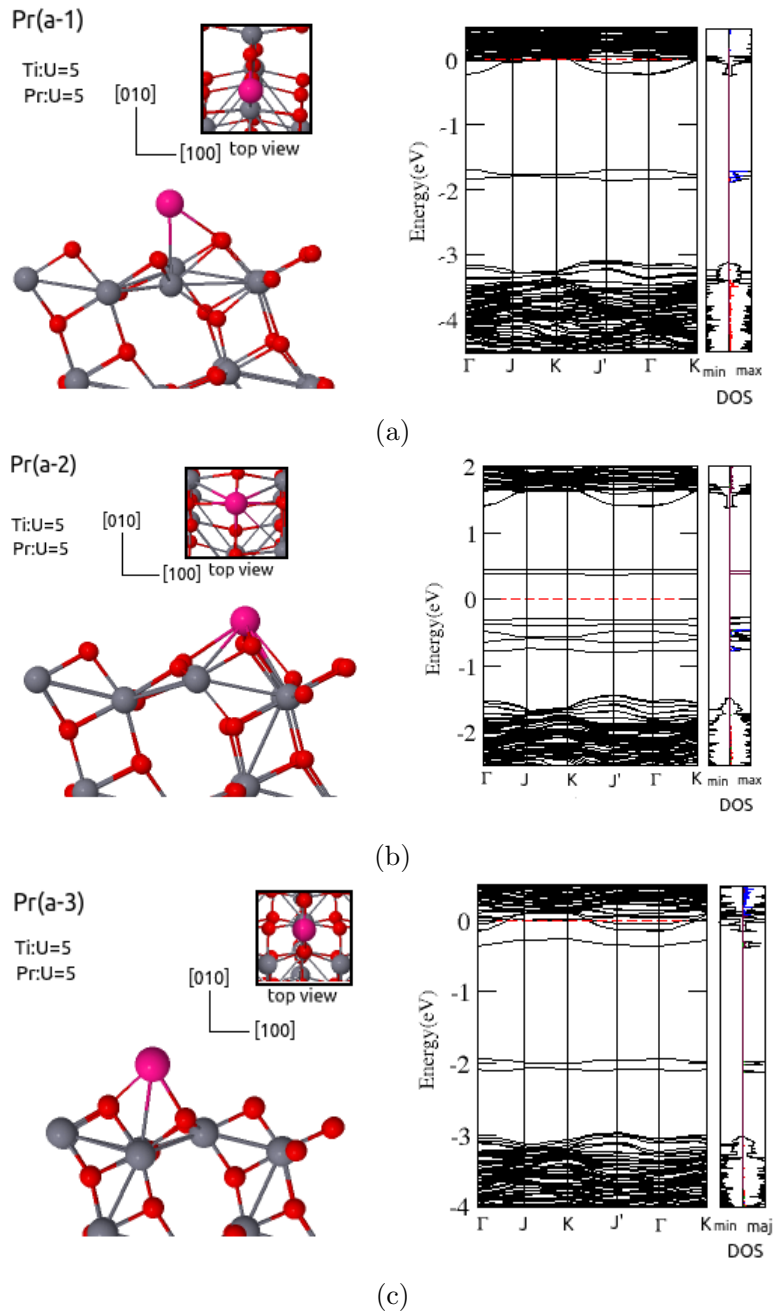


Figure 3.3: The geometric and electronic structures of three different adsorbed Pr:TiO<sub>2</sub> systems respectively for (a) Pr(a-1), (b) Pr(a-2), and (c) Pr(a-3) systems. Praseodymium, oxygen, and titanium atoms are indicated pink, red, and gray balls.

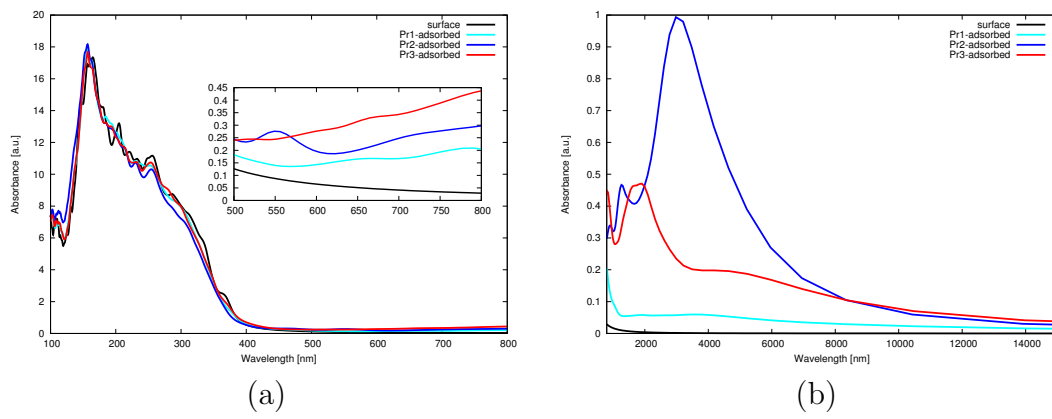


Figure 3.4: The optical absorption spectra of Pr adsorbed on TiO<sub>2</sub> models at (a) visible range and (b) infrared range.

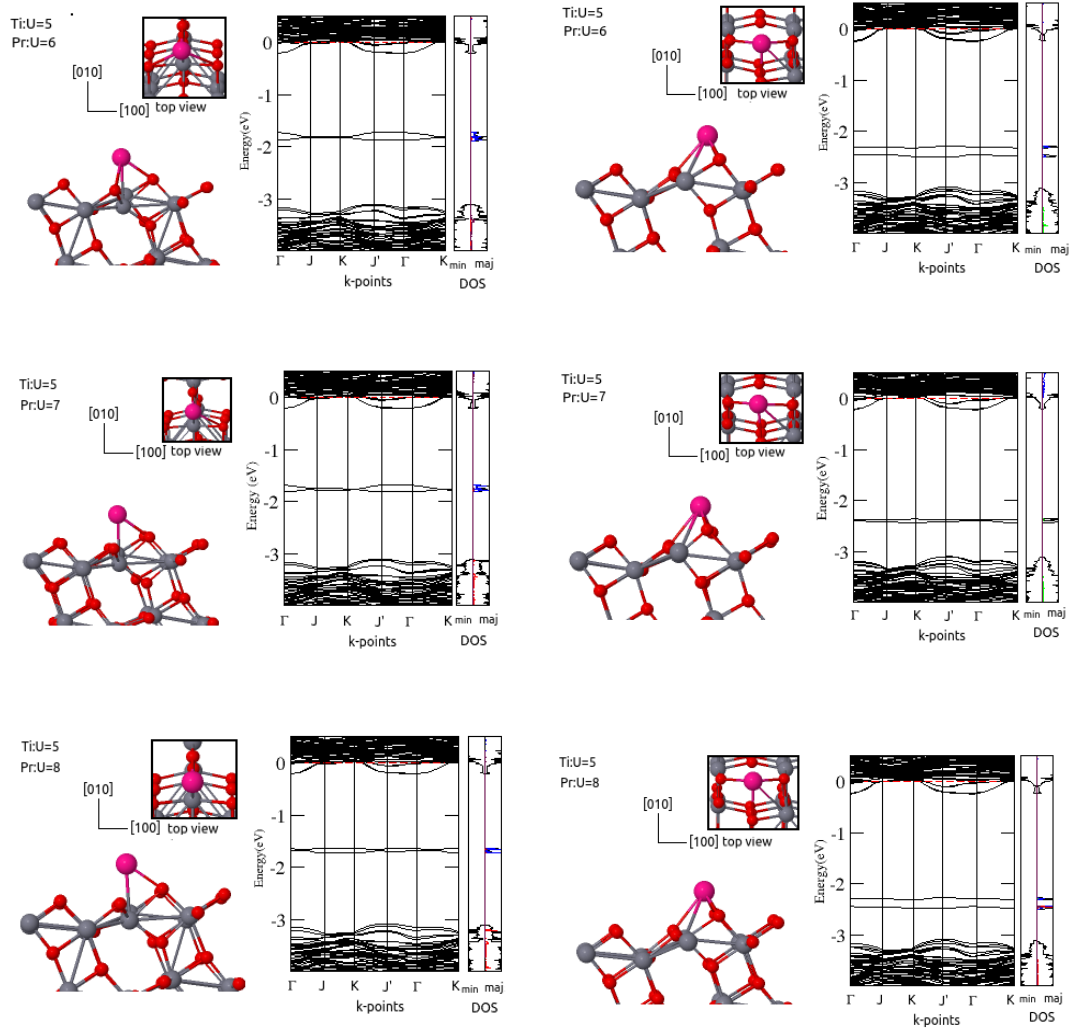


Figure 3.5: The geometric and electronic structures of two adsorptional cases for Pr:TiO<sub>2</sub> system, as the value of  $U$  for Ti was taken in 5 eV and for Pr was taken in the range of 5 to 8, respectively. While the first column represents the Pr( $a$ -1) case, the second column represents Pr( $a$ -2) case. Energy bands structures are represented rightmost panel of atomic structure figures

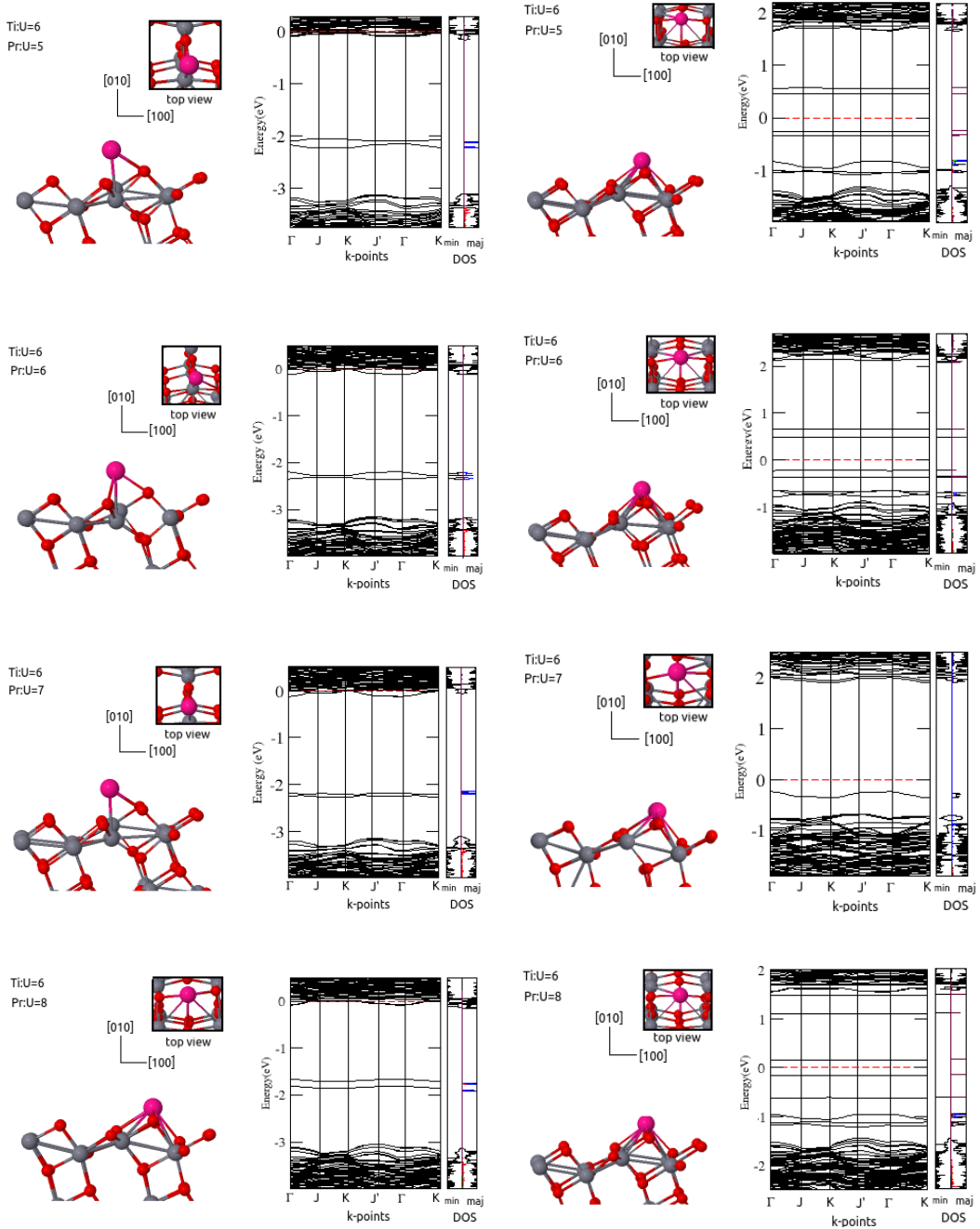


Figure 3.6: The geometric and electronic structures of two adsorptional cases for Pr:TiO<sub>2</sub> system, as the value of U for Ti was taken in 6 eV and for Pr was taken in the range of 5 to 8, respectively and it was taken to 6 eV for Ti. While the first column represents the Pr(*a*-1) case, the second column represents Pr(*a*-2) case. Energy bands and DOS structures are represented rightmost panel of atomic structure figures



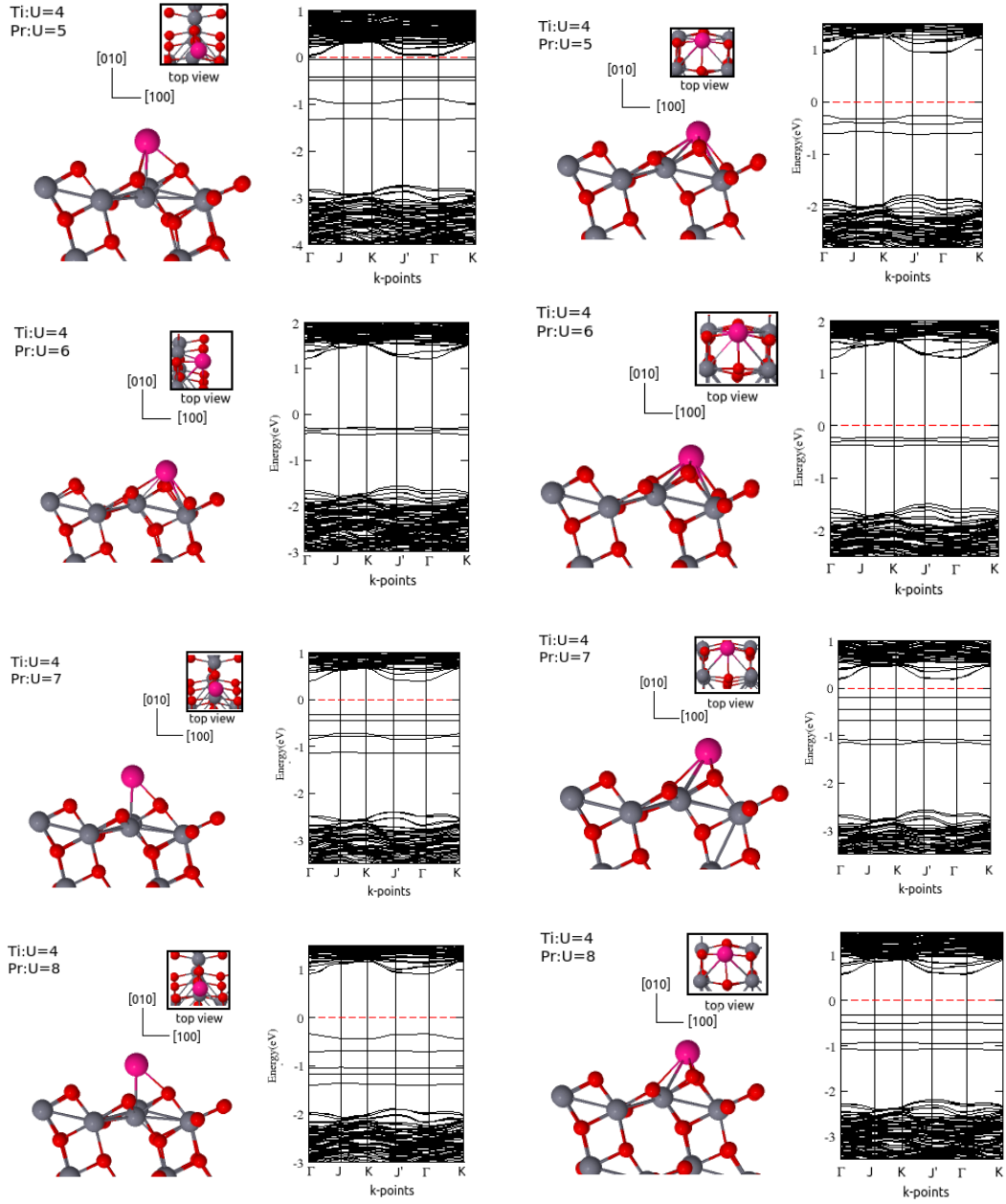


Figure 3.7: The geometric and electronic structures of two adsorptional cases for Pr:TiO<sub>2</sub> system, as the value of  $U$  for Ti was taken in 4 eV and for Pr was taken in the range of 6 to 8, respectively. While the first column represents the Pr( $a-1$ ) case, the second column represents Pr( $a-2$ ) case. Energy bands and DOS structures are represented rightmost panel of atomic structure figures



## CHAPTER 4

# BENZOIC ACID (BZA) ADSORPTION ON THE SURFACE

As many molecular adsorption applications in the field of photocatalytic activity of materials have commonly centered on the adsorption of anchoring groups (carboxylic acid, phosphonic acid, and hydroxyl groups). The most frequently used anchoring group is the carboxylic acid ( $-\text{COOH}$ ) [51, 52, 53]. It provides strong binding of the dye structures on the surface and encourages the charge transfer between the dye and the surface. Various stable binding configurations between surface and  $\text{COOH}$  are encountered in the literature [54, 55], while the configurations of  $\text{RCOOH}$  are not as available. There are very few examples focused on the adsorption of larger carboxylic acid molecules, such as benzoic acid, which possibly give more information about the carboxylic acid-surface interaction. Moreover, surface dopants such as Pr are known to provide anchoring sites for adsorbed molecules. It is therefore informative to investigate adsorption, electronic and structural properties of BZA molecules adsorbed on the bare and Pr-doped  $\text{TiO}_2$  (101) surfaces. In this chapter, we first present our results the gas-phase properties of the BZA molecules and later move on to adsorbed geometries.

### 4.0.4 Benzoic acid (BZA)

The geometric parameters of BZA such as bond lengths and angles as well as energy were calculated using DFT. The structures were compared with experi-

Table 4.1: Average bond lengths of of benzoic acid experimental and calculated by DFT

Bonds between atoms	Distances(Å)		
	Exp. [103]	Theo. [105]	Our Work
C1-C2	1.48		1.49
C2-C3	1.39	1.39	1.40
C3-C4	1.41	1.40	1.40
C4-C5	1.37	1.40	1.40
C5-C6	1.36	1.39	1.40
C6-C7	1.42	1.39	1.39
C7-C2	1.39		1.40
O1-C1	1.29	1.32	1.37
O2=C2	1.24	1.23	1.22
O1-H		1.00	1.09

mental and another theoretical work (DFT/B3LYP) [103, 105]. The calculated values for benzoic acid are listed in Table 4.1 in accordance with the atom numbering scheme shown in Fig 4.1-(a). Our calculation results indicate that almost all C–C bond lengths of the benzene ring have similar lengths, average of 1.40 Å. Distance between atoms C1–O1 in the carboxyl group is longer than C1=O2. Taking into account the experimental data the difference between the two bonds is 0.08 Å for C1–O1 and 0.02 Å for C1=O2. In the experiment, the O2=C1–O1, C2–C1–O1, and C2–C1=O2 angles were found as 122°, 118°, and 122°, respectively. In our study, these values were found as 122°, 113°, and 125°, respectively. Also, the angle value of C–O–H was found as 105°.

Highest occupied molecular orbital (HOMO) and lowest unoccupied molecular orbital (LUMO) of BZA are very useful quantitative descriptions of bonding. These orbitals determine the reactivity of the molecules and the process of interaction with others. The energy difference between the HOMO and LUMO is referred to as the HOMO–LUMO gap. It is used to explain the possible charge transfer within the molecule when interacting with other species. For the benzoic acid molecule, the HOMO and LUMO gap is 4.00 eV, as shown in Fig 4.1-(b). A small HOMO–LUMO gap indicates low stability for the molecule, which means higher reactivity in chemical reactions.

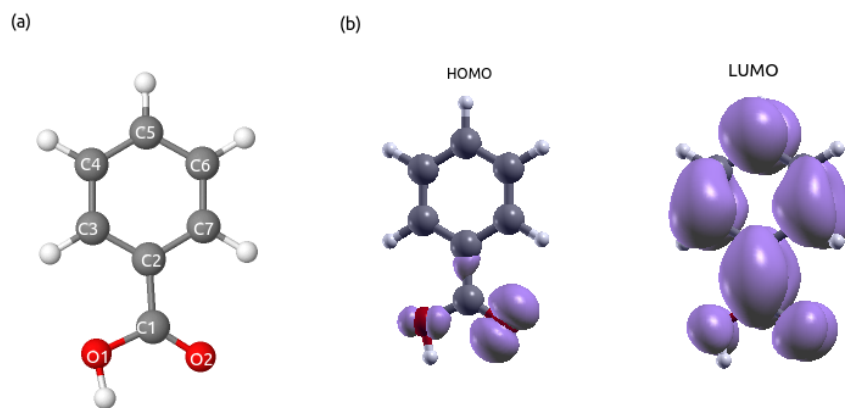


Figure 4.1: (a) The relaxed benzoic acid with atomic labels, (b) HOMO and LUMO charge densities

#### 4.0.5 Benzoic acid adsorbed on Bare Surface

After the absorption process, three stable configurations were identified for the BZA molecule interaction with the  $\text{TiO}_2$  anatase (101) surface, as shown in Figure 4.2. In two of these configurations, the molecule is upright forming one Ti–O covalent bond, ( $C_b(a-1)$  and  $C_b(a-2)$ ). In the third BZA interacts with the surface atoms in the horizontal position,  $C_b(a-3)$ . The adsorption energies of BZA and relevant structural parameters are listed in Table 4.2, and also atomic band structures and density of states are indicated in the rightmost panel of Figure 4.2.

The highest adsorption energy has been found as 0.88 eV for the  $C_b(a-1)$  geometry. This value is consistent with the adsorption energy values in the range of 0.8 eV to 1.0 eV found by Martsinovich *et al.* [54] and also the value of 0.92 eV found by Vittadini *et al.* [55] for the COOH acid. The bond length of Ti–O2 is 1.87 Å O2–C1–O1 and C1–O1–H angles are  $124^\circ$  and  $110^\circ$ , respectively. It is observed that small changes of angular values were calculated as compared to the gas phase of the BZA molecule. Also, the angle between the molecular plane and the surface (C1–O1–Ti) was found to be  $90^\circ$ . For  $C_b(a-2)$ , BZA adsorbed on the surface has binding energy of 0.83 eV. The average Ti–O2 distance is 1.88 Å. The angle values of O2–C1–O1 and C1–O1–H are  $122^\circ$  and  $104^\circ$ , respectively, while C1–O1–Ti is  $82^\circ$ . These results are closer to the values of the gas phase

Table 4.2: Average bond lengths ( $\text{\AA}$ ) and adsorption energies (eV) of BZA and BZ adsorbed on  $\text{TiO}_2$  and  $\text{Pr}/\text{TiO}_2$ .

	$E^{ads}$	Atomic Distance					
		Ti-Ti	Ti-O <sub>s1</sub>	Ti-O <sub>s2</sub>	Ti-O1 <sub>m</sub>	Ti-O2 <sub>m</sub>	C-O <sub>m</sub>
$C_b(a-1)$	0.88	3.13	1.87	2.02	2.42		1.25
$C_b(a-2)$	0.83	3.17	1.88	2.08	2.34		1.26
$C_b(a-3)$	0.13	3.11	1.88	2.02	3.19		1.23
$C_b(d-1)$	2.43	3.15	1.88		2.14	2.24	1.29
$C_b(d-2)$	1.76	3.21	1.87		2.24	2.25	1.29

		Ti-O <sub>s1</sub>	Ti-O <sub>s2</sub>	Pr-Ti	Pr-O <sub>s1</sub>	Pr-O <sub>s2</sub>	Pr-O1 <sub>m</sub>	C-O <sub>m</sub>
C(a-1)	1.02	2.10	2.07	3.45	2.20	2.84	2.36	1.25
C(a-2)	0.94	2.14	2.11	3.24	2.26	2.42	2.42	1.25
C(a-3)	0.76	2.10	2.11	3.24	2.23	2.44	2.50	1.26
C(d-1)	3.87	1.95		3.26	2.23	2.49	2.32	1.31
C(d-2)	2.54	2.08		3.28	2.17	2.69	2.31	1.34

of molecule as compared to  $C_b(a-1)$ . Here, we conclude that the molecule is influenced less by the interaction with the surface in terms of atomic structure. For  $C_b(a-3)$ , bonding is achieved via weak forces and a covalent bond is absent. Accordingly, the binding energy is only 0.13 eV. For this configuration, an inclination is observed towards the surface which results from interaction between oxygen atoms on the surface and carbon atoms in the molecule.

Regarding the electronic properties, first, we compared the band gaps of anatase bare and adsorption of BZA surfaces, gain insight on the effect of adsorption on the electronic structure of the anatase. The values of band gaps of both adsorption models are very similar to those of the bare surface, as shown in the rightmost panel of Figure 4.2. The band gaps are reduced by only about 0.1 eV upon adsorption (Table 4.3). This suggests little effect of adsorption on the electronic structure of anatase slabs. Energy levels originating from the BZA molecule are not located in the gap. There are two energy states near the valence band edge. On the other hand, for the  $C_b(a-3)$  geometry, impurity states originating from the molecular interaction can be seen clearly located close

to the valance band region. As a result of these states a band gap narrowing in the range of about 0.6 eV can be observed. The DOS for the surface with adsorbate is very similar to that of the bare surface. For all BZA binding on the bare surface forms, there are only small changes due to the presence of the adsorption.

#### 4.0.6 Benzoic Acid Adsorbed on Pr/TiO<sub>2</sub> Surface

In this part, BZA was adsorbed on the surface on which a Pr impurity atom was already incorporated. Since the Pr(a-2) geometry is the most stable one, it was used as the base for our BZA adsorption studies. Three different structures were considered for BZA adsorption: two vertical positions of BZA on Pr, C(a-1) and C(a-2); one horizontal position on Pr, C(a-3). The adsorption energies and relevant structural values of BZA in for these configurations were listed in table 4.2 and band structures and density of states are indicated in Figure 4.2. Here,  $U$  values were taken to be 5 eV both for Ti and Pr atoms. All the relevant atomic and electronic properties were discussed in the previous chapter.

The highest adsorption energy for BZA was found as 1.02 eV in the C(a-1) case. The formation energy was calculated to be 7.06 eV. The total adsorption energies of Pr(a-1) and C(a-1) were found 7.06 eV. These results are same. For the most stable position, atomic distances of Ti-O2 is found 2.07 Å, also the angles of O2-C1-O1 and C1-O1-H are found to be 122° and 112°, respectively. These values are very similar to gas phase of the BZA molecule. The angle between the molecules and the surface atom (C1-O1-Ti) was found to be 91°. For C(a-2), which is the other vertical adsorption configuration of BZA on Pr, the adsorption energy is calculated as 0.94 eV. The length of the Ti-O2 bond is found as 2.11 Å, slightly longer than the value for the of C(a-1) model. The O2-C1-O1 and C1-O1-H angles are found to be 123° and 115°, respectively. In the C(a-3) structure, which is the horizontal geometry. The adsorption energy is found to be 0.76 eV. The length of Ti-O2 is 2.11 Å. It is similar to C(a-2) structure, slightly longer than that of C(a-1) model. The angles of O2-C1-O1 and C1-O1-H are found to be 121° and 108°, respectively. As seen to in the previous section,

the molecule horizontally adsorbed on the surface the adsorption structures of surface without Pr atom. It is seen here that the ability of molecule adsorption of the surface can be increased by Pr impurity of the surface.

We compared the band structures of the anatase surface with a Pr atom (Figure 4.2) and adsorption of BZA on Pr-doped surface, to detect the effect of adsorption on the electronic structure of the anatase. The number of states originating from Pr impurity atom located in the band gap decreased after benzoic acid adsorbed on the surface. The band gap is found to be 1.1 eV and this value is same for three combinations. This value is appropriate for absorption in the visible range. In terms of PDOS graph, while between Ti, O and Pr interaction is more dominant in the defect states locating under the Fermi level. Pr is more active in unoccupied states at structure of Pr(a-2). Pr and BZA interaction is more predominant in this case.

#### 4.0.7 Dissociated Benzoic Acid on Surface

In this subsection, the benzoate anion (BZ) adsorbed on the anatase (101) surface has been investigated. Two different stable geometries with were found; both are shown in Figure 4.3 and relevant structural values sre listed table 4.2. In structure  $C_b(d-1)$ , two O molecule atoms bond with unsaturated Ti5c surface atoms. The Ti-O1 and Ti-O2 bond lengths are 2.14 Å and 2.24 Å, respectively. The O2-C1-O1 angle was found to be 125°. This value has increased as compared with its gas phase value. In the geometry labeled  $C_b(d-2)$ , two O molecule atoms tend to bond with an unsaturated Ti5c surface atom. The Ti-O1 and Ti-O2 distances are calculated to be 2.24 Å and 2.25 Å, respectively. The O2-C1-O1 angle was found to be 116°, which is once again smaller than the gas phase. The O2-Ti-O1 angle was found to 58°. When these structures are compared to their adsorption energies, we can say that the  $C_b(d-1)$  structure to be more stable with its 2.43 eV value.

As seen in the band structure plots, defect states originating from molecule and surface interaction are located near the VB for both geometries. This defect states appear flat and they corresponds to the  $p$  orbitals. This indicates a larger



effect of oxygen on these cases. The values of band gaps for both adsorption models are very similar to those of the bare surface. Band gap narrow were very small in the range of about 0.2 eV for  $C_b(d-1)$  and 0.12 eV for  $C_b(d-2)$ . Both CBs appear more crowded in terms of gap states compared to the band structures of BZ geometries.

#### 4.0.8 Dissociated Benzoic Acid on the Pr/TiO<sub>2</sub> Surface

In this part, we have investigated the benzoate anion (BZ) adsorbed on the surface with a Pr impurity atom. Two different combinations were found. In the first, two O molecule atoms bond with unsaturated Pr surface, (C(d-1)). In the second only one O atom is bound to Pr, (C(d-2)). Both of them are shown in Figure 4.3 and relevant structural values were listed table 4.2. In the C(d-1) structure, the Pr-O1 and Pr-O2 bond lengths are found to be 2.32 Å and 2.69 Å, respectively. The value of Pr-O1 is shorter than nondissociated BZA. The O2-C1-O1 angle was found to be 120°. This value has decreased as compared with the gas phase. The O2-Pr-O1 angle was found to 52°. In the C(d-2) structure, Pr-O1 bond length is calculated as 2.31 Å. This value is very close to its value of C(d-1). The O2-C1-O1 angle was found to be 123°, a value that is greter than the gas phase. When the adsorption energies of these structures are compared, the C(d-1) structure to be more stable with its 3.87 eV. As a result, it can be said that the molecule is able to bind more strongly to the surface owing to the presence of Pr impurity atom.

The electronic properties of these forms have been examined from spin-polarized band structure and density of states graphs and are shown in the rightmost panel of atomic structure in Figure 4.3. As displayed in the band structures of C(d-1), two fully occupied impurity states are located below the Fermi energy and in the band gap while the other states reside very close to the valence band. The number of these states in the C(d-1) is less than C(d-2). According to the PDOS graph, Ti, O and Pr contributions dominate in the energy states originating from molecule-surface interaction. As for the band structure of C(d-2), in contrast to the C(d-1) structure, the number of impurity states within the band gap appears

to be larger. Once again, Ti, O and Pr contributions dominate although the Pr contribution is smaller. The band gap of both of band structures is found to be 1.4 eV. This value corresponds to the visible range.

Table 4.3: Bader charge values of BZA and BZ adsorbed on TiO<sub>2</sub> and Pr:TiO<sub>2</sub>.

	$E_g$	Bader Charges									
		Ti	O1	O2	Pr	O1 <sub>m</sub>	O2 <sub>m</sub>	O(-H)	C <sub>a</sub>	C <sub>b</sub>	H
BZA						-1.12	-1.09		+1.39	-0.02	+0.59
BZ						-0.82	-0.83		+1.42	-0.05	
C <sub>b</sub> (a-1)	2.80	+2.09	-0.91	-1.07		-1.16	-1.39		+1.37	+0.15	+0.16
C <sub>b</sub> (a-2)	2.84	+2.09	-0.91	-1.12		-1.13	-1.19		+1.51	-0.11	+0.30
C(a-1)	1.14	+1.81	-1.14	-1.28	+2.09	-1.18	-1.24	-1.00	+1.43	-0.01	+0.07
C(a-2)	1.13	+1.69	-1.14	-1.31	+2.09	-1.17	-0.77	-1.04	+1.40	+0.06	+0.75
C(a-3)	1.19	+1.80	-1.15	-1.26	+2.01	-1.17	-1.15		+1.44	-0.13	+0.33
C <sub>b</sub> (d-1)	2.70	+2.09	-0.91	-1.00		-1.09	-1.12	-1.25	+1.43	+0.03	+0.30
C <sub>b</sub> (d-2)	2.77	+2.08	-0.90	-1.03		-1.07	-1.10	-1.19	+1.46	+0.06	+0.34
C(d-1)	1.86	+2.02	-1.09	-1.21	+2.07	-1.17	-1.16	-1.31	+1.45	+0.03	+0.26
C(d-2)	1.74	+1.81	-1.12	-1.23	+2.10	-1.20	-1.14	-1.25	+1.49	+0.03	+0.30

The Bader charges of C, O<sub>m</sub> and H atoms in the benzoic acid molecule, Ti and O surface atoms and Pr based are listed in Table 4.3. BZA is adsorbed more strongly on the Pr/TiO<sub>2</sub> as seen from the high charge values of O<sub>m</sub>, compared to the bare surface. Here, more charge transfer is realized in these structures. In the geometries, the charge transfer is realized between the O2<sub>m</sub> and the H atom, not the surface atoms. The highest change in the charge of O2<sub>m</sub> atoms is observed in the C(d-1) configuration. This result is consistent with the results of adsorption energy results.

#### 4.0.9 Optical Properties

The absorption spectrum of the pure and decorated TiO<sub>2</sub> surfaces are calculated and shown in Fig. 4.4 4.5 4.6. When BZA is adsorbed on the surface, absorption response is obtained in the UV-region. It is known that benzoic acid can show absorption performance in the UV-region, which is similar to the TiO<sub>2</sub>, so these results do not surprise for us. (fig. 4.4(a)). However absorption is seen around

only 400 nm in the visible-range for  $C_b(a-3)$  model. This is thought to be related to impurity states located near the valence band. At Fig. 4.4(b), in a similar manner, dissolved benzoic acid adsorbed on surface models show an absorption behavior near 400 nm. The band gaps of these models have impurity states located very closed to the valence band, as well.

After BZA has been adsorbed on the surface with a Pr impurity atom, the adsorption profile is seen to be similar to Pr/TiO<sub>2</sub>, as shown in Fig. 4.5. As mentioned in the previous section, Pr adsorbed shifts the absorption band edge of the TiO<sub>2</sub> to 465 nm and 552 nm, as shown with red line in the figures. For the Pr adsorption system, it has exhibited the better optical absorption behavior in the visible-light region. Because Pr/TiO<sub>2</sub> has an impurity state originating from Pr in the band gap, it leads to a higher optical absorption performance than pure anatase TiO<sub>2</sub> in the long wavelength range. The enhanced absorption of the BZA added on Pr/TiO<sub>2</sub> surface in the whole visible region can be attributed to the presence of Pr atom. When the C(a-1) structure is considered, its absorption performance around the 500 nm is seen to decline below the performance of the Pr(a-2) structure. In the 630-780 nm range, C(a-2) shows the greatest performance. All structures display same the absorption behaviour at the 780 nm. Fig. 4.5(b) shows the absorption spectra of BZA adsorbed on Pr/TiO<sub>2</sub> at the infrared range. BZA adsorbed on the bare surface shows no absorption in the IR-region, so we consider only Pr adsorption TiO<sub>2</sub> systems. TiO<sub>2</sub> surface having Pr impurity atom can indicate absorption feature in the IR-region. Absorption performance of BZA added structures was found higher than Pr(a-2) in the infrared region.

The absorption spectrum of the two combinations of benzoate anion adsorbed on Pr/TiO<sub>2</sub> can be seen in Fig. 4.6(a). When these two structures are compared in the visible-light region, the most significant differences in the absorption spectrum is the fact that the absorption performance of C(d-2) is better than the C(d-1), even if it is at the same level with the performance of the structure Pr(a-2) between 700 nm–800 nm. While C(d-2) shows the same behavior with BZA applications in this interval, C(d-1) is different. Unlike BZA, absorption performance of benzoate anion adsorbed surface was found lower than Pr(a-2) in

the infrared region, as shown in Fig. 4.6(b). All combinations show a large peak at around 2000 nm, comparable to the absorbance performance in the visible range. Beyond this point, the absorbance performance decreases rapidly.

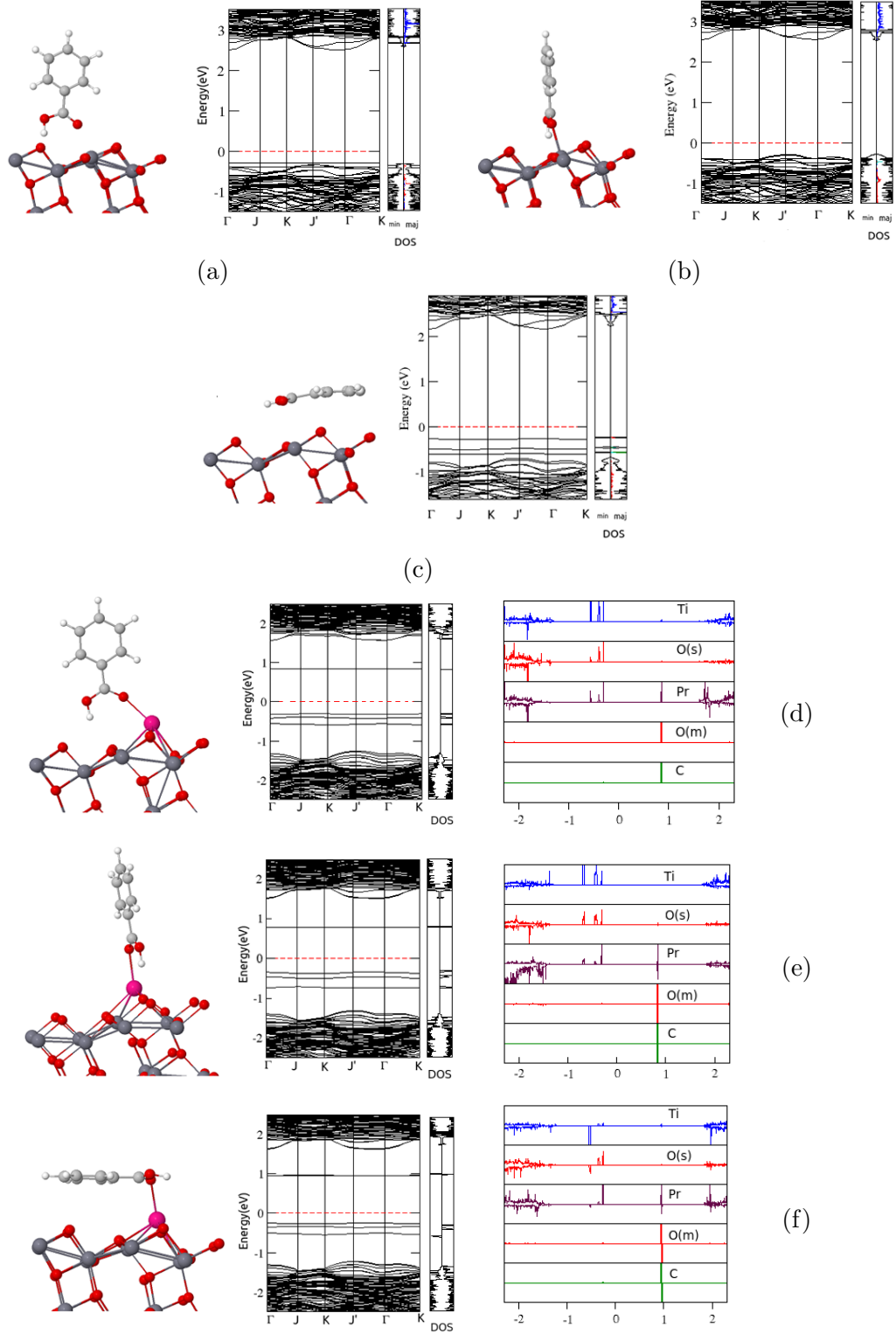


Figure 4.2: The geometric and electronic structures of adsorption of BZA on the bare surface ( $C_b(a-1)$ ;(a),  $C_b(a-2)$ ;(b),  $C_b(a-3)$ ;(c)) and on Pr/TiO<sub>2</sub> ( $C(a-1)$ ;(d),  $C(a-2)$ ;(e),  $C(a-3)$ (f))surface, respectively. Energy bands and PDOS structures are represented rightmost panel of atomic structure figures

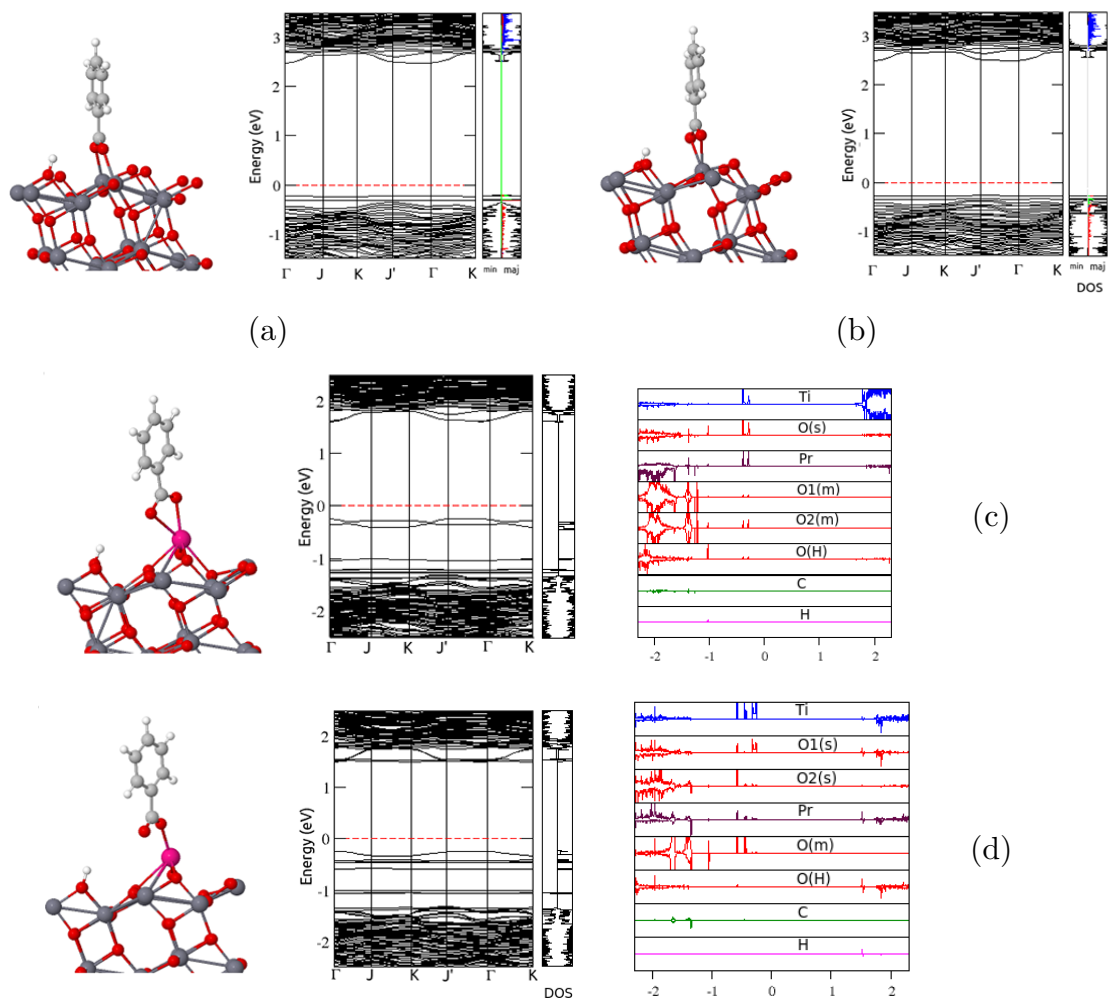


Figure 4.3: The geometric and electronic structures of adsorption of dissociated benzoic acid on the bare surface and on Pr:TiO<sub>2</sub> surface

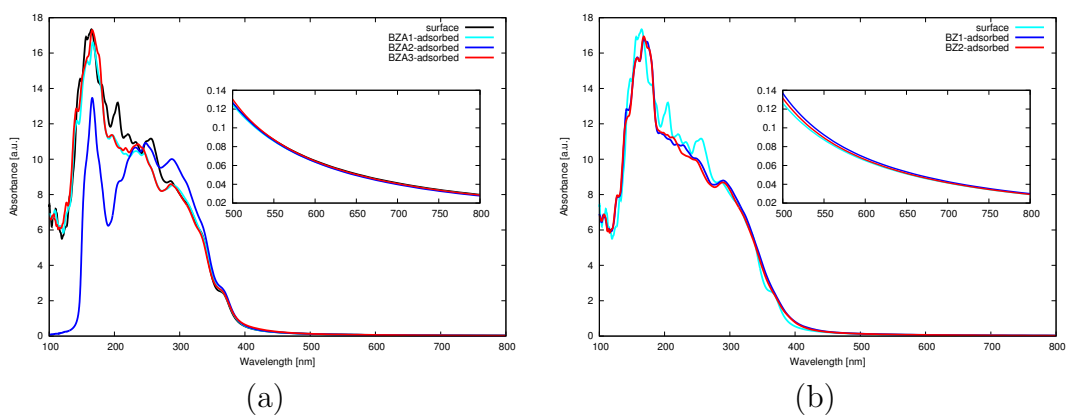


Figure 4.4: The optical absorption spectra of (a) benzoic acid (BZA) and (b) benzoate anion (BZ) adsorbed on TiO<sub>2</sub> models at visible range.

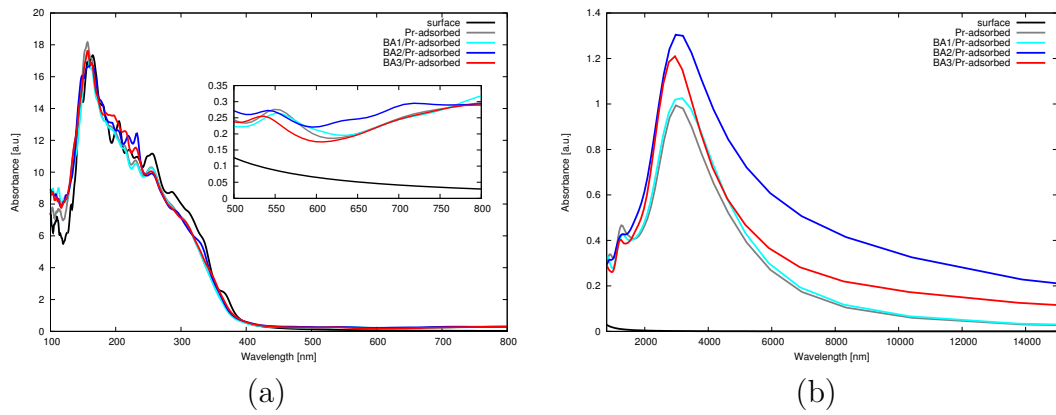


Figure 4.5: The optical absorption spectra of benzoic acid (BZA) adsorbed on Pr/TiO<sub>2</sub> models at (a) visible range, (b) infrared range.

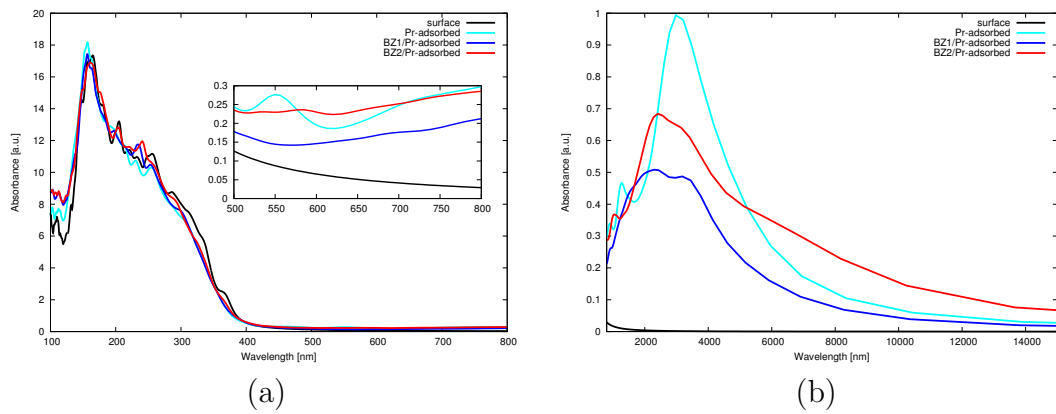


Figure 4.6: The optical absorption spectra of benzoate anion (BZ) adsorbed on Pr/TiO<sub>2</sub> models at (a) visible range, (b) infrared range.





## CHAPTER 5

# COUMARIN 153 (C153) ADSORPTION ON THE TiO<sub>2</sub> SURFACE

### 5.1 Computational Method

In this chapter, first principle total energy calculations were performed within DFT+U as in the our previous chapters. The valance atomic configurations used for the PAW potentials are  $3d^3 4s^1$  for Ti and  $2s^2 2p^4$  for O,  $5s^2 5p^6 4f^2 5d^1 6s^2$  for Pr,  $2s^2 2p^2$  for C,  $2s^2 2p^3$  for N,  $2s^2 2p^5$  for F and  $1s^1 2p^2$  for H, respectively. The cut off energy was 500 eV. The Hubbard  $U$  correction was used for Ti  $3d$  and Pr  $4f$  states. A  $U$  value of 5 eV was used for both atomic species. A  $4 \times 4 \times 1$   $k$ -point mesh was considered sufficient for our TiO<sub>2</sub> (101) surface calculations. A two-layer slab model was used to describe the (101) surface, as shown Fig. 5.2.  $3 \times 1$  unit in the surface plane was comprised of  $11.74 \times 10.36 \times 28.95 \text{ \AA}^3$  dimensions with a vacuum space of nearly 20  $\text{\AA}$ .

### 5.2 Result and Discussions

#### 5.2.1 Coumarin 153

Before the interaction of C153 with the TiO<sub>2</sub> anatase surface, we first present benchmark results for the C153 molecule in the gas phase. The geometric parameters such as bond lengths and angles as well as energy were calculated using DFT. The highest occupied (HOMO) and lowest unoccupied (LUMO) molecu-

lar orbitals are shown in Figure 5.1. The HOMO–LUMO gap is equal to 2.17 eV and compares reasonably well to the experimental value (2.94 eV) [108]. As seen in Figure 5.1, HOMO is localized in the carbonyl group of the C153 but extends also over the whole molecule. However, LUMO is more localized near the carbonyl group. When the atomic distances were compared with another theoretical work (TDDFT/B3LYP) [109], only differences were found. The bond length for C1=O1 in isolated C153 is 1.22 Å in our study (1.20 Å in the reference study). The lengths of the C1–C2, C1–O2, and C2–H bonds were calculated to be 1.44 (1.45) Å, 1.41 (1.39) Å, and 1.09 (1.08) Å, respectively. Figures shown in parentheses are taken from the results of the reference study [109].

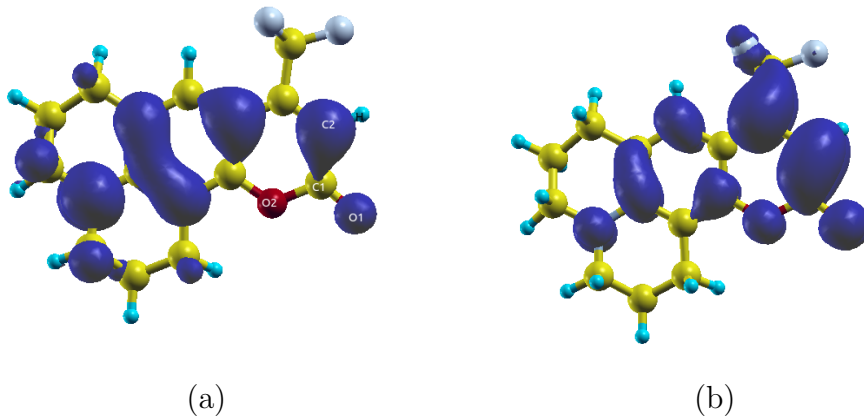


Figure 5.1: HOMO-LUMO of isolated Coumarin 153 is represented

### 5.2.2 TiO<sub>2</sub> Anatase Surface

The anatase surface considered in this study, as shown in Fig 5.2(a). It has six two-fold coordinated oxygen atoms ( $O_{2c}$ ) on step-like while three 6-fold coordinated Ti atoms are located along troughs ( $Ti_{6c}$ ). The terraces lying between the hills and the troughs expose six 5-fold coordinated Ti atoms ( $Ti_{5c}$ ) and three 3-fold coordinated O atoms ( $O_{3c}$ ). The band structure of the surface was calculated DFT+U framework with  $U = 5$  and an indirect band gap of 3.16 eV.

An O-vacancy ( $V_0$ ) was created on the surface by removing one oxygen, as shown in Fig 5.2(b) and (c). O-vacancy is one of the major point defect on anatase (101) surface and impacts the physical and chemical properties of metal oxide

surfaces significantly [110, 111]. Two excess electrons have appeared in the band gap because of oxygen reduction from the surface. The removal of a surface 2-fold  $O_{2c}$  results in leaves behind one 5-fold coordinated along the trough  $Ti_{5c}$  and one 4-fold  $Ti_{4c}$  along the terrace between the hills ( $V_{01}$ ). Removal of a terrace-like oxygen instead yielded, one 5-fold coordinated along the trough  $Ti_{5c}$  cations and two 4-fold  $Ti_{4c}$  occurred along the terrace ( $V_{02}$ ). The oxygen atom available at the tip of the molecule was placed on these defect sites.

O-vacancy formation energies ( $E_{form}$ ) were calculated using from following the equation [112]

$$E_{form}(V_0) = E_{tot}(def) - E_{tot}(nodef) + \frac{1}{2}\mu(O_2) \quad (5.1)$$

where  $\mu(O_2)$  is the total energy of an  $O_2$  molecule, and  $E_{tot}(def)$  and  $E_{tot}(nodef)$  are the total energies of the  $TiO_2$  surface with and without defects, respectively. The resulting formation energies for the first surface ( $V_{01}$ ), and the second surface ( $V_{02}$ ) sites are 3.93 eV, and 5.41 eV, respectively. Selloni *et al.* reported the structural properties of oxygen vacancies in anatase  $TiO_2$  (101) surface calculated using a DFT+ $U$  approach. Their results indicate that the formation energies of ( $V_{01}$ ) were found to be 4.15 eV for a slab containing 108 atoms and 4.25 eV for a slab containing 216 atoms. The energy of  $V_{02}$  was found to be 5.40 eV for the 216 atoms slab. These results point towards the sensitivity of the formation energies to the system size. The formation of energy for our system having 72 atoms cannot be compared to these results. On the other hand, the calculated energy of ( $V_{02}$ ) in our study is the consistent with Selloni's study. These results show that terrace-vacancy is more energetic than step-oxygen vacancy site

It need to give information about these electronic structures to explain localized band gap states. After O-vacancy process, free electrons in the defective geometry are taken instead of the ( $V_0$ ) vacancy states in the crystal lattice. These electrons have a direct effect on the electronic structure of  $TiO_2$  by forming defect states below the conduction band, as shown in Fig 5.2(b) and (c). As seen in the  $TiO_2(V_{01})$  band structure, while two occupied defect states appear

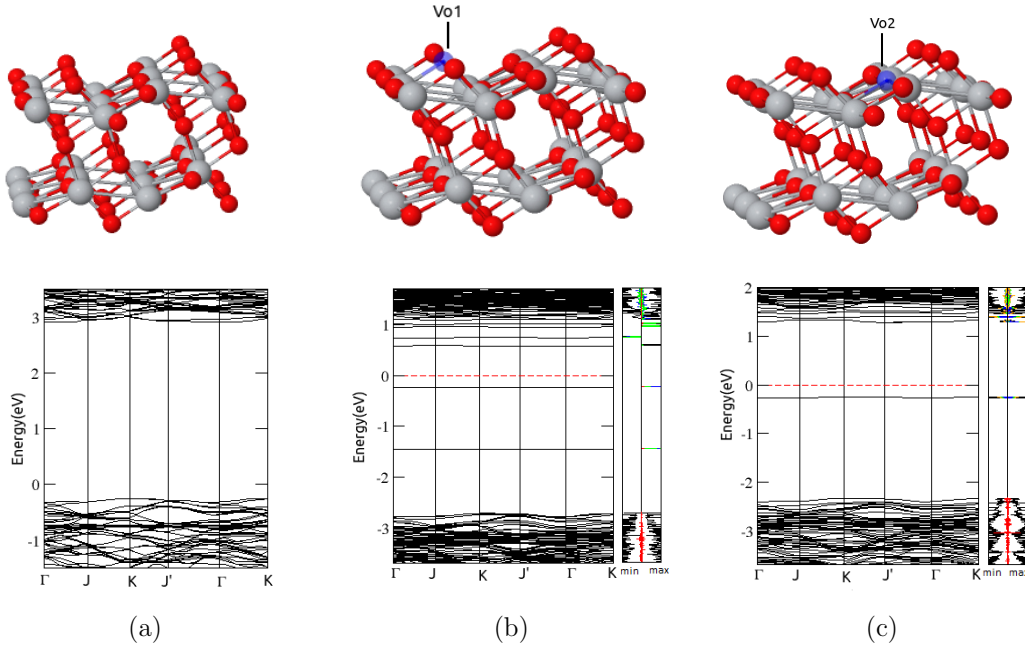


Figure 5.2: The atomic and electronic structures of (a)  $\text{TiO}_2$ , (b)  $\text{TiO}_2(\text{V}_{01})$ , and (c)  $\text{TiO}_2(\text{V}_{02})$  surfaces. PDOS graphics is shown rightmost panel by band structure, therein,  $\text{Ti}_{4c}$ ,  $\text{Ti}_{5c}$  and O are represented by the blue, green (orange), and red colours, respectively

under the Fermi level, unoccupied defect states are localized close to the conduction band. The band gap was calculated to be 1.16 eV. According to the PDOS, these states originated from  $\text{Ti}_{5c}$  and  $\text{Ti}_{4c}$  atoms having extra unsaturated bonds from the formation of oxygen vacancy. For the  $\text{TiO}_2(\text{V}_{02})$  band structure, while two occupied defect degenerate states appear under the Fermi level, unsaturated defect states are localized in the conduction band. The band gap was found as 1.08 eV. At the PDOS, these states originated from  $\text{Ti}_{5c}$  and  $\text{Ti}_{4c}$  atoms from the formation of oxygen vacancy.

### 5.2.3 Adsorption of Coumarin 153

#### 5.2.3.1 Adsorption on $\text{TiO}_2$

In this part, we examined the adsorption of C153 molecule on perfect and oxygen-vacancy  $3 \times 1$  anatase (101) surface. The binding geometries and band structures are shown in Figure 5.3. The relevant atomic geometries are listed in Table 5.1.

Table 5.1: Average bond lengths, electronic band gap, and adsorption energies of C153 adsorbed on both the anatase surface and the surface having O-vacancies.

	$E^{ads}$ (eV)	$E_g$ (eV)	Atomic Distance ( $\text{\AA}$ )				
			Ti1- $O_m$	Ti2- $O_m$	Ti1- $O_s$	Ti2- $O_s$	C- $O_m$
C153/TiO <sub>2</sub>	0.77	1.95	2.36		2.03	2.06	1.24
C153/TiO <sub>2</sub> (V <sub>01</sub> 1)	1.24	1.16	2.31	2.39	2.04	1.93	1.27
C153/TiO <sub>2</sub> (V <sub>02</sub> )	1.78	1.08	2.34	2.50	2.06	1.98	1.29
			Ti1- $O_m$	Ti2-F	Ti3-F	F-C	C- $O_m$
C153/TiO <sub>2</sub> (V <sub>01</sub> 2)	2.45	1.98	2.32	2.76	2.33	1.43	1.24
			Ti1-Pr	O <sub>s</sub> 1-Pr	O <sub>s</sub> 2-Pr	Pr- $O_m$	C- $O_m$
Pr/TiO <sub>2</sub>	6.92	2.15	3.29	2.20	2.44		
C153/Pr/TiO <sub>2</sub>	1.16	0.55	3.33	2.22	2.57	2.38	1.25

Only one stable adsorption geometry was identified for C153 on the perfect surface, denoted by C153/TiO<sub>2</sub>. Three different geometries were which will refer to as C153/TiO<sub>2</sub>(V<sub>01</sub>1), C153/TiO<sub>2</sub>(V<sub>01</sub>2) and C153/TiO<sub>2</sub>(V<sub>02</sub>). All four geometries and their band structures are shown in Figure 5.4. Here, the edge oxygen atom of the molecule ( $O_m$ ) is in touch with the vacancy site for both C153/TiO<sub>2</sub>(V<sub>01</sub>1) and C153/TiO<sub>2</sub>(V<sub>02</sub>). As for C153/TiO<sub>2</sub>(V<sub>01</sub>2), while the F atom of molecule setted on the V<sub>01</sub> side, the edge atom adsorbed on surface of Ti atom.

In the C153/TiO<sub>2</sub> geometry the initial geometry is chosen almost vertical to the surface. After the relaxation process, one O atom at edge of molecule formed a fivefold coordinated surface Ti<sub>5c</sub> atom. The adsorption energy is calculated to be 0.77 eV. The distance between molecule  $O_m$  atom and surface Ti<sub>5c</sub> atom is about 2.36  $\text{\AA}$ . On the defective surface, on the other hand no other binding geometries were identified. C153 causes two states to appear in the band gap below the Fermi level. This causes, a narrowing of the electronic band gap of formed a bond with was found 1.95 eV. As seen from the PDOS analysis displayed next to the band structure to be molecule atoms C, N, O are more localized in the impurity band under the Fermi level, which are shown as green, violet and red peaks in the PDOS plot. However, states from O atoms in the molecule are predominantly localized in the lowest gap state.

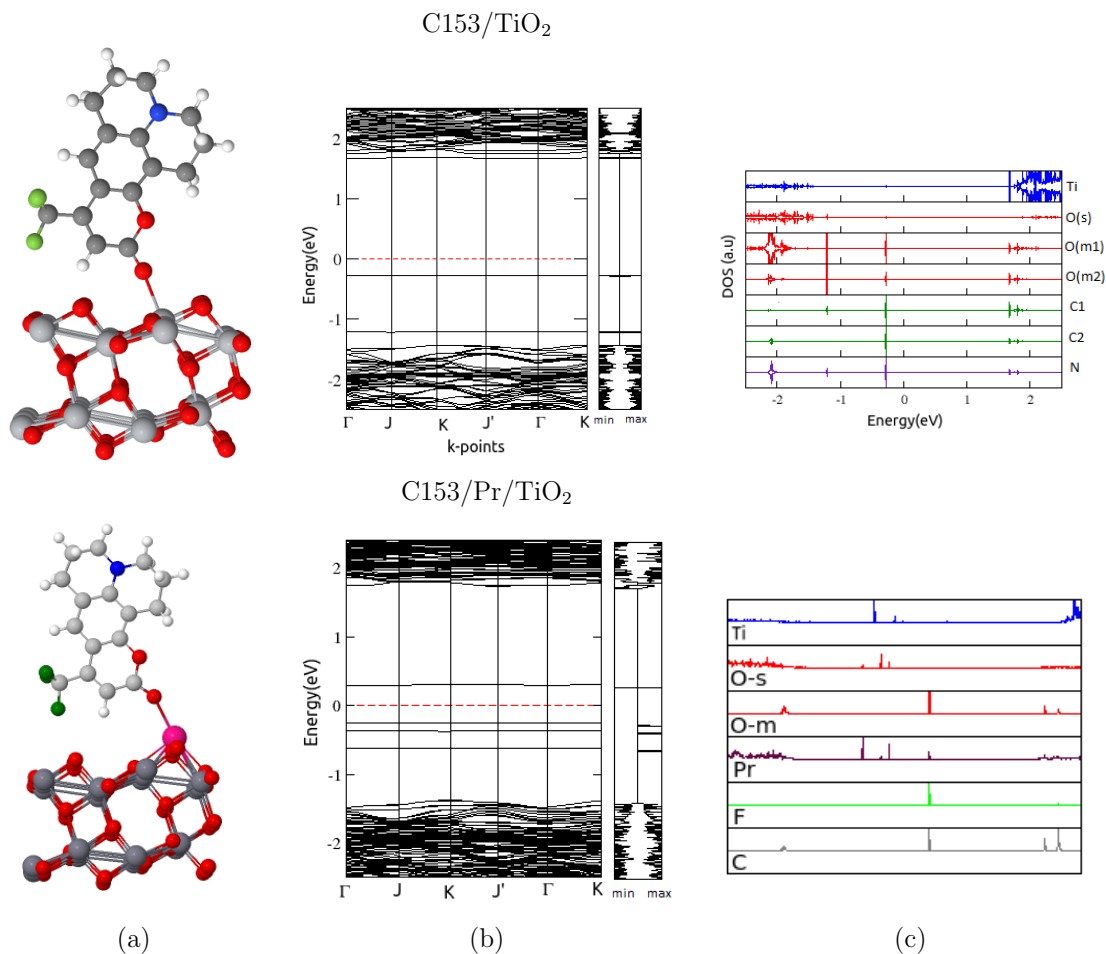


Figure 5.3: The geometric and electronic structures of three adsorptional cases for C153:TiO<sub>2</sub> and C153/Pr/TiO<sub>2</sub> system. While the first column (a) represents the atomic structure case, the second and third columns; (b), (c) represent energy bands and DOS structures.

The adsorption energy C153/TiO<sub>2</sub>(V<sub>01</sub>1), was calculated 1.24 eV. For the most stable position, the distance between the oxygen atom of the molecule and the surface Ti<sub>5c</sub> atom (Ti1-O<sub>m</sub>) was found to be 2.31 Å. For C153/TiO<sub>2</sub>(V<sub>01</sub>2) the highest adsorption energy was found to be 2.45 eV. The F-C bond increases slightly in length from 1.36 Å to 1.43 Å upon the formation of adsorption. For C153/TiO<sub>2</sub>(V<sub>02</sub>), the adsorptional energy was calculated as 1.78 eV. This is higher than the value of C153/TiO<sub>2</sub>(V<sub>01</sub>1). On the reduced surfaces, terrace-vacancy is more reactive than step-oxygen vacancy site.

According to the electronic band structure of C153/TiO<sub>2</sub>(V<sub>01</sub>1), the four impurity states originating from the C153 molecule adsorption are higher in energy in

the band structure. The Fermi energy resides between conduction and valence bands with three impurity states below. An additional impurity state is seen above the Fermi level. As seen in the PDOS analysis, the energy level originating from Ti  $3d$  orbital is 0.3 eV under Fermi level. Other states originating from the C153-surface interaction are located close to valence band. States of the C153 atoms are more dominant in the empty state located above the Fermi level. The band gap is calculated to be 1.16 eV. In the band structure of C153/TiO<sub>2</sub>(V<sub>02</sub>), four defect states are located under the Fermi level. Two unoccupied degenerate states are above the level. In the PDOS analysis, the two defect states located the closest to Fermi level originate from the Ti  $3d$  orbital. The band gap is 1.08 eV. For C153/TiO<sub>2</sub>(V<sub>012</sub>), the occupied states under Fermi level are very close to each other as unlike other band structures. One unoccupied state is located closed to conduction band. Between Ti and atoms of molecule interaction is more reactive in these occupied states. The un occupied state is originated from surface and molecule atom interaction. The band gap is calculated to be 1.98 eV. This value is quite high compared to the previous one.

Our results indicate weak interaction between the C153 molecule and the surface. The adsorption energy increases in the presence of vacancies and the structures becomes magnetic.

### 5.2.3.2 Adsorption on Pr/TiO<sub>2</sub>

In this subsection, we investigate the physical behaviour C153 adsorbed on the surface with a Pr impurity atom. The most stable location for the Pr atom was identified and chosen as the anchor site with an adsorption energy of 6.92 eV. On this site, a single C153 adsorption geometry was considered, where the molecule is vertical to the surface. The adsorption energy and relevant structural parameters of C153 is listed table 5.1 and also atomic band structure and density of states are indicated in the Figure 5.3. Here,  $U$  values were taken 5 eV for Pr atoms.

The C153 adsorption geomerty, one O atom at the edge of the molecule is bounded to the Pr atom located on the surface. The adsorption energy was

Table 5.2: Bader charge analysis results for C153/TiO<sub>2</sub>(101) anatase systems. For labeling refer to Fig 5.3 5.4

Model	$\mu_B$	Ti1	Ti2	Ti3	O(s1)	O(s2)	O(m1)	O(m2)
bare		+2.04	+2.05	+2.06	-1.08	-1.07		
C153							-1.09	-1.04
C153/TiO <sub>2</sub>		+2.09			-1.07	-1.06	-1.10	-0.99
TiO <sub>2</sub> (V <sub>01</sub> )	1.99	+1.72	+1.77	+2.04	-1.09	-1.12		
C153/TiO <sub>2</sub> (V <sub>01</sub> 1)	2.00	+1.85	+2.05		-1.07	-1.12	-1.16	-1.01
C153/TiO <sub>2</sub> (V <sub>01</sub> 2)	2.00	+1.81	+1.83	+2.05	-1.12	-1.13	-1.05	-1.01
TiO <sub>2</sub> (V <sub>02</sub> )	0.00	+1.77	+1.73	+1.83	-1.11	-0.94		
C153/TiO <sub>2</sub> (V <sub>02</sub> )	2.00	+1.83	+1.82	+2.05	-1.12	-0.93	-1.15	-0.98
Pr/TiO <sub>2</sub>	5.00	+2.00	+2.05	+1.81	-1.14	-1.24		
C153/Pr/TiO <sub>2</sub>	5.00	+2.00	+1.81	+1.84	-1.14	-1.22	-1.22	-1.03
		C1	C2	N	F	H	Pr	
C153		+1.38	-0.02	-1.13	-0.61	-0.14		
C153/TiO <sub>2</sub>		+1.25	+0.08	-1.15	-0.60	+0.19		
C153/TiO <sub>2</sub> (V <sub>01</sub> 1)		+1.16	+0.07	-1.17	-0.60	+0.21		
C153/TiO <sub>2</sub> (V <sub>01</sub> 2)		+1.31	+0.05	-1.16	-0.63	+0.12		
C153/TiO <sub>2</sub> (V <sub>02</sub> )		+1.17	-0.02	-1.22	-0.57	-0.29		
C153/Pr/TiO <sub>2</sub>							+1.99	
C153/Pr/TiO <sub>2</sub>		+1.32	+0.02	-1.05	-0.56	+0.22	+2.05	

calculated to be 1.16 eV. This is a medium value when compared to other models. The length of the Pr-O<sub>m</sub> bond 2.38 Å. A value very close to the BZA adsorption geometries on TiO<sub>2</sub> (101). Considering the binding energy as an indicator of the degree of interaction between C153 and the surface, we can conclude that this adsorption structure is less strong than vacancy applications.

The band gap of this system is seen to decrease until 0.55 eV. The Fermi energy appeared between conduction and valance bands. While three occupied defect states appear under the Fermi level, one unoccupied defect state is located 1.50 eV below the conduction band. According to the PDOS graph, while between Ti, O and Pr contribution is more dominant in the occupied defect states, the defect state located under the conduction band originates from Pr and C153 interaction. This unoccupied state is closer to the Fermi energy level as compared to benzoic acid application. The band gaps of all C153 in applications of adsorption seems appropriate for the visible region.



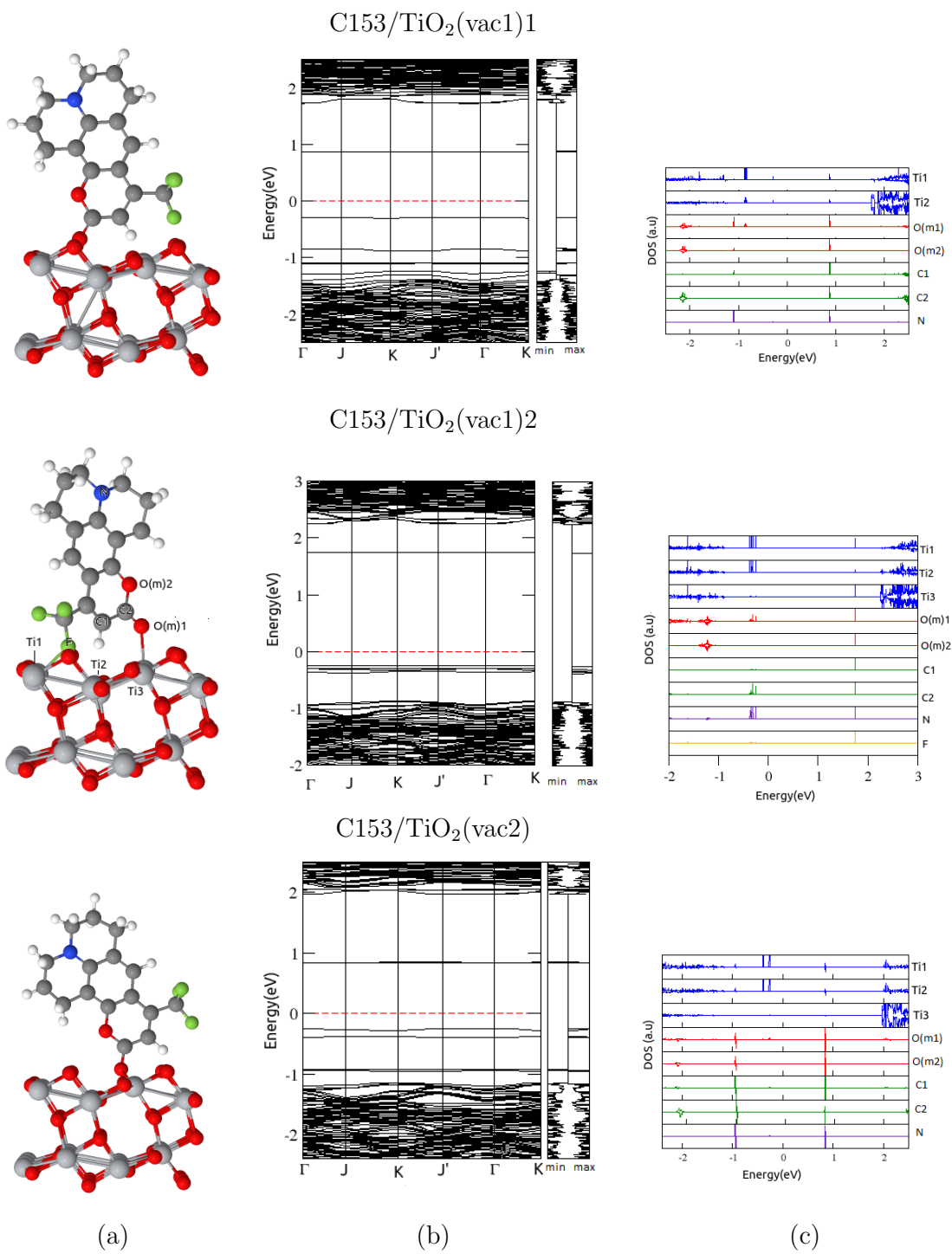


Figure 5.4: The geometric and electronic structures of three adsorptional cases for C153/TiO<sub>2</sub>(V<sub>01</sub>1), C153/TiO<sub>2</sub>(V<sub>01</sub>2) and C153/TiO<sub>2</sub>(V<sub>02</sub>) systems. While the first column (a) represents the atomic structure case, the second and third columns; (b), (c) represent energy bands and DOS structures.

Bader charge analysis results comprise for the C, O<sub>m</sub>, N, F and H atoms in the C153 molecule; Ti and O surface atoms; and the Pr atom reported in table 5.2. As expected, the maximum change in charge for Ti atoms is seen at the C153/TiO<sub>2</sub>(V<sub>02</sub>) structure, since, one oxygen atom O(m1) located at the edge of the molecule interacts with of three unsaturated Ti atoms. Charge differences in surface oxygen atoms (O(s)) are rather low, they are appreciable only in the model the C153/Pr/TiO<sub>2</sub>. The highest charge transfer is observed for O(m1) for C153/Pr/TiO<sub>2</sub> whereas almost no charge is seen for C153/TiO<sub>2</sub>. For the C1, O(m1) atom, the charge transfer is highest in the C153/TiO<sub>2</sub>(V<sub>01</sub>) and TiO<sub>2</sub>(V<sub>02</sub>) structures. This shows that the charge interchange is strong between the atoms of molecule.

#### 5.2.4 Optical Properties

The optical absorbance spectra of the systems are considered as shown in the visible range Fig. 5.5 left-hand panel (a, c, e), and in the near infrared range Fig. 5.5 on the right-hand panel (b, d, f). Here, the two ranges are determined as ultraviolet-visible (UV-vis,  $\lambda=100-800$  nm) and the near to far infrared (IR,  $\lambda=800-14000$  nm). As in the previous sections, the bare TiO<sub>2</sub>(101)-3 $\times$ 1 surface shows a large peak in the UV range (between 150–400 nm). Other structures display similar performance in this range. In the visible part of the spectrum, while absorption for perfect surface shows no absorption, absorption lines of O-vacancies and Pr-doped systems indicate an improvement. Particularly, TiO<sub>2</sub>(V<sub>02</sub>) system shows the best absorption performance. After the adsorption of C153 molecule, while C153:TiO<sub>2</sub> shows a very similar performance to the bare surface in the visible range (Fig. 5.5(c)), absorption lines of C153/Pr/TiO<sub>2</sub> system indicates an improvement with the good absorbance performance after the region 600 nm. Indeed, C153/TiO<sub>2</sub>(V<sub>01</sub>1) indicates the best absorption performance, when it is compared to other C153 adsorption systems (Fig. 5.5(e)). In the near-IR region shown in Fig. 5.5 on the right-hand panels, while the bare surface and C153/TiO<sub>2</sub> demonstrate no signal at all while other configurations remain active, O-vacancies systems indicate absorption performance. In C153/TiO<sub>2</sub>(V<sub>01</sub>1), the absorbance maximum appears around 2600 nm, then

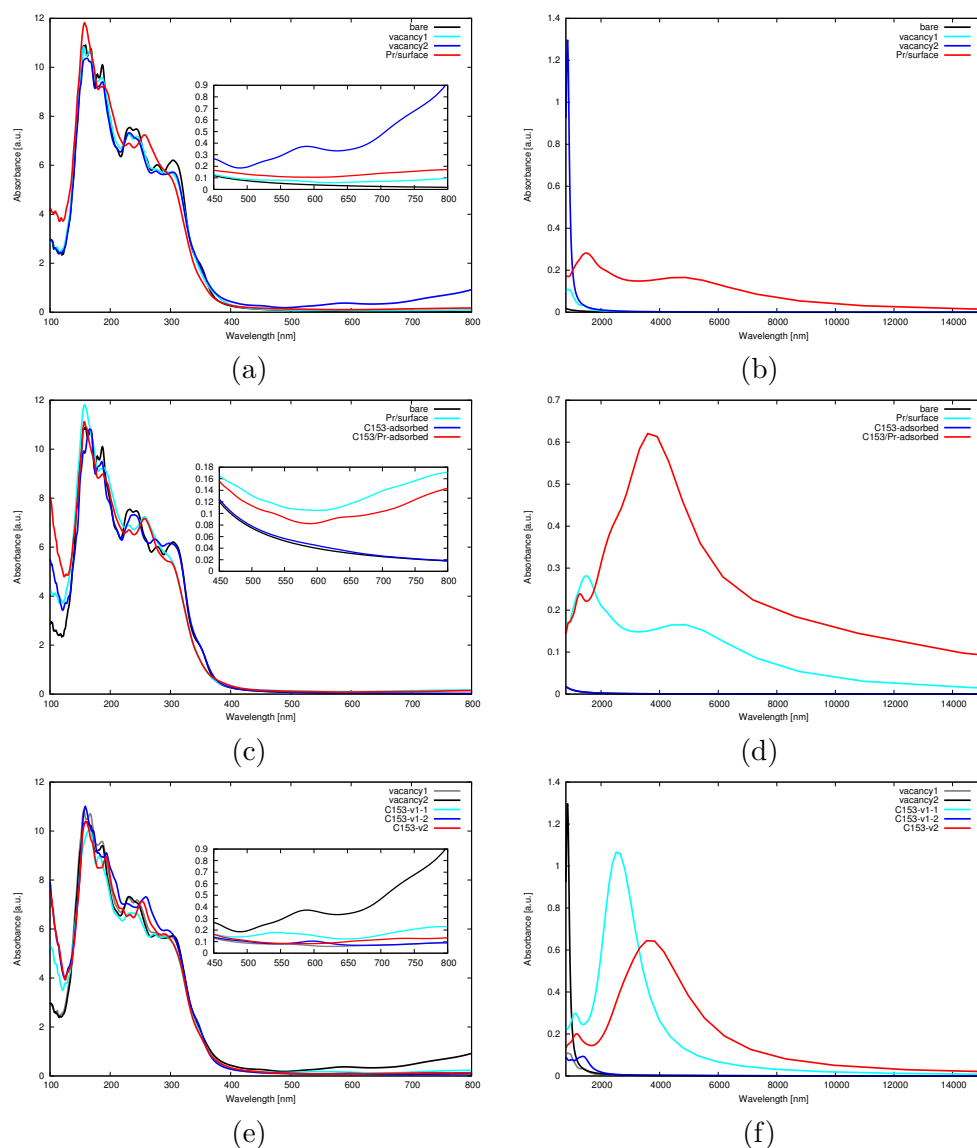


Figure 5.5: The optical absorbance of bare, O-vacancies and Pr-doped  $\text{TiO}_2(101)\text{-}3\times 1$  surfaces (a, b), cases for  $\text{C153}:\text{TiO}_2$  and  $\text{C153}/\text{Pr}/\text{TiO}_2$  system (c, d) and cases for  $\text{C153}/\text{TiO}_2(V_{011})$ ,  $\text{C153}/\text{TiO}_2(V_{012})$  and  $\text{C153}/\text{TiO}_2(V_{02})$  systems (e, f). The graphs on the left-hand panel (a, c, e) refer to the visible range and those on the right-hand panel (b, d, f) to the infrared region.

it rapidly loses activity.  $\text{C153}/\text{Pr}/\text{TiO}_2$  displays good activity between visible and the near-IR edge. Although the peak of  $\text{C153}/\text{TiO}_2(V_{02})$  appears around 4000 nm, it is lower than that of  $\text{C153}/\text{TiO}_2(V_{011})$ .  $\text{C153}/\text{TiO}_2(V_{011})$  shows absorbance at longer range with its performance reaching zero around 8000 nm. Although  $\text{C153}/\text{TiO}_2(V_{012})$  is structure with the strongest molecular adsorption

on the surface, it does not show very effective performance at the both visible and infrared regions.

## CHAPTER 6

### BEYOND PR

In this section, we explore the performance of the other lanthanides in place of Pr and the compare performances. Lanthanides are usually known with similar physical properties, so it might be interesting to see how they would behave from optical performance point of view. The lanthanides investigated here were chosen according to the occupancy rate of the  $f$  – *orbitals* of atoms. Considering Pr atom has the two electron  $f$  – *orbitals*, investigation of the absorption behavior for  $f$  – *orbital* electrons of lanthanides with more is interesting. Therefore, three types lanthanide adatoms, Gd, Er, and Lu on TiO<sub>2</sub> surface have been studied. Gadolinium (Gd) has a set of 7 electrons in half-field  $4f$  orbitals and is frequently used in photocatalytic applications [113]. Erbium (Er) has a set of 11 electrons filled  $4f$  orbital and it is appropriate for photocatalytic application [42]. Lutetium (Lu) has a completely filled  $4f$  orbital. Also, while the Ti<sup>4+</sup> ionic radius is only 0.68 Å, lanthanide ions have much larger radii (Gd<sup>3+</sup>(0.94Å), Er<sup>3+</sup>(0.88Å), and Lu<sup>3+</sup>(0.85Å)).

#### 6.1 Computational Method

First principle total energy calculations have been performed within DFT+U as in the previous chapters. The valence atomic configurations used for the PAW potentials are  $3d^3 4s^1$  for Ti and  $2s^2 2p^4$  for O, also  $5s^2 5p^6 4f^7 5d^1 6s^2$  for Gd,  $5s^2 5p^6 4f^{11} 5d^1 6s^2$  for Er, and  $5s^2 5p^6 4f^{14} 5d^1 6s^2$  for Lu, respectively. The charge analysis was done by using the Bader method. The cut off energy was 500 eV. Hubbard Terms (U) were chosen to be,  $U-J = 6.00 5.80 3.88$  eV for Gd,

Table 6.1: Adsorption energy and average bond lengths of Ln adsorbed on the surface.

	$E^{ads}$ (eV)	$\mu_B$	Atomic Distance ( $\text{\AA}$ )					
			Ti(1)-Ti(2)	Ti(1)-O(1)	Ti(1)-O(2)	Ln-Ti(1)	Ln-O(1)	Ln-O(2)
pure			3.12	1.88	2.03			
Gd:TiO <sub>2</sub>	4.20	-6.00	3.15	2.13	2.14	3.10	2.08	2.18
Er:TiO <sub>2</sub>	7.35	2.00	3.14	2.07	2.19	3.13	2.18	2.33
Lu:TiO <sub>2</sub>	7.74	3.00	3.13	2.12	2.19	3.03	1.96	2.04

Er, Lu, respectively as literature [114, 115].

## 6.2 Result and Discussions

### 6.2.1 Adsorptional Cases for a Single Lanthanides

The energetically most favorable adsorption site was chosen for all calculations in this part, where two O<sub>2c</sub> atoms lie along a row on an elevated portion of the (101) surface. Pr(a-2) adsorption model defined previously Chapter 3. Adsorption structure and its band structure had been considered to be stable state for a single lanthanide atoms (Gd, Er, Lu) on the surface, as shown in Figure 6.1(a). Adsorption energies and related structural parameters for the four RE metals adsorption on TiO<sub>2</sub> obtained from our calculations are summarized in Table 6.1. We found that the adsorption energies of Er and Lu adsorbed on the surface are large, 7.35 eV and 7.74 eV, respectively, while that of Gd is relatively smaller with a value of 4.20 eV. When the structures are examined in terms of their bond lengths, Lu bond length between the surface atoms are less than the length of the other adsorbed structures. For example, the distance between Lu and O(1) was found to be 1.96  $\text{\AA}$ , while the same distance in Er adsorption structure is 2.18  $\text{\AA}$ . There is 0.22  $\text{\AA}$  difference between them. For all cases, the magnetic moment has three different values, such as 6.00 for Gd, 2.00 for Er and 3.00 for Lu  $\mu_B$ .

In relation to the electronic band structures and PDOS of Ln adatom TiO<sub>2</sub>

which are shown as Figures 6.1(b) on the leftmost panel, for Gd:TiO<sub>2</sub>, three full occupied impurity states are located below the Fermi energy. Similarly, Gd, Ti and also O atoms interactions is more dominant in these states. As for Er:TiO<sub>2</sub>, the electronic band structure of this case is very different from Gd:TiO<sub>2</sub>. The impurity states under the Fermi level resides closer to the conduction band. These new impurity states are induced by *f* orbitals so Er is more dominant. The states which are located closed to the Fermi level are dispersionless. For Lu:TiO<sub>2</sub>, three impurity states are in the middle of the gap and under the Fermi level. Interaction between impurity and surface atoms is more dominant in these impurity band state. Two occupied energy states are nearly degenerate along the  $\overline{JK}$  direction. Two dispersionless impurity states are originate from the Lu atom are located in the conduction band.

According to Bader charge analysis of adsorptional structures studied here listed in the Table 6.2. The highest change in the charge of the Ln ion is realized in the Lu:TiO<sub>2</sub> structure, with  $Q_{Lu} = +1.96e$ . Also, in same structure, the charge changes for O atoms are the highest a compared with other structures. For Gd:TiO<sub>2</sub>, these charge values have the lowest value. These results are consistent with that obtained from adsorption energies. The charge values for the Ti atoms are slightly different from each other for these structures. On the basis of these results, we can consider that the Ln–O interaction is the stronger than Ln–Ti interaction. Considering the band gap of these structures, while the band gap is 2.01 eV for Gd:TiO<sub>2</sub> and 1.91 eV for Lu:TiO<sub>2</sub>, which are close to each other, it is quite small from the other values with 0.91 eV for Er:TiO<sub>2</sub>.

Table6.2: Bader charges ( $|e|$ ) and band gap of Ln (Gd, Er, Lu) adsorption geometries on the TiO<sub>2</sub>.

	$E_g$ (eV)	Charges					
		Ti1	Ti3	O1	O2	O3	Ln
pure	2.89	+2.04	+2.04	-0.91	-1.08	-0.91	
Gd:TiO <sub>2</sub>	2.01	+1.81	+1.81	-1.12	-1.17	-1.14	+1.27
Er:TiO <sub>2</sub>	0.91	+1.81	+1.85	-1.16	-1.22	-1.16	+1.51
Lu:TiO <sub>2</sub>	1.91	+1.80	+1.80	-1.23	-1.26	-1.20	+1.96

The optical absorbance spectra of  $\text{TiO}_2$ ,  $\text{Gd}/\text{TiO}_2$ ,  $\text{Er}/\text{TiO}_2$ , and  $\text{Lu}/\text{TiO}_2$  samples are considered as shown in for visible range Fig. 6.2(a) and for near infrared range Fig. 6.2(b). The bare  $\text{TiO}_2(101)$  surface displays a large peak in the UV range (between 150–400 nm), also other structures having lanthanide impurity atom show similar performance in this range. While the absorbance rapidly decreases and approaches zero around wavelength of 400 nm for bare  $\text{TiO}_2$  surface, declining absorbance curves remain above zero for the doped structures. In the visible part of the spectrum,  $\text{Gd}/\text{TiO}_2$  shows the best performance in the region until 650 nm, and also  $\text{Gd}/\text{TiO}_2$  and  $\text{Lu}/\text{TiO}_2$  indicate similar activity at the 500-550 nm range. After than, the curve of  $\text{Lu}/\text{TiO}_2$  is seen slight decline. In the near-IR region, the best absorbance performance maximum appears for  $\text{Gd}/\text{TiO}_2$  around 4000 nm. After 6000 nm,  $\text{Er}/\text{TiO}_2$  shows the largest absorbance activity.

### 6.2.2 Benzoic Acid Adsorbed on Ln/ $\text{TiO}_2$ Surface

In this section, BZA adsorbed on the Ln-enriched surface was investigated. Here, we have taken one adsorption structure for each Ln. This structure was chosen to be the energetically most favorable adsorption site for BZA, as known previous section. Adsorption structures and its band structures had been considered to be stable state for a BZA on the Ln/ $\text{TiO}_2$  surface, as shown in Figure. 6.4 and relevant geometrical properties are listed in Table 6.3. The BZA adsorption energies in the presence of Gd structure are greater than that of Er and Lu. Ln- $\text{O}_m$  distances are found to be 2.57 Å for Gd, 2.51 Å for Er, and 2.49 Å for Lu.

For this adsorptional geometry, a comparison of the band structures and density of states of adsorbed BZA on Ln-doped surface is shown in Figures 6.4. Overall, for BZA/Er: $\text{TiO}_2$  structure, the number of impurity states that originate from Er impurity are atom located in the band gap decreased after benzoic acid adsorbed on the surface. For BZA/Gd: $\text{TiO}_2$  and BZA/Lu: $\text{TiO}_2$  structures, the number of impurity states located under the Fermi level remains same after the benzoic acid adsorption. As can be seen from PDOS analysis, interaction



Table 6.3: Average bond lengths ( $\text{\AA}$ ) and adsorption energies (eV) of benzoic acid adsorbed on  $\text{TiO}_2$  and Ln/ $\text{TiO}_2$ .

	$E^{ads}$ (eV)	$\mu_B$	Atomic Distance ( $\text{\AA}$ )						
			Ti-Ti	Ti-O1	Ti-O2	Ln-Ti	Ln-O <sub>s1</sub>	Ln-O <sub>s2</sub>	Ln-O <sub>m</sub>
BZA/Gd: $\text{TiO}_2$	3.23	4.00	3.16	2.13	2.15	3.14	2.12	2.22	2.57
BZA/Er: $\text{TiO}_2$	1.20	4.00	3.16	2.06	2.20	3.13	2.13	2.15	2.51
BZA/Lu: $\text{TiO}_2$	1.35	3.00	3.09	2.10	2.19	3.08	1.98	2.08	2.49

between impurity and surface atoms plays a dominant role in these states. As for these three structure, flat empty states appear above the Fermi energy level. In these states, interaction between molecules impurity atoms located on the surface is the dominant. Clearly appearing BZA/Er: $\text{TiO}_2$ , some flat empty states appear originating from Er. Two occupied energy states are nearly degenerate along the  $\overline{JK}$  direction.

Bader charge analysis of BZA adsorptional structures, as shown in the Table 6.4 indicated that the highest change in the charge for the Ln atoms are realized in the BZA/Gd: $\text{TiO}_2$  structure, which increases from  $Q_{Lu} = +1.27e$  (as seen from Table 6.2) to  $Q_{Lu} = +2.00e$ . Similarly, the charge changes for O (O1 and O2) atoms of surface has the highest value in this structure, when compared with other structures. This result is consistent with the high binding energy on Gd. The charge values for the Ti atoms are almost unchanged for all structures. Considering the band gap of these structures, the band gap have found as 0.96 eV for BZA/Gd: $\text{TiO}_2$  and 1.00 eV for BZA/Lu: $\text{TiO}_2$ , which are close to each other. Here, after adsoption of BZA, the band gaps decrease for these structure. However, band gap increases from 0.91 eV to 1.50 eV after BZA adsorbed on Er-doped  $\text{TiO}_2$  surface. These band gap values for all structures are consistent for absorbance in the visible region.

After, BZA has been adsorbed on the surface on which has lanthanite impurity atoms, the absorption spectrum both VR- and IR- were shown in Fig. 6.3 When these three structures are compared in the visible-light region, the most significant differences in the absorption spectrum is the fact that the absorption performance of BZA/Gd: $\text{TiO}_2$  is the best. In the near-IR region, BZA/Gd: $\text{TiO}_2$

Table6.4: Bader charge and band gap values of BZA adsorbed on Ln:TiO<sub>2</sub>.

	E <sub>g</sub> (eV)	Bader Charges								
		Ti	O1	O2	Ln	O1 <sub>m</sub>	O2 <sub>m</sub>	C <sub>a</sub>	C <sub>b</sub>	H
BZA						-1.12	-1.09	+1.39	-0.02	+0.59
BZA/Gd:TiO <sub>2</sub>	0.96	+1.81	-1.19	-1.27	+2.00	-1.19	-1.11	+1.37	-0.14	+0.65
BZA/Er:TiO <sub>2</sub>	1.50	+1.82	-1.16	-1.25	+2.05	-1.20	-1.11	+1.37	-0.03	+0.65
BZA/Lu:TiO <sub>2</sub>	1.00	+1.81	-1.24	-1.27	+2.02	-1.16	-1.18	+1.42	+0.11	+0.73

system indicate the maximum absorption performance around 2000 nm, then it rapidly loses activity. After 4000 nm, BZA/Gd:TiO<sub>2</sub> and BZA/Lu:TiO<sub>2</sub> systems display same absorbance performance. In BZA/Er:TiO<sub>2</sub>, the best absorbance performance appears around 6000 nm .

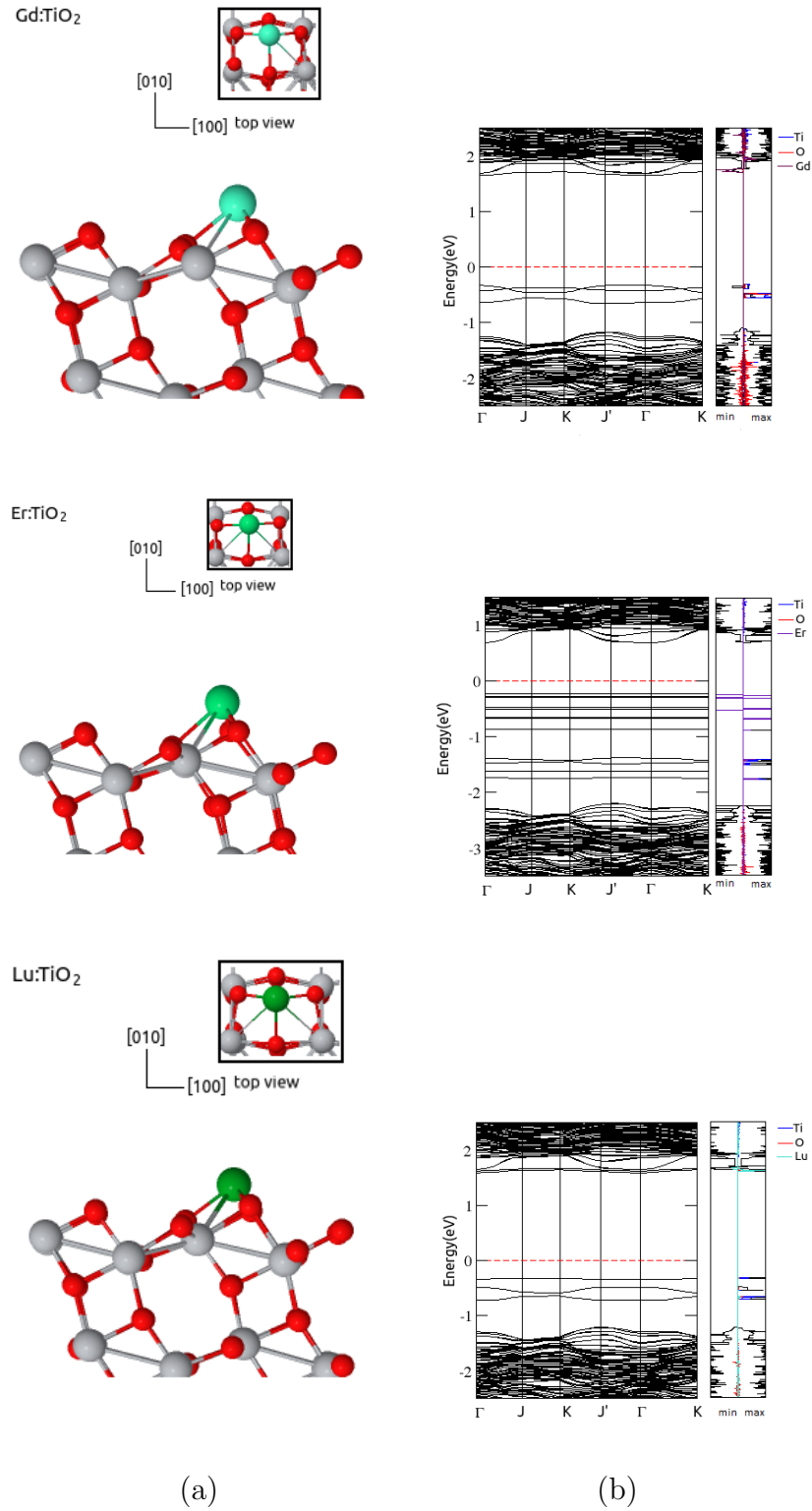


Figure 6.1: The geometric and electronic structures of adsorptional cases for Gd:TiO<sub>2</sub> systems, Er:TiO<sub>2</sub>, and Lu:TiO<sub>2</sub> systems, respectively. While the first column (a) represents the atomic structure case, the second and third columns; (b) represent energy bands and DOS structures.

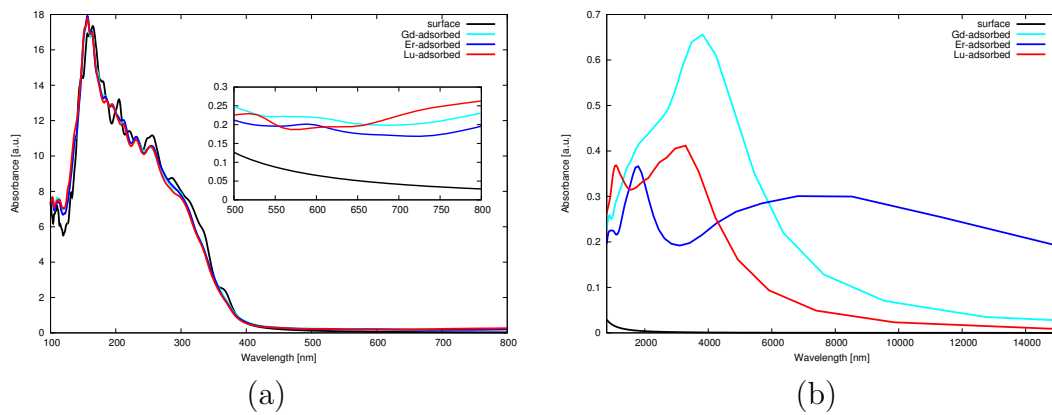


Figure 6.2: The optical absorption spectra of Ln (Gd, Er, Lu) adsorbed on  $\text{TiO}_2$  models at (a) visible and (b) infrared ranges.

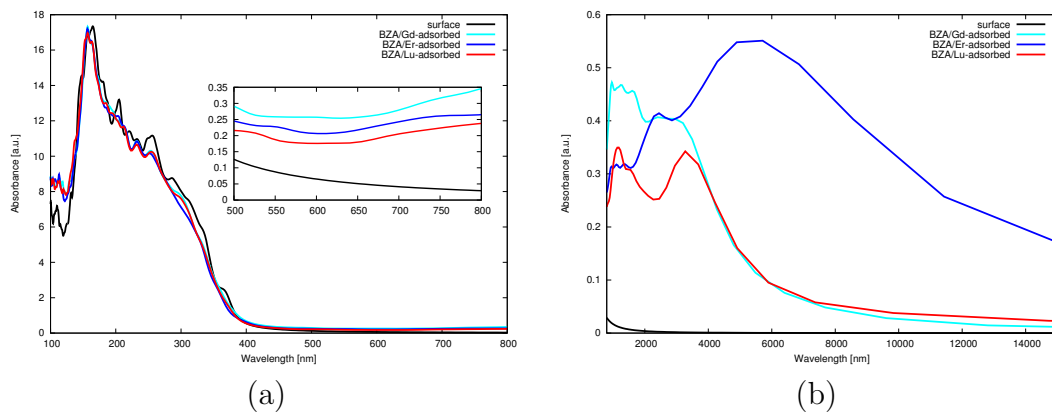
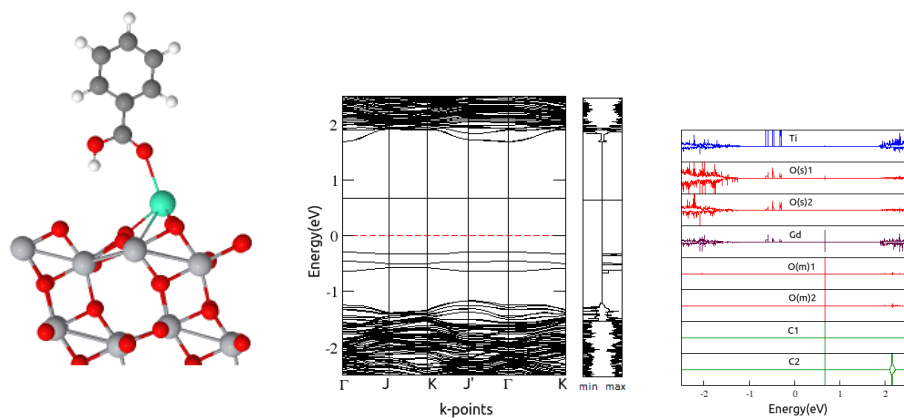
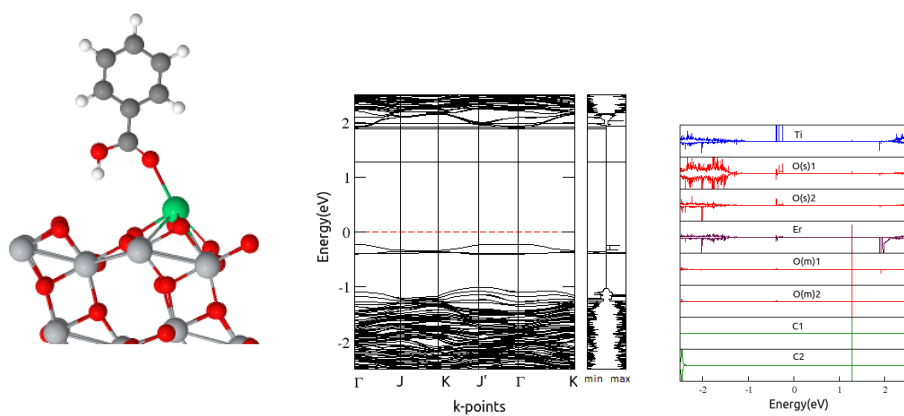


Figure 6.3: The optical absorption spectra of BZA adsorbed on Ln(Gd, Er, Lu)/ $\text{TiO}_2$  models at (a) visible and (b) infrared ranges.

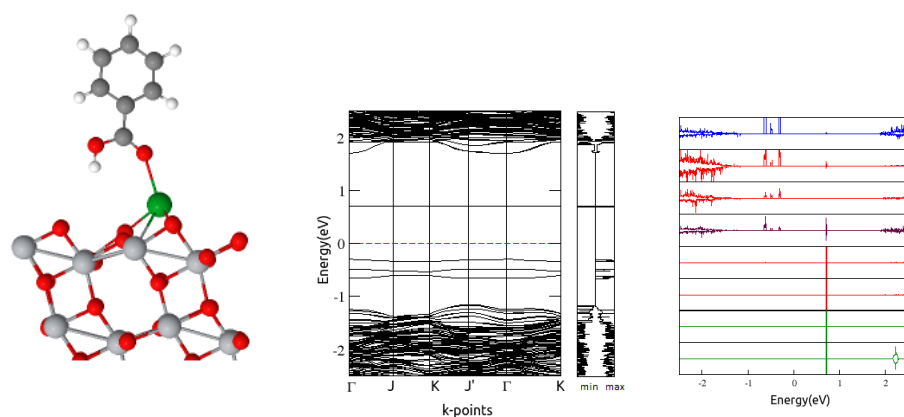
BA/Gd:TiO<sub>2</sub>



BA/Er:TiO<sub>2</sub>



BA/Lu:TiO<sub>2</sub>



(a)

(b)

(c)

Figure 6.4: The geometric and electronic structures of adsorptional cases for BZA/Gd:TiO<sub>2</sub> systems, BZA/Er:TiO<sub>2</sub> and BZA/Lu:TiO<sub>2</sub> systems. While the first column (a) represents the atomic structure case, the second and third columns; (b), (c) represent energy bands and DOS structures.



## CHAPTER 7

### CONCLUSION

TiO<sub>2</sub> supported with atoms or molecules is generally used as an active system for photocatalytic applications. Rare-earth metals are considered highly appropriate dopants due to the enhanced photocatalytic activity of TiO<sub>2</sub>. The absolute value of  $U$  for  $d$ -orbitals of Ti atom has not yet been reported in the literature. In chapter 3, we filled this gap by recalculating the band gap and lattice constants of the bulk anatase TiO<sub>2</sub> for varied  $U$  values. Based on these calculation results, we obtained a fitting  $U$  value. In order to calculate the  $U$  value for  $f$ -orbitals of Pr atom, we used Pr-oxide bulk structure (Pr<sub>2</sub>O<sub>3</sub>). Although the existing literature had reported a number of specific values of  $U$ , we could not find a trend among these reported values. Therefore, we have considered the varying  $U$  values both for  $d$ -orbitals of Ti and  $f$ -orbitals of Pr atoms and the adsorption processes were recalculated. These calculations have shown that there are no structural and electronic change is conditional on the different  $U$  values for Pr atom. The differences which occur at the band gaps, on the other hand, stem from the different  $U$  values for Ti atom. For adsorptional proceses, we have examined the structural, electronic and optic properties of the interaction between Pr atom and anatase (101) reconstructed surface are investigated. The stable geometries for each metal and surface atom have been obtained by relaxation to minimum total energy. According to our results, since interaction between Pr and the surface atoms is strong and the actual radius of Pr is more than the surface of the atoms, changing of the positions of the surface atoms with presence of Pr was appeared. This change can be seen most clearly for the interaction between Ti and Pr atoms. Furthermore, a strong binding geometry is obtained

from Pr interaction between both Ti and O atoms. Bader charge analysis has supported this result depending on the higher charge transfer between atoms. Finally, after the adsorption process, the structure gained magnetic properties. When evaluated in terms of optical properties, the adsorption of Pr is also a good method for increasing the absorbance both in the visible and the infrared range. When evaluated in terms of optical properties, we demonstrated that the adsorption of Pr is also a useful method to increase the absorbance performance of TiO<sub>2</sub> both in the visible and the infrared range.

Pr shows high performance as an anchor for dye molecules. The adsorbance of benzoic acid is strong, providing that the presence of Pr impurity atoms on the surface that otherwise weakly interact with the surface. Again, due to the presence the Pr atom, the band structures of the adsorptional systems have become as convenient for visible region. As a result of this, they have exhibited the better optical absorption behavior in the visible-light region. While adsorption of benzoic acid on the bare surface structures showed no absorbance properties in the infrared region, the Pr-doped surface indicated impressive performance in this region. Adsorptional structures having Pr-doped substrate have gained magnetic property.

We have studied the inteaction Coumarin 153 (C153) and clean, Pr-doped and reduced (O-vacancy) surface. The first, the O-vacancy proceses have been investigated. After O-vacancies process, the surface of the band gap was narrowing due to grow number of unsaturated atoms on the surface. Interaction between C153 molecule and the clean nanowire was realized weaker interaction when considering the binding energy. However, C153 binds to Pr-doped or reduced nanowire structures more strongly. The strongest binding model was obtained from the adsorption of two ends of the C153 molecule on O-vacancy nanowire. In terms of the strength of the adsorption, the creation of O-vacancy seems to be a more effective method than the Pr-doped. But, when considering their performance of absorbance, two methods give similar results at the visible range. Adsorptional structures having both the O-vacancy and Pr-doped substrates gain magnetic properties.



We have examined the adsorption behavior three lanthanide atoms chosen based on 4f-orbital occupancy rate, such as half-filled for Gd, high-filled for Er, and full-filled for Lu. The adsorbance of Lu on the surface is the strongest as compared with others in terms of the binding energy. Bader charge analysis has supported this result. When considering the band structures, for adsorption of both Gd and Lu, similar results have obtained. Whereas, after the adsorption of Er, band structure were obtained a quite different from these structures. It is considered that this result is due to the rate of occupancy in f-orbitals of Er atom. As indicated in the absorbance curves, absorbance activities of these structures are close to each other at visible range. In the infrared region, up to 6000 nm, the absorbance performance of the structure having Gd atom is more highly than others. Considering lanthanide atoms to have similar physical properties, this may be regarded as a distinctive feature. If we discuss based on the calculation result of benzoic acid adsorbed on Ln-doped substrate. The absorbances of benzoic acid on Ln-doped substrates are strong like Pr-doped. The strongest binding model was obtained from the adsorption of benzoic acid on Gd-doped substrate. When considering the band structures, the number of impurity states originated from Er impurity atom located in the band gap decreased and similar results have obtained. According to the absorbance curves, absorbance performance of these structures are near each other at visible range. In the infrared region the absorbance activity of Er-doped substrate is more highly than others.

In this thesis, our results have presented that using dyes together with rare earth elements as surface dopants on TiO<sub>2</sub> substrates could be a controllable and efficient approach for bettering their optical activity. Consequently, investigation of rare-earth metals and more complex dye molecules for solar application idea would obviously important.



## REFERENCES

- [1] M. R. Hoffmann, S. T. Martin, W. Choi, and D. W. Bahnemann. Environmental applications of semiconductor photocatalysis. *Chemical Reviews*, 95(1):69–96, 1995.
- [2] J.-M. Herrmann. Heterogeneous photocatalysis: fundamentals and applications to the removal of various types of aqueous pollutants. *Catalysis Today*, 53(1):115–129, 1999.
- [3] D. P. Daghrir Rimeh and D. Robert. Modified TiO<sub>2</sub> for environmental photocatalytic applications: A review. *Industrial and Engineering Chemistry Research*, 52(10):3581–3599, 2013.
- [4] B. O'Regan and M. Grätzel. A low-cost, high-efficiency solar cell based on dye-sensitized colloidal TiO<sub>2</sub> films. *Nature*, 353:737–740, 1991.
- [5] M. Grätzel. Photoelectrochemical cells. *Nature*, 414:338–344, 2001.
- [6] X. Chen and S. S. Mao. Titanium dioxide nanomaterials: Synthesis, properties, modifications, and applications. *Chemical Reviews*, 107(7):2891–2959, 2007.
- [7] D. Ravelli, D. Dondi, M. Fagnoni, and A. Albini. Photocatalysis. a multifaceted concept for green chemistry. *Chem. Soc. Rev.*, 38(7):1999–2011, 2009.
- [8] M. Kopaczyńska, K. Vargová, M. Wysocka-Król, G. Plesch, and H. Podbielska. Chapter2: Photocatalytic effects in doped and undoped titania. pages 15–25, 2012.
- [9] W. Xu, P. K. Jain, B. J. Beberwyck, and A. P. Alivisatos. Probing redox photocatalysis of trapped electrons and holes on single sb-doped titania nanorod surfaces. *Journal of the American Chemical Society*, 134(9):3946–3949, 2012.
- [10] F. Gao, Y. Wang, D. Shi, J. Zhang, M. Wang, X. Jing, R. Humphry-Baker, P. Wang, S. M. Zakeeruddin, and M. Grätzel. Enhance the optical absorptivity of nanocrystalline TiO<sub>2</sub> film with high molar extinction coefficient ruthenium sensitizers for high performance dye-sensitized solar cells. *Journal of the American Chemical Society*, 130(32):10720–10728, 2008.

- [11] M. O’Neil, J. Marohn, and G. McLendon. Dynamics of electron-hole pair recombination in semiconductor clusters. *The Journal of Physical Chemistry*, 94(10):4356–4363, 1990.
- [12] W. Choi, A. Termin, and M. R. Hoffmann. The role of metal ion dopants in quantum-sized TiO<sub>2</sub>: Correlation between photoreactivity and charge carrier recombination dynamics. *The Journal of Physical Chemistry*, 98(51):13669–13679, 1994.
- [13] S. Sakthivel, S.-U. Geissen, D. Bahnemann, V. Murugesan, and A. Vogelpohl. Enhancement of photocatalytic activity by semiconductor heterojunctions. *Journal of Photochemistry and Photobiology A: Chemistry*, 148(1–3):283–293, 2002.
- [14] S. Sakthivel, B. Neppolian, M. Shankar, B. Arabindoo, M. Palanichamy, and V. Murugesan. Solar photocatalytic degradation of azo dye: comparison of photocatalytic efficiency of zno and TiO<sub>2</sub>. *Solar Energy Materials and Solar Cells*, 77(1):65–82, 2003.
- [15] M. Valenzuela, P. Bosch, J. Jiménez-Becerrill, O. Quiroz, and A. Páez. Preparation, characterization and photocatalytic activity of zno, fe<sub>2</sub>o<sub>3</sub> and znfe<sub>2</sub>o<sub>4</sub>. *Journal of Photochemistry and Photobiology A: Chemistry*, 148(1–3):177–182, 2002.
- [16] M. Grätzel. Dye-sensitized solar cells. *Journal of Photochemistry and Photobiology C: Photochemistry Reviews*, 4(2):145–153, 2003.
- [17] M. A. Fox and M. T. Dulay. Heterogeneous photocatalysis. *Chemical Reviews*, 93(1):341–357, 1993.
- [18] A. Fujishima, X. Zhang, and D. A. Tryk. TiO<sub>2</sub> photocatalysis and related surface phenomena. *Surface Science Reports*, 63(12):515–582, 2008.
- [19] A. Mills and S. L. Hunte. An overview of semiconductor photocatalysis. *Journal of Photochemistry and Photobiology A: Chemistry*, 108(1).
- [20] A. F. nad Kenichi Honda. *Electrochemical Photolysis of Water at a Semiconductor Electrode*, 238:37–38.
- [21] A. Fujishima, T. N. Rao, and D. A. Tryk. Titanium dioxide photocatalysis. *Journal of Photochemistry and Photobiology C: Photochemistry Reviews*, 1(1):1–21, 2000.
- [22] S. N. Frank and A. J. Bard. Heterogeneous photocatalytic oxidation of cyanide ion in aqueous solutions at titanium dioxide powder. *Journal of the American Chemical Society*, 99(1):303–304, 1977.
- [23] B. O’Regan and M. Grätzel. A low-cost, high-efficiency solar cell based on dye-sensitized colloidal TiO<sub>2</sub> films. *Nature*, 353:737–740, 1991.

- [24] M. Grätzel. Photoelectrochemical cells. *Nature*, 414(6861):338–344, 2001.
- [25] M. Grätzel. Solar energy conversion by dye-sensitized photovoltaic cells. *Inorganic Chemistry*, 44(20):6841–6851, 2005.
- [26] T. A. Kandiel, L. Robben, A. Alkaim, and D. Bahnemann. Brookite versus anatase  $\text{TiO}_2$  photocatalysts: phase transformations and photocatalytic activities. *Photochem. Photobiol. Sci.*, 12:602–609, 2013.
- [27] H. Zhang and J. F. Banfield. Thermodynamic analysis of phase stability of nanocrystalline titania. *J. Mater. Chem.*, 8:2073–2076, 1998.
- [28] T. A. Kandiel, L. Robben, A. Alkaim, and D. Bahnemann. Brookite versus anatase  $\text{TiO}_2$  photocatalysts: phase transformations and photocatalytic activities. *Photochem. Photobiol. Sci.*, 12, 2013.
- [29] A. Vittadini, A. Selloni, F. P. Rotzinger, and M. Grätzel. Structure and energetics of water adsorbed at  $\text{TiO}_2$  anatase 101 and 001 surfaces. *Phys. Rev. Lett.*, 81:2954–2957, 1998.
- [30] G. Martra. Lewis acid and base sites at the surface of microcrystalline  $\text{TiO}_2$  anatase: relationships between surface morphology and chemical behaviour. *Applied Catalysis A: General*, 200(1-2):275–285, 2000.
- [31] A. Vittadini, A. Selloni, F. P. Rotzinger, and M. Grätzel. Structure and energetics of water adsorbed at  $\text{TiO}_2$  anatase (101) and (001) surfaces. *Phys. Rev. Lett.*, 81:2954–2957, 1998.
- [32] S. Yang, N. Huang, Y. M. Jin, H. Q. Zhang, Y. H. Su, and H. G. Yang. Crystal shape engineering of anatase  $\text{TiO}_2$  and its biomedical applications. *CrystEngComm*, 17:6617–6631, 2015.
- [33] C. D. Valentin, E. Finazzi, G. Pacchioni, A. Selloni, S. Livraghi, M. C. Paganini, and E. Giamello. N-doped  $\text{TiO}_2$ : Theory and experiment. *Chemical Physics*, 339(1-3):44–56, 2007.
- [34] R. Janisch, P. Gopal, and N. A. Spaldin. Transition metal-doped  $\text{TiO}_2$  and  $\text{ZnO}$ —present status of the field. *Journal of Physics: Condensed Matter*, 17(27):R657, 2005.
- [35] J. Zhu, Z. Deng, F. Chen, J. Zhang, H. Chen, M. Anpo, J. Huang, and L. Zhang. Hydrothermal doping method for preparation of  $\text{Cr}^{+3}$ - $\text{TiO}_2$  photocatalysts with concentration gradient distribution of  $\text{Cr}^{+3}$ .
- [36] C.-H. Li, Y.-H. Hsieh, W.-T. Chiu, C.-C. Liu, and C.-L. Kao. Study on preparation and photocatalytic performance of  $\text{Ag}/\text{TiO}_2$  and  $\text{Pt}/\text{TiO}_2$  photocatalysts. *Separation and Purification Technology*, 58(1):148–151, 2007.

- [37] J. Yu, J. Xiong, B. Cheng, and S. Liu. Fabrication and characterization of Ag–TiO<sub>2</sub> multiphase nanocomposite thin films with enhanced photocatalytic activity. *Applied Catalysis B: Environmental*, 60(3–4):211–221, 2005.
- [38] Y. Han and a. Q. G. Chang-jun Liu. Interaction of Pt clusters with the anatase TiO<sub>2</sub> surface: A first principles study. *The Journal of Physical Chemistry B*, 110(14):7463–7472, 2006.
- [39] S. Gupta and M. Tripathi. A review of TiO<sub>2</sub> nanoparticles. *Chinese Science Bulletin*, 56(16):1639–1657, 2011.
- [40] Z. Zhang and J. John T. Yates. Band bending in semiconductors: Chemical and physical consequences at surfaces and interfaces. *Chemical Reviews*, 112(10):5520–5551, 2012.
- [41] C. T. Campbell and J. Sauer. Introduction: Surface chemistry of oxides. *Chemical Reviews*, 113(6):3859–3862, 2013.
- [42] S. Bingham and W. A. Daoud. Recent advances in making nano-sized TiO<sub>2</sub> visible-light active through rare-earth metal doping. *J. Mater. Chem.*, 21.
- [43] C. Li, M. Liu, N. G. Pschirer, M. Baumgarten, and K. Müllen. Polyphenylene-based materials for organic photovoltaics. *Chemical Reviews*, 110(11):6817–6855, 2010.
- [44] A. W. Hains, Z. Liang, M. A. Woodhouse, and B. A. Gregg. Molecular semiconductors in organic photovoltaic cells. *Chemical Reviews*, 110(11):6689–6735, 2010.
- [45] X. Huang, S. Han, W. Huang, and X. Liu. Enhancing solar cell efficiency: the search for luminescent materials as spectral converters. *Chem. Soc. Rev.*, 42:173–201, 2013.
- [46] J. Choi, P. Sudhagar, P. Lakshmiathiraj, J. W. Lee, A. Devadoss, S. Lee, T. Song, S. Hong, S. Eito, C. Terashima, T. H. Han, J. K. Kang, A. Fujishima, Y. S. Kang, and U. Paik. Three-dimensional gd-doped TiO<sub>2</sub> fibrous photoelectrodes for efficient visible light-driven photocatalytic performance. *RSC Adv.*, 4:11750–11757, 2014.
- [47] J. Lin and J. C. Yu. An investigation on photocatalytic activities of mixed TiO<sub>2</sub>-rare earth oxides for the oxidation of acetone in air. *Journal of Photochemistry and Photobiology A: Chemistry*, 116(1):63–67, 1998.
- [48] K. Parida and N. Sahu. Visible light induced photocatalytic activity of rare earth titania nanocomposites. *Journal of Molecular Catalysis A: Chemical*, 287(1–2):151–158, 2008.

- [49] H. Shi, T. Zhang, and H. Wang. Preparation and photocatalytic activity of  $\text{La}^{+3}$  and  $\text{Eu}^{+3}$  co-doped  $\text{TiO}_2$  nanoparticles: photo-assisted degradation of methylene blue. *Journal of Rare Earths*, 29:746–752, 2011.
- [50] C. Liang, C. Liu, F. Li, and F. Wu. The effect of praseodymium on the adsorption and photocatalytic degradation of azo dye in aqueous  $\text{Pr}^{+3}$ - $\text{TiO}_2$  suspension. *Chemical Engineering Journal*, 147(2–3):219–225, 2009.
- [51] Y. Bai, I. Mora-Seró, F. D. Angelis, J. Bisquert, and P. Wang. Titanium dioxide nanomaterials for photovoltaic applications. *Chemical Reviews*, 114(19):10095–10130, 2014.
- [52] A. Hagfeldt, G. Boschloo, L. Sun, L. Kloo, and H. Pettersson. Dye-sensitized solar cells. *Chemical Reviews*, 110(11):6595–6663, 2010.
- [53] M. Urbani, M. Grätzel, M. K. Nazeeruddin, and T. Torres. Meso-substituted porphyrins for dye-sensitized solar cells. *Chemical Reviews*, 114(24):12330–12396, 2014.
- [54] N. Martsinovich, D. R. Jones, and A. Troisi. Electronic structure of  $\text{TiO}_2$  surfaces and effect of molecular adsorbates using different DFT implementations. *The Journal of Physical Chemistry C*, 114(51):22659–22670, 2010.
- [55] A. Vittadini, A. Selloni, F. P. Rotzinger, and M. Grätzel. Formic acid adsorption on dry and hydrated  $\text{TiO}_2$  anatase (101) surfaces by DFT calculations. *The Journal of Physical Chemistry B*, 104(6):1300–1306, 2000.
- [56] P. Persson, R. Bergström, , and S. Lunell. Quantum chemical study of photoinjection processes in dye-sensitized  $\text{TiO}_2$  nanoparticles. *The Journal of Physical Chemistry B*, 104(44):10348–10351, 2000.
- [57] Q. Guo, I. Cocks, and E. Williams. The adsorption of benzoic acid on a  $\text{TiO}_2(110)$  surface studied using STM, ESDIAD and LEED. *Surface Science*, 393(1–3):1–11, 1997.
- [58] K. Liu, Y. Zheng, G. Jia, M. Yang, Y. Huang, and H. You. Facile synthesis of hierarchically superstructured praseodymium benzenetricarboxylate with controllable morphologies. *CrystEngComm*, 13:452–458, 2011.
- [59] H.-M. Wang, H.-X. Li, X.-Y. Yu, Z.-G. Ren, and J.-P. Lang. Cyclodimerization and cyclotrimerization of isocyanates promoted by one praseodymium benzenethiolate complex  $[\text{Pr}(\text{SPh})_3(\text{THF})_3]$ . *Tetrahedron*, 67(8):1530–1535, 2011.
- [60] W. Peng, Z. S. M., M. J. E., N. M. K., S. Takashi, and G. Michael. A stable quasi-solid-state dye-sensitized solar cell with an amphiphilic ruthenium sensitizer and polymer gel electrolyte. *Nat Mater*, 2(6):402–407, 2003.

- [61] D. Kuang, J. Brillet, P. Chen, M. Takata, S. Uchida, H. Miura, K. Sumioka, S. M. Zakeeruddin, and M. Grätzel. Application of highly ordered  $\text{TiO}_2$  nanotube arrays in flexible dye-sensitized solar cells. *ACS Nano*, 2(6):1113–1116, 2008.
- [62] W. Peng, Z. S. M., M. J. E., N. M. K., S. Takashi, and G. Michael. A stable quasi-solid-state dye-sensitized solar cell with an amphiphilic ruthenium sensitizer and polymer gel electrolyte. *Nat Mater*, 2(6):402–407, 2003.
- [63] Y. Chen, Z. Zeng, C. Li, W. Wang, X. Wang, and B. Zhang. Highly efficient co-sensitization of nanocrystalline  $\text{TiO}_2$  electrodes with plural organic dyes. *New J. Chem.*, 29:773–776, 2005.
- [64] M. Velusamy, K. R. J. Thomas, J. T. Lin, Y.-C. Hsu, and K.-C. Ho. Organic dyes incorporating low-band-gap chromophores for dye-sensitized solar cells. *Organic Letters*, 7(10):1899–1902, 2005.
- [65] J. M. Rehm, G. L. McLendon, Y. Nagasawa, K. Yoshihara, J. Moser, and M. Grätzel. Femtosecond electron-transfer dynamics at a sensitizing dye–semiconductor  $\text{TiO}_2$  interface. *The Journal of Physical Chemistry*, 100(23):9577–9578, 1996.
- [66] O. Enea, J. Moser, and M. Grätzel. Achievement of incident photon to electric current conversion yields exceeding 80 *Journal of Electroanalytical Chemistry and Interfacial Electrochemistry*, 59(1):59–65, 1989.
- [67] P. Ricci, a. Da Pozzo, S. Palmas, F. Muscas, and C. Carbonaro. Efficient charge transfer process in Coumarin 153–nanotubular  $\text{TiO}_2$  hybrid system. *Chemical Physics Letters*, 531:160–163, 2012.
- [68] J. Kohanoff. Electronic structure calculations for solids and molecules: theory and computational methods. pages 3–120, 2006.
- [69] R. M. Martin. Electronic structure basic theory and practical methods. 2008.
- [70] D. R. Hartree. The wave mechanics of an atom with a non-coulomb central field. part i. theory and methods. *Mathematical Proceedings of the Cambridge Philosophical Society*, 24:89–110, 1 1928.
- [71] J. C. Slater. Note on hartree’s method. *Phys. Rev.*, 35:210–211, 1930.
- [72] L. H. Thomas. The calculation of atomic fields. *Mathematical Proceedings of the Cambridge Philosophical Society*, 23:542–548, 1927.
- [73] P. Hohenberg and W. Kohn. Inhomogeneous electron gas. *Phys. Rev.*, 136:B864–B871, 1964.



- [74] D. M. Ceperley and B. J. Alder. Ground state of the electron gas by a stochastic method. *Phys. Rev. Lett.*, 45:566–569, 1980.
- [75] J. P. Perdew, K. Burke, and M. Ernzerhof. Generalized gradient approximation made simple. *Phys. Rev. Lett.*, 77:3865–3868, 1996.
- [76] D. Vanderbilt. Soft self-consistent pseudopotentials in a generalized eigenvalue formalism. *Phys. Rev. B*, 41:7892–7895, 1990.
- [77] P. E. Blöchl. Projector augmented-wave method. *Phys. Rev. B*, 50:17953–17979, 1994.
- [78] D. C. Langreth and M. J. Mehl. Beyond the local-density approximation in calculations of ground-state electronic properties. *Phys. Rev. B*, 28:1809–1834, 1983.
- [79] S. L. Dudarev, G. A. Botton, S. Y. Savrasov, C. J. Humphreys, and A. P. Sutton. Electron-energy-loss spectra and the structural stability of nickel oxide: An LSDA+U study. *Phys. Rev. B*, 57:1505–1509, 1998.
- [80] E. Sanville, S. D. Kenny, R. Smith, and G. Henkelman. Improved grid-based algorithm for bader charge allocation. *Journal of Computational Chemistry*, 28(5):899–908, 2007.
- [81] G. Henkelman, A. Arnaldsson, and H. Jónsson. A fast and robust algorithm for bader decomposition of charge density. *Computational Materials Science*, 36(3):354 – 360, 2006.
- [82] E. Finazzi, C. Di Valentin, G. Pacchioni, and A. Selloni. Excess electron states in reduced bulk anatase TiO<sub>2</sub>: Comparison of standard GGA, GGA+U, and hybrid DFT calculations. *The Journal of Chemical Physics*, 129(15):154113–9, 2008.
- [83] M. M. Islam, M. Calatayud, and G. Pacchioni. Hydrogen adsorption and diffusion on the anatase TiO<sub>2</sub>(101) surface: A first-principles investigation. *The Journal of Physical Chemistry C*, 115(14):6809–6814, 2011.
- [84] M. E. Arroyo-de Dompablo, A. Morales-García, and M. Taravillo. DFT+U calculations of crystal lattice, electronic structure, and phase stability under pressure of TiO<sub>2</sub> polymorphs. *The Journal of Chemical Physics*, 135(5):054503–9, 2011.
- [85] A. E. Bocquet, T. Mizokawa, K. Morikawa, A. Fujimori, S. R. Barman, K. Maiti, D. D. Sarma, Y. Tokura, and M. Onoda. Electronic structure of early 3d -transition-metal oxides by analysis of the 2p core-level photoemission spectra. *Phys. Rev. B*, 53:1161–1170, 1996.
- [86] F. Tran, J. Schweifer, P. Blaha, K. Schwarz, and P. Novák. PBE+U calculations of the jahn-teller effect in Pro<sub>2</sub>. *Phys. Rev. B*, 77:085123, 2008.

- [87] L. Kavan, M. Grätzel, S. E. Gilbert, C. Klemenz, and H. J. Scheel. Electrochemical and photoelectrochemical investigation of single-crystal anatase. *Journal of the American Chemical Society*, 118(28):6716–6723, 1996.
- [88] M. B. Kanoun, A. H. Reshak, N. Kanoun-Bouayed, and S. Goumri-Said. Evidence of coulomb correction and spin-orbit coupling in rare-earth dioxides CeO<sub>2</sub>, PrO<sub>2</sub> and TbO<sub>2</sub>: An Ab initio study. *Journal of Magnetism and Magnetic Materials*, 324(7):1397–1405, 2012.
- [89] A. Sayede, R. Khenata, A. Chahed, and O. Benhelal. Electronic and optical properties of layered RE<sub>2</sub>Ti<sub>2</sub>O<sub>7</sub> from first principles. *Journal of Applied Physics*, 113(17):173501–5, 2013.
- [90] W. Chen, P. Yuan, S. Zhang, Q. Sun, E. Liang, and Y. Jia. Electronic properties of anatase TiO<sub>2</sub> doped by lanthanides: A DFT+U study. *Physica B: Condensed Matter*, 407(6):1038–1043, 2012.
- [91] B. Bouadjemi, S. Bentata, A. Abbad, W. Benstaali, and B. Bouhafs. Half-metallic ferromagnetism in PrMnO<sub>3</sub> perovskite from first principles calculations. *Solid State Communications*, 168:6–10, 2013.
- [92] F. Spadavecchia, G. Cappelletti, S. Ardizzone, M. Ceotto, M. S. Azzola, L. L. Presti, G. Cerrato, and L. Falciola. Role of pr on the semiconductor properties of nanotitania. an experimental and first-principles investigation. *The Journal of Physical Chemistry C*, 116(43):23083–23093, 2012.
- [93] A. Prokofiev, A. Shelykh, and B. Melekh. Periodicity in the band gap variation of Ln<sub>2</sub>X<sub>3</sub> (x = o, s, se) in the lanthanide series. *Journal of Alloys and Compounds*, 242(1–2):41–44, 1996.
- [94] H. Lal and K. Gaur. Electrical conduction in non-metallic rare-earth solids. *Journal of Materials Science*, 23(3):919–923, 1988.
- [95] N. Hirosaki, S. Ogata, and C. Kocer. Ab initio calculation of the crystal structure of the lanthanide Ln<sub>2</sub>O<sub>3</sub> sesquioxides. *Journal of Alloys and Compounds*, 351(1–2):31–34, 2003.
- [96] O. Greis, R. Ziel, B. Breidenstein, A. Haase, and T. Petzel. The crystal structure of the low-temperature a-type modification of pr<sub>2</sub>O<sub>3</sub> from x-ray powder and electron single crystal diffraction. *Journal of Alloys and Compounds*, 216(2):255–258, 1995.
- [97] H. Jiang, P. Rinke, and M. Scheffler. Electronic properties of lanthanide oxides from the *gw* perspective. *Phys. Rev. B*, 86:125115, 2012.
- [98] F. Labat, P. Baranek, , and C. Adamo. Structural and electronic properties of selected rutile and anatase TiO<sub>2</sub> surfaces. *Journal of Chemical Theory and Computation*, 4(2):341–352, 2008.

- [99] X.-Q. Gong, A. Selloni, M. Batzill, and U. Diebold. Steps on anatase  $\text{TiO}_2(101)$ . *Nat Mater*, 5(8):665–670.
- [100] E. Mete, D. Uner, O. Gülseren, and i. m. c. Ellialtıođlu. Pt-incorporated anatase  $\text{TiO}_2(001)$  surface for solar cell applications: First-principles density functional theory calculations. *Phys. Rev. B*, 79:125418, 2009.
- [101] Y. Lin, Z. Jiang, C. Zhu, X. Hu, X. Zhang, H. Zhu, J. Fan, and S. H. Lin. C/B codoping effect on band gap narrowing and optical performance of  $\text{TiO}_2$  photocatalyst: a spin-polarized DFT study.
- [102] J. Wu, Q. Liu, P. Gao, and Z. Zhu. Influence of praseodymium and nitrogen co-doping on the photocatalytic activity of  $\text{TiO}_2$ . *Materials Research Bulletin*, 46(11):1997–2003, 2011.
- [103] G. A. Sim, J. M. Robertson, and T. H. Goodwin. The crystal and molecular structure of benzoic acid. *Acta Crystallographica*, 8(3):157–164, 1955.
- [104] M. Samsonowicz. Molecular structure of phenyl- and phenoxyacetic acids – spectroscopic and theoretical study. *Spectrochimica Acta Part A: Molecular and Biomolecular Spectroscopy*, 118:1086–1097, 2014.
- [105] M. Samsonowicz. Molecular structure of phenyl- and phenoxyacetic acids – spectroscopic and theoretical study. *Spectrochimica Acta Part A: Molecular and Biomolecular Spectroscopy*, 118:1086–1097, 2014.
- [106] G. Pan, W. Jing, L. Qing-Ju, and Z. Wen-Fang. First-principles study on anatase  $\text{TiO}_2$  codoped with nitrogen and praseodymium. *Chinese Physics B*, 19(8):087103, 2010.
- [107] J. Wu, Q. Liu, P. Gao, and Z. Zhu. Influence of praseodymium and nitrogen co-doping on the photocatalytic activity of  $\text{TiO}_2$ . *Materials Research Bulletin*, 46(11):1997–2003, 2011.
- [108] G. J. II, W. R. Jackson, C. Y. Choi, and W. R. Bergmark. Solvent effects on emission yield and lifetime for coumarin laser dyes. requirements for a rotatory decay mechanism. *The Journal of Physical Chemistry*, 89(2):294–300, 1985.
- [109] D. Wang, C. Hao, S. Wang, H. Dong, and J. Qiu. Time-dependent density functional theory study on the electronic excited-state hydrogen bonding of the chromophore coumarin 153 in a room-temperature ionic liquid. *Journal of Molecular Modeling*, 18(3):937–945, 2012.
- [110] Y. He, O. Dulub, H. Cheng, A. Selloni, and U. Diebold. Evidence for the predominance of subsurface defects on reduced anatase  $\text{TiO}_2$ . *Phys. Rev. Lett.*, 102:106105, 2009.

- [111] P. Scheiber, M. Fidler, O. Dulub, M. Schmid, U. Diebold, W. Hou, U. Aschauer, and A. Selloni. (sub)surface mobility of oxygen vacancies at the TiO<sub>2</sub> anatase (101) surface. *Phys. Rev. Lett.*, 109:136103, 2012.
- [112] H. Cheng and A. Selloni. Surface and subsurface oxygen vacancies in anatase TiO<sub>2</sub> and differences with rutile. *Physical Review B*, 79(9):2–5, 2009.
- [113] A. S. Weber, A. M. Grady, and R. T. Koodali. Lanthanide modified semiconductor photocatalysts. *Catal. Sci. Technol.*, 2:683–693, 2012.
- [114] W. Setyawan, R. M. Gaume, S. Lam, R. S. Feigelson, and S. Curtarolo. High-throughput combinatorial database of electronic band structures for inorganic scintillator materials. *ACS Combinatorial Science*, 13(4):382–390, 2011.
- [115] Z. Huang, L. Ye, Z. Q. Yang, and X. Xie. Interaction between er atoms and the carbon cage c<sub>82</sub>. *Phys. Rev. B*, 61:12786–12791, 2000.

# CURRICULUM VITAE

## PERSONAL INFORMATION

**Surname, Name:** Vural, Kivılcım Bařak

**Nationality:** Turkish (TC)

**Date and Place of Birth:** 28.07.1981

**Marital Status:** Single

**Phone:** 05326255622

## EDUCATION

<b>Degree</b>	<b>Institution</b>	<b>Year of Graduation</b>
M.S.	METU in Physics	2006
B.S.	AİBU in Physics	1999
High School	Bahçelievler Deneme High School, Ankara	1999